Modeling and control of new generation of tethered energy drone

Audrey Schanen

THÈSE

Pour obtenir le grade de

DOCTEUR DE L'UNIVERSITÉ GRENOBLE ALPES

Spécialité : AUTOMATIQUE - PRODUCTIQUE

Arrêté ministériel : 25 mai 2016

Présentée par

Audrey SCHANEN

Thèse dirigée par **Ahmad HABLY**, Université Grenoble Alpes
et codirigée par **Nacim MESLEM**, Université Grenoble Alpes
et **Jonathan DUMON**,IE,CNRS

préparée au sein du **Laboratoire Grenoble Images Parole Signal Automatique**
dans **l'École Doctorale Electronique, Electrotechnique, Automatique, Traitement du Signal (EEATS)**

Modélisation et commande d'un drone captif

Modeling and control of new generation of tethered energy drone

Thèse soutenue publiquement le **10 décembre 2021**,
devant le jury composé de :

Monsieur Ahmad HABLY
PROFESSEUR ASSOCIE, Université Grenoble Alpes, Directeur de thèse
Monsieur Nicolas Marchand
DIRECTEUR DE RECHERCHE, Grenoble INP - Gipsa-lab, Examinateur
Madame Delphine Riu
PROFESSEUR, Grenoble INP, Présidente du jury
Monsieur Pedro Castillo
DIRECTEUR DE RECHERCHE, UTC, Rapporteur
Monsieur Edouard Laroche
PROFESSEUR DES UNIVERSITES, ICUBE, Rapporteur
Monsieur José Fermi Guerrero-Castellanos
MAITRE DE CONFERENCE, Benemérita Universidad Autónoma de Puebla, Examinateur

ACKNOWLEDGMENT

These three years of work were such an experience that could not have taken place without my supervisors Ahmad, Nacim and Jonathan who offer me the possibility of working on this very interesting and innovative subject.

I would like to thank in particular Jonathan, Alexandre, Amaury and the mechatronic prototyping centre for the support on the development of the prototype which allowed me to perform experimentation. It was a very interesting part of my work and I am very happy to have been able to take part to this development. It was the outcome of my work and I am glad to have succeed.

For the support during this years, I would like to thank the members of Gipsa-lab, who most of the time were my former teachers, for always have a smile or a nice word to me.

The last thank is for my Ph.D colleagues who I did not see a lot but were always taking news on my work and it was always nice to talk with them.

MODELING AND CONTROL OF NEW GENERATION OF TETHERED ENERGY DRONE

Abstract

by Audrey Schanen, Ph.D.
Université Grenoble Alpes
October 2021

The French energy transition law imposes a reduction of the fossil energies down to 50% within 10 years. Transition scenarios foresees renewable part of energy production to reach between 40% and 70%, with an increasing portion of wind energy. By 2027, the IEA predicts that wind will be the number-one source of the EU's energy, but even that will not be enough to meet stringent emissions targets. Considering for example the floating offshore wind turbines, the material amount per unit of power involved in the construction of wind turbines and floating devices may render this concept unsustainable if it is scaled with current fossils energy production levels. The emerging airborne wind energy (AWE) sector offers breakthrough concepts that will allow diversifying the wind energy production offer.

Recent research results are gradually assessing and eliminating feasibility risks and improving the understanding of AWE systems. A key premise for airborne wind is that it should be able to significantly reduce costs by cutting the amount of materials required for each generation unit, compared to traditional turbines. On the other hand, and unlike turbines, AWE systems have to cope with partially unpredictable wind to remain airborne and need to land when wind conditions are poor. Landings and launches are hard to automate, and each one raises the risk of catastrophic failure. Indeed, the presence of atmospheric turbulence in the lower layers of the atmospheric boundary layer as well as possibly the movement of the

landing platform make the wind conditions very delicate (high turbulence and significant speed gradients). For example, in 2019, Makani's offshore 600kW energy kite prototype was lost during landing.

In order to safely perform the take-off and landing phases of a drone-based AWE system, the objective is to steer it to a desired location (or position) in the air while maintaining the tether to a defined range of tension. To achieve that, a nonlinear multi-objectives controller is proposed to control simultaneously the drone and the on-ground winch. Since the main goal is to reach a target position and not to follow up closely a user-defined trajectory, a margin on the tracking error is tolerated while the system stays in a safety zone to avoid crashes. This controller is then tested and validated in simulation and experimentally on a developed prototype. Wind disturbances are also added to test the robustness of the controller. It appears that for high wind speed the aerodynamic forces have to be taken into account in the controller design. That is why an Extended Kalman Filter (EKF) has been developed to estimate these forces and include them to the controller.

Résumé Les systèmes éoliens aéroportés ont attiré beaucoup d'attention ces dernières années. Le but de ce système est de proposer un design alternatif aux éoliennes conventionnelles, grâce à un profil aérodynamique attaché au sol par un câble. L'idée est d'utiliser moins de structures et de fondations que pour les éoliennes conventionnelles et d'ainsi atteindre des vents de hautes altitudes qui sont plus stables et plus forts. Plus facile à transporter et à installer, ces systèmes peuvent permettre d'exploiter des gisements éoliens inaccessibles par les technologies actuelles, et sont bien mieux adaptés pour une installation sur des plateformes flottantes. Enfin, ces systèmes peuvent également être installés sur des bateaux comme complément de propulsion éolien, ce qui peut permettre de réduire significativement le recours aux combustibles fossiles dans ce domaine.

Il existe deux catégories de système éolien aéroporté : les systèmes avec production au sol et ceux avec production embarquée. Pour la production au sol,l'élément volant est relié à une génératrice au sol grâce à un câble. Pour la production embarquée, la production d'énergie se fait en vol et est récupérée au sol à l'aide d'un câble conducteur.

Dans la littérature, la modélisation, le contrôle et l'optimisation de ces systèmes sont des sujets largements traités que ce soit théoriquement, en simulation ou expérimentalement. Cependant, un point important qui a été peu étudié est son décollage et son aterrissage, notamment pour la commercialisation de tels systèmes.

L'objectif de la thèse est de proposer une solution de décollage et d'aterrissage pour système éolien aéroporté. Pour cela, la solution envisagée utilise un drone sur lequel seront fixés d'une part le profil aérodynamique et d'autre part le câble. Après avoir modéliser le système, un contrôleur a été développer pour permettre de faire décoller et atterir le système en sécurité, tout en gardant le câble tendu. L'objectif étant d'atteindre une position souhaité et non de suivre parfaitement une trajectoire, une certaine erreur est tolérée tant que le système reste dans une zone de sécurité, pour ainsi éviter les crashs. Ce contrôleur a ensuite été testé et valié en simulation puis sur un protoype expérimental développé pour cette thèse. Les tests ont aussi été réalisés en présence de vent pour tester la robustesse du contrôleur. Pour des faibles vitesses de vent, le contrôleur arrive à rejeter cette perturbation, mais quand celui ci augmente, ild evient nécessaire d'intégrer les forces aérodynamiques au contrôleur. C'est pour ça qu'un filtre de Kalman fut ajouter pour estimer les forces aérodynamiques et ainsi pouvoir les prendre en compte dans le contrôleur.

Contents

List of Tables

List of Figures

Dedication

This thesis is dedicated to my mother and father.

Publication list

1. Schanen, Audrey; Dumon, Jonathan; Meslem, Nacim; Hably, Ahmad; Nègre, Amaury; Sarazin, Alexandre , "***Tethered drone-based Airborne wind energy system launching and retrieving***", *Journal of Guidance, Control, and Dynamics*, p. 1-10.

2. Schanen, Audrey; Dumon, Jonathan; Meslem, Nacim; Hably, Ahmad, "***Take-off and landing of an AWE system using a multicopter***", ACC 2020, USA.

3. Schanen, Audrey; Dumon, Jonathan; Meslem, Nacim; Hably, Ahmad, "***On Using Drones for the Take-off and Landing Phases of an AWE System***", AWEC 2019, Scotland.

4. Schanen, Audrey; Dumon, Jonathan; Meslem, Nacim; Hably, Ahmad, " ***Experimental Results on drone-based Take-Off and Landing of an AWE System*** ", WESC 2021, Germany.

Chapter One

Introduction

1.1 Motivation

The French energy transition law imposes a reduction of the fossil energies down to 50% within 10 years. Transition scenarios foresees renewable part of energy production to reach between 40% and 70%, with an increasing portion of wind energy. By 2027, the IEA [1] predicts that wind will be the number-one source of the EU's energy, but even that will not be enough to meet stringent emissions targets. Considering for example the floating offshore wind turbines, the material amount per unit of power involved in the construction of wind turbines and floating devices may render this concept unsustainable if it is scaled with current fossils energy production levels.

The emerging airborne wind energy (AWE) sector offers breakthrough concepts that will allow diversifying the wind energy production offer. The first research on this kind of system dates back to the 1930s with the work of Aloys van Gries [2], a German engineer. In the end of the 20th century, Miles L. Loyd [3] compares the power produced by a conventional wind turbines to the power generated by an AWE system. It appears that the AWE system could theoretically generate much more energy than the conventional system. From this point, the sector of airborne wind energy started to grow up. The first companies are born in the beginning of the 21th century with for example Ampyx Power [4] (2008) and Kitemill

[5] (2008). On the other side of the Atlantic, the Makani company [6] in 2006 started the development and building of a first real scale working prototype. This prototype (Fig.1.1) was able to generate up to 600 kW. The company closed in September 2020, leaving 13 years of research in open access.

Figure 1.1 Makani's M600 AWE system. Source: Alphabet Inc [6].

Different design of airborne wind energy systems exist. It is composed of a flying device linked to the ground through a tether. There are two main ways to categorize most airborne wind energy designs: soft-wing versus rigid-wing. In addition to this first classification, those that generate energy in the air (on-board) versus those that use a pumping motion to power an on-ground generator, as shown in Fig.1.2. The system can be installed on the land but there are also offshore system, as the one from Makani.

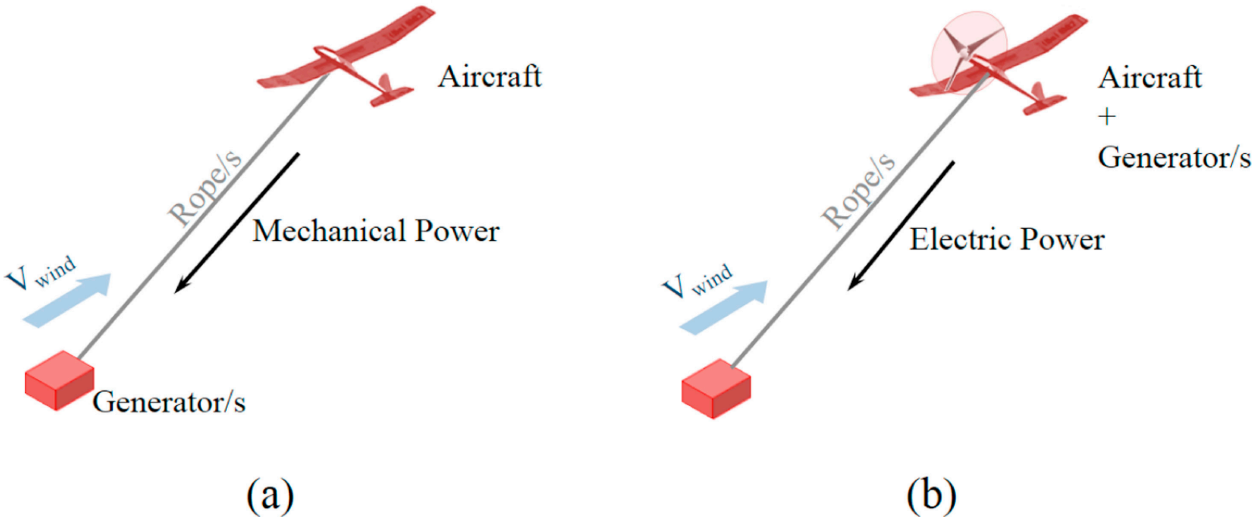

Figure 1.2 AWE system with on-ground generator (a) and on-board (b). Source: [7]

The physics behind airborne wind energy includes diverse range of concepts involving aerodynamic tethered structures that capture high-altitude wind energy, of different power range (from KW to MW), and deliver it to the ground. As an example, Kitepower [8] can produce 100kW for a wing area of $47m^2$, with the system presented on Fig.1.3. Enerkite [9] (Fig.1.4) announces a system rated power of 500 kW for a wing area of $125m^2$.

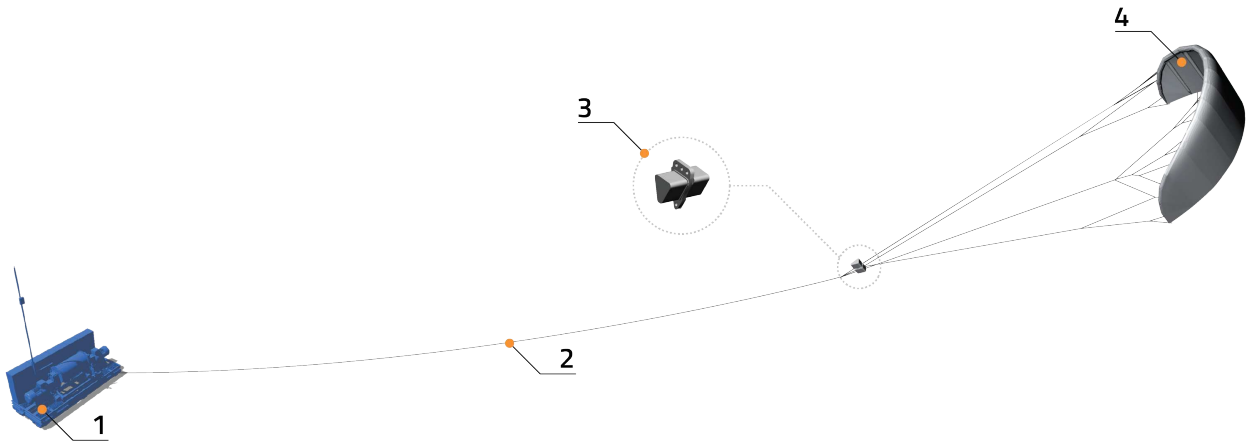

Figure 1.3 Kitepower system with (1) the ground-station, (2) the tether, (3) the kite control unit and (4) the kite. Source: Kitepower website [8].

Figure 1.4 Enerkite system. Source: Enerkite website [9].

Recent research results are gradually assessing and eliminating feasibility risks and improving the understanding of AWE systems. A key premise for airborne wind is that it should be able to significantly reduce costs by cutting the amount of materials required for each generation unit, compared to traditional turbines. On the other hand, and unlike turbines, AWE systems have to cope with partially unpredictable wind to remain airborne and need to land when wind conditions are poor. Landings and launches are hard to automate, and each one raises the risk of catastrophic failure. Indeed, the presence of atmospheric turbulence in the lower layers of the atmospheric boundary layer as well as possibly the movement of the landing platform make the wind conditions very delicate (high turbulence and significant speed gradients). For example, in 2019, Makani's offshore 600kW energy kite prototype was lost during landing.

1.2 Background

In the field of AWE system, some studies have been done on the take-off and landing of such systems.

In [10], three take-off approaches of a rigid wing are presented: a vertical take-off with on-board propellers, a rotational take-off and a linear take-off with on-board propellers. Each approach is discussed according to chosen criteria. Vertical take-off requires a small ground area and allows to take-off in a large range of wind conditions. However, it induces additional on-board power and mass. To deal with this issue, the design of the wing has to be rethink. The rotational take-off is done using a rotating arm which will take a large ground area. It has the advantages to require a low on-board power and additional mass. However, this solution involve high manufacturing and installation costs. The last approach, the linear take-off (Fig.1.5) requires a small ground area, on-board power and additional mass. The chosen approach is the last one, since it is the approach with the less impact on the system design. Then the author studies this approach in simulation, with an interest on the power used.

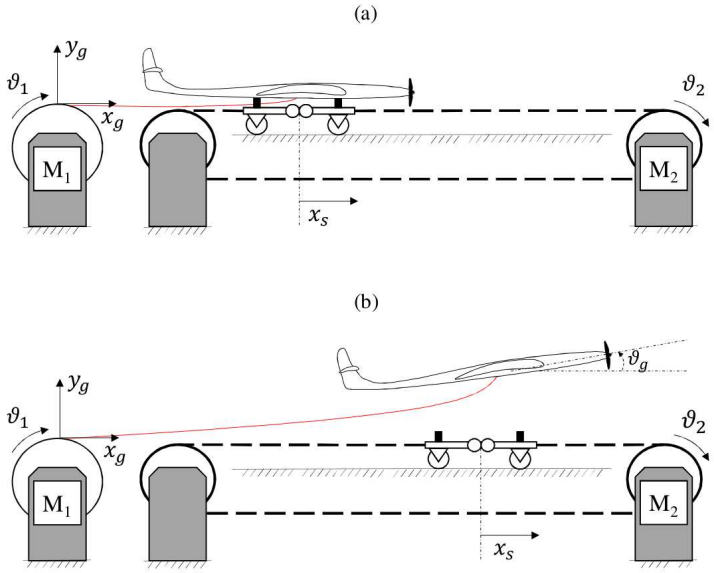

Figure 1.5 Linear take-off procedure. Source: [10]

In [11] a take-off and landing solution using a multicopter is presented (Fig1.6). The analysis of this approach is done for a flexible wing. The approach consists in using a multicopter to take the wing at a parking position from where it could start the production phase. Then the multicopter leaves the wing in the air and lands. For the landing of the kite, the on-ground winch is used. The controller presented for the multicopter allows the system to follow a trajectory for the take-off. This solution is valid under certain hypothesis. The knowledge of the aerodynamic model of the kite, and information on the wind speed and direction are also required. This approach is then tested in simulation. An equilibrium analysis is also done to calculate the boundary conditions.

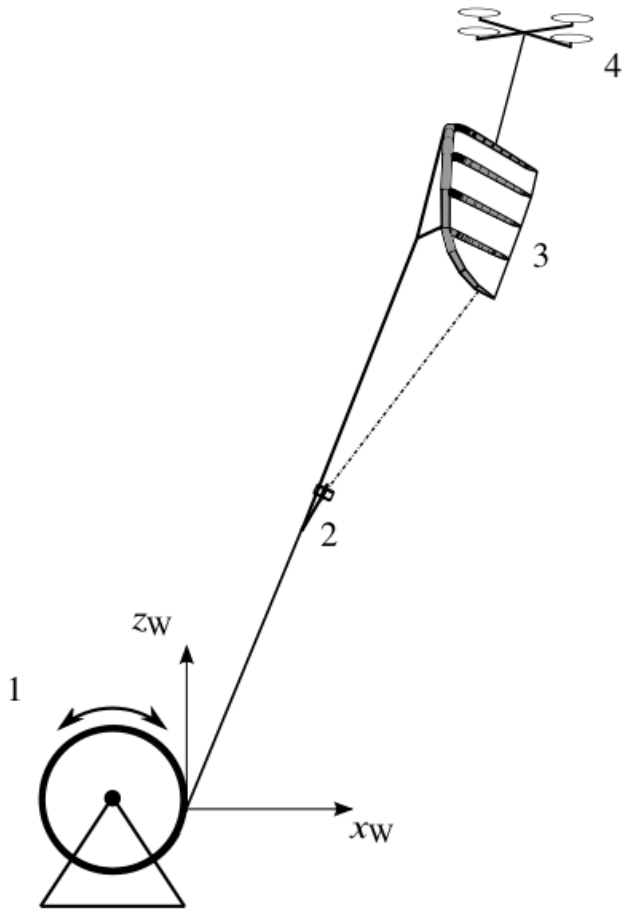

Figure 1.6 Vertical take-off procedure with ground station 1, kite steering unit 2, kite 3 and multicopter 4. Source: [11]

In [12] different methods for take-off and landing are presented. The solution using a multicopter (Fig.1.7) is then studied through static and dynamic analyses. According to the authors the advantages of this approach are the simplicity of the on-ground winch (compared to rotational take-off for example) and the possibility to launch and land even in absence of wind. However, the multicopter and its energy storage involve a high airborn-mass and a higher drag. A solution of electric tether moved by a carriage along the tether to supply the multicopter is proposed and will be developed in a future work. It concludes about a disadvantage of soft kite which generates a lift force opposite to the propeller thrust during the take-off.

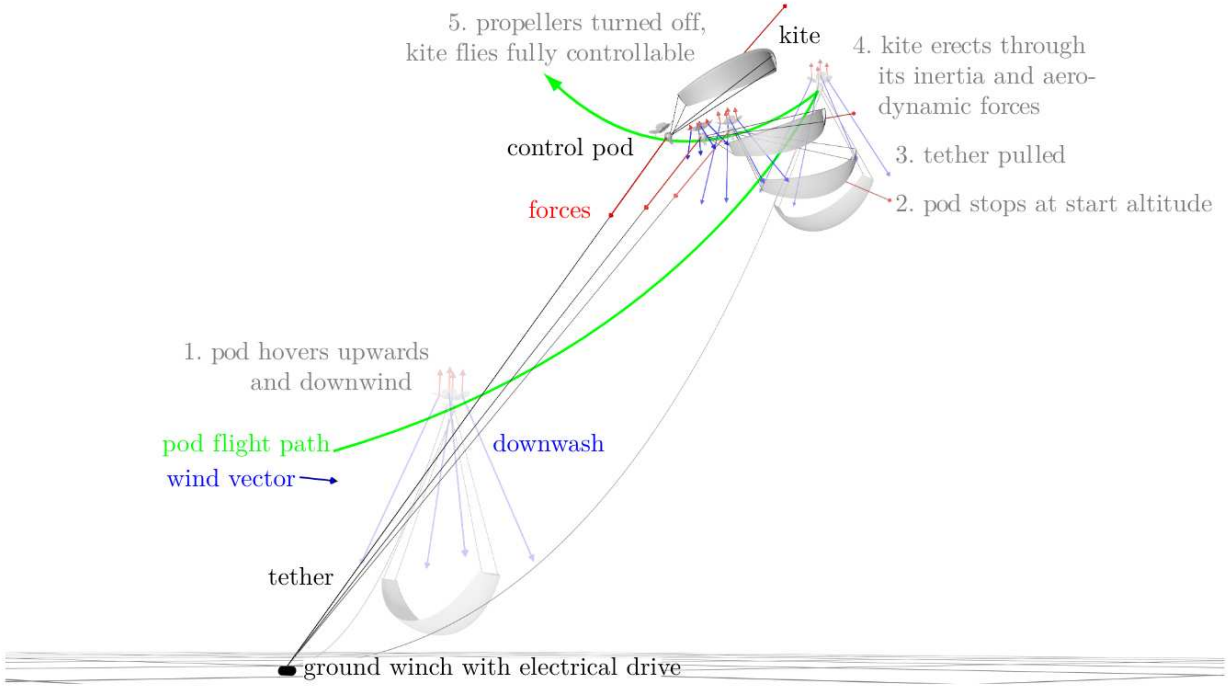

Figure 1.7 Take-off with a multicopter Source: [12]

The proposed solutions allow to perform a take-off and/or a landing under different wind conditions. However, none of these solutions have been tested experimentally. Note that, in the literature, the work on tethered drone can also be studied since the systems are quite similar.

In [13], a marine locomotive quadrotor UAV is presented (Fig.1.8). The system is com-

posed of a UAV linked to a buoy through a tether. The tether is an umbilical power tether to deal with the problem of battery. A SVCS controller is designed to control the buoy's surge velocity thanks to the UAV. In this work, the system was model in 2D first and will then be extended in 3D. The tether is considered inextensible and of negligible mass. Results are validated in simulation. However, in this solution, the tether is of constant length, which is not the case in our work. It is not dealing with take-off and landing, but it is presenting the control of the multicopter.

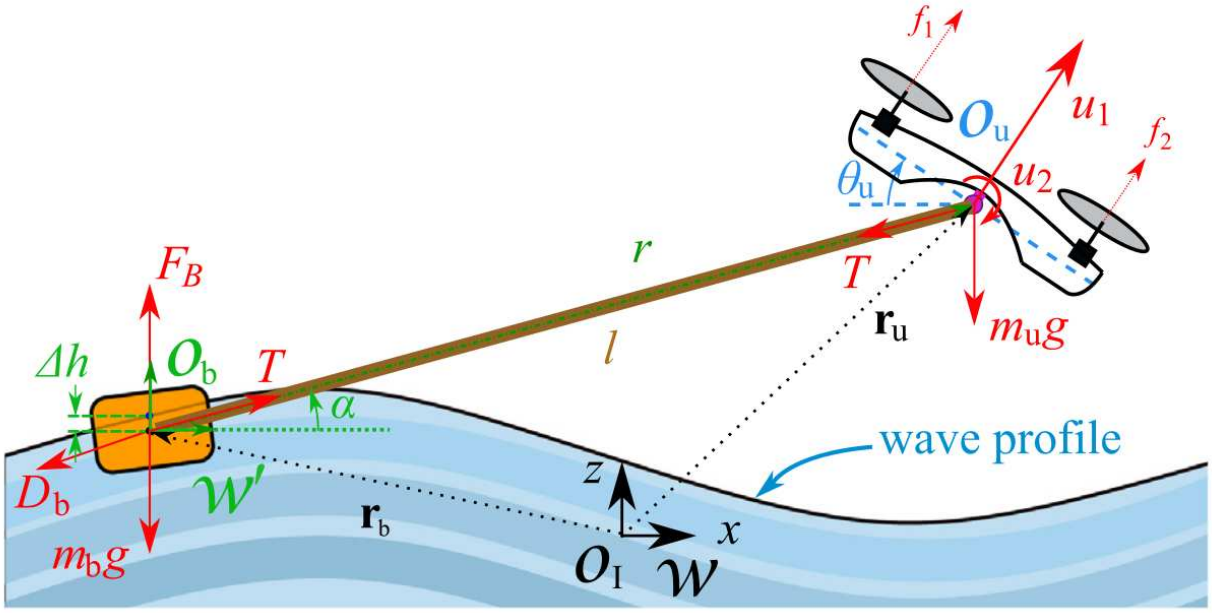

Figure 1.8 Marine locomotive quadrotor UAV. Source: [13]

In [14], a system composed of an aerial vehicle linked trough a tether to a ground station (Fig.1.9) is studied. The tether length is controlled thanks to the winch, and the objective is to keep the tether always taut. A strategy of inner and outer loop is used to control the system. In this work, the system is modeled in 2D. This work is closed to this thesis, however they have not taken into account the influence of the wind and the aerodynamic disturbances it can induce. Moreover, the strategy is validated only in simulation and the results seem not so good, either the system is fast but the tether is not taut or the tether remains taut but the system is slow.

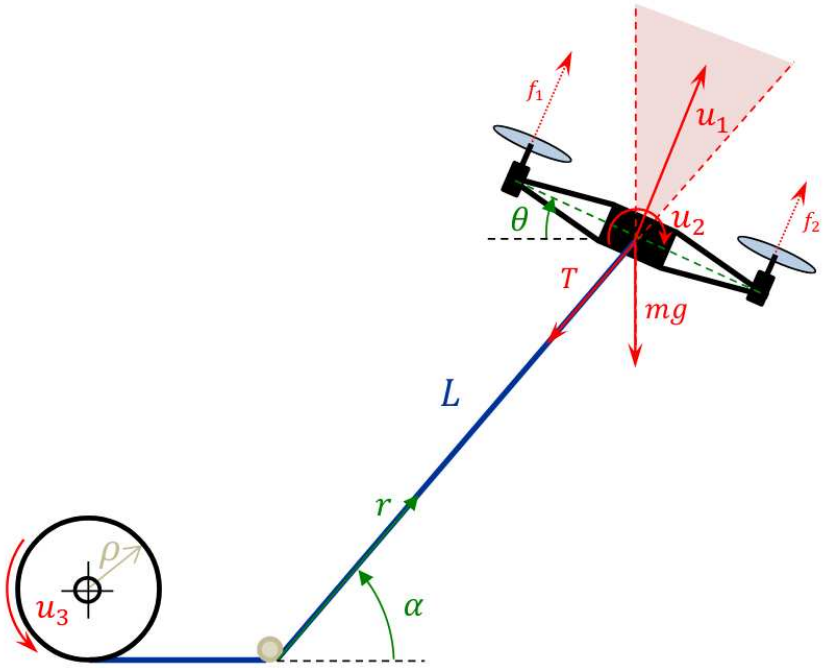

Figure 1.9 2D model of a tethered UAV with a taut tether. Source: [14]

In [15], the control of an aerial vehicle composed of a wing linked to the ground through a tether is presented (Fig.1.10). The aim of this work is to move the vehicle to a desired position while the tether remain taut. To do that, a nonlinear state feedback with a state dependent saturation using a Lyapunov method is designed. It is then tested in simulation with experimental aerodynamic data. In this work, the tether is assumed rigid, inextensible and mass-less. The only actuator available is the airfoil, this solution is suitable only under certain wind conditions. There is also no actuator for the tether, the control is unilateral.

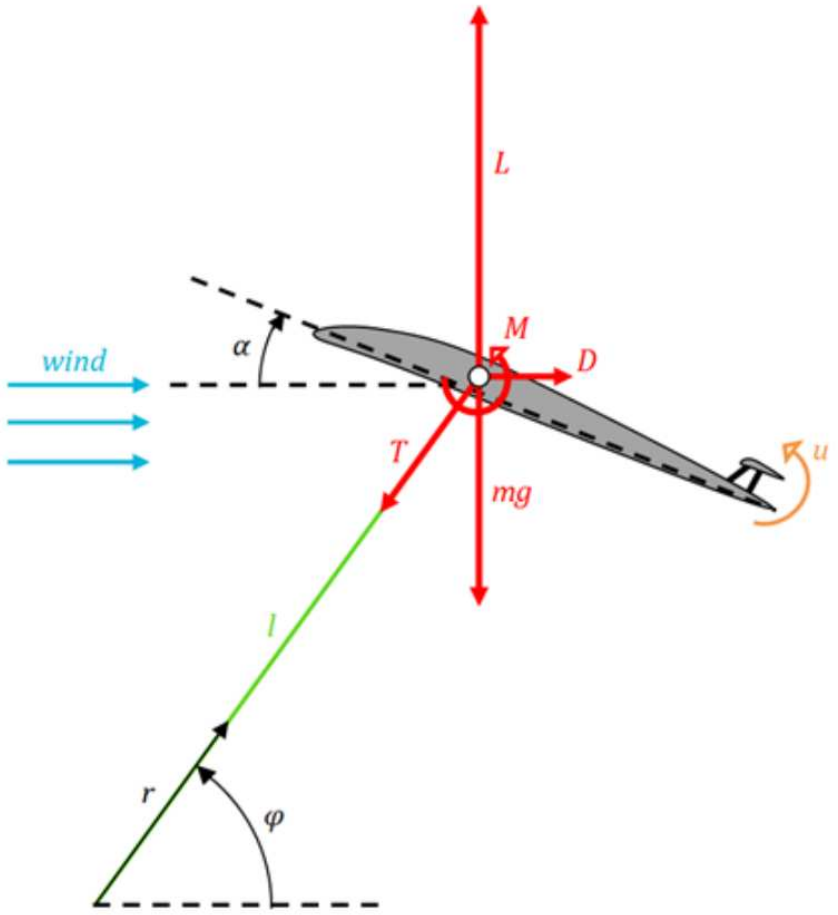

Figure 1.10 Aerial vehicle sustained by the wind. Source: [15]

In [16] a tether mathematical model is proposed (Fig.1.11), based on a finite element method and Lagrange's equation of motion. The tether is modelled in segments linked together, with the first segment of variable length and an additional virtual elements simulated to represent the multicopter. This model is then tested in simulation under wind disturbances and during take-off and hover manoeuvres. In this work, there is no mathematical model for the multicopter and there is no winch to control the tether tension. However the author projects to included it in further work.

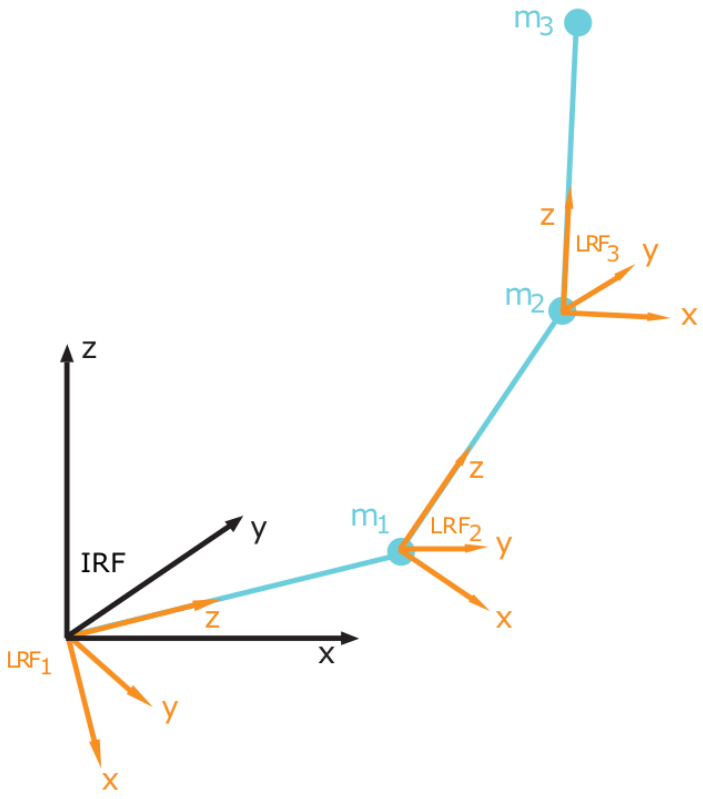

Figure 1.11 Example of tether model. Source: [16]

In [17], a solution to land on a inclined plane (Fig.1.12) is presented. A non linear model predictive control, with two layers is designed. It allows to have real time performance thanks to the two layers running at two different rates. One is looking for the possible trajectories, while the other one is applyied over the chosen trajectory. This controller is validated in simulation and is able to reject disturbances due to the wind and to deal with modelling errors. In this work, the tether is of fixed length and it only deals with the landing.

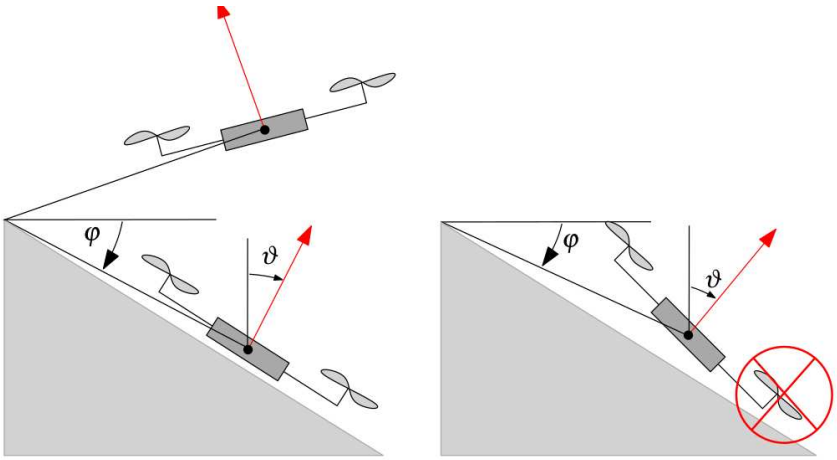

(a) *Correct landing* (b) *Wrong landing*

Figure 1.12 Landing on a inclined plane. Source: [17]

1.3 Context

This PhD study is the fourth one on the subject of AWE at Gipsa-lab [18]. The first one was done by Rogelio Lozano Jr. [19] [20] [21] from 2010 to 2014 on the study of the flight dynamics of a small scale kite, including indoor experimentation [22]. The second work was about relaxation-cycle power generation systems control optimization [23] and defended by Mariam Samir Ahmed [24] [25] [26] from 2010 to 2014. The last work was done by Yashank Gupta [27] [28] on the subject of Control of a Magnus-effect based Airborne wind energy system [29] from 2015 to 2018. These three subjects covered the modelling and the energy production of such system. However, the take-off and landing phases for the AWE systems were not studied in either work. This is the reason why we want to propose a solution answering to this need. Combining the different works done on AWE system at Gipsa-lab, a complete production cycle including a take-off, a production phase and a landing phase will be possible to achieve, and thus studied the system in its complete operation.

1.4 Objectives

In order to safely perform the take-off and landing phases of a drone-based AWE system, the objective is to steer it to a desired location (or position) in the air while maintaining the tether to a defined range of tension. To achieve that, a nonlinear multi-objectives controller is proposed to control simultaneously the drone and the on-ground winch. Since the main goal is to reach a target position and not to follow up closely a user-defined trajectory, a margin on the tracking error is tolerated while the system stays in a safety zone to avoid crashes.

1.5 Manuscript plan

The manuscript is organized in the following structure. Chapter 2 presents the system and its modelling. A mathematical model of the system is introduced. In Chapter 3 a control solution is proposed to answer the problem of take-off and landing of the system. It is then tested in simulation for different kind of systems and under different wind disturbances. An improvement to deal with the aerodynamic disturbances is proposed at the end of this chapter. This improvement involves the knowledge of the aerodynamic forces and this is why an estimator is designed in Chapter 4. The principal of extended Kalman filter is briefly introduced and then applied to the system. Simulation are run to validate the proposed estimator. Chapter 5 is dedicated to present experimental results of this thesis. First a presentation of the experimental test bench is done. Then some experimental results are discussed. This manuscript is concluded by Chapter 6 where conclusions on this work are presented and some perspectives are given.

Chapter Two

Modelling

The studied airborne wind energy (AWE) system is composed of two components: The first one is a flying device composed of a rigid wing with a multicopter or a drone and the second is an on-ground station. Both elements are connected by the means of a tether. In presence of wind, the flying device generates aerodynamic lift and drag forces. For on-ground AWE systems, the resultant traction force is transferred via the tether to an on-ground generator where a drum is used to convert the linear motion of the tether into shaft power, that is then used to drive a generator. A thrust force is generated by the drone attached to the flying device in order to control the trajectory of the system, especially in absence of wind. The different forces related to the drone that act on the system are considered as introduced in [20].

In our work, only the system motion in the vertical plane is considered, assuming that the system is aligned to the main wind direction and it is only subject to small variations in the third dimension. It is also assumed that the tether of length r forms a straight line. This assumption is acceptable for a taut tether of small length since in this case the linear mass is negligible. Otherwise, a tether model should be added in order to take into account its influence as presented in [30]. The tether has an elevation angle β with respect to the horizontal plane. The combined mass of all airborne system components is denoted by M_M.

In order to establish the model, all the forces acting on the system have to be expressed.

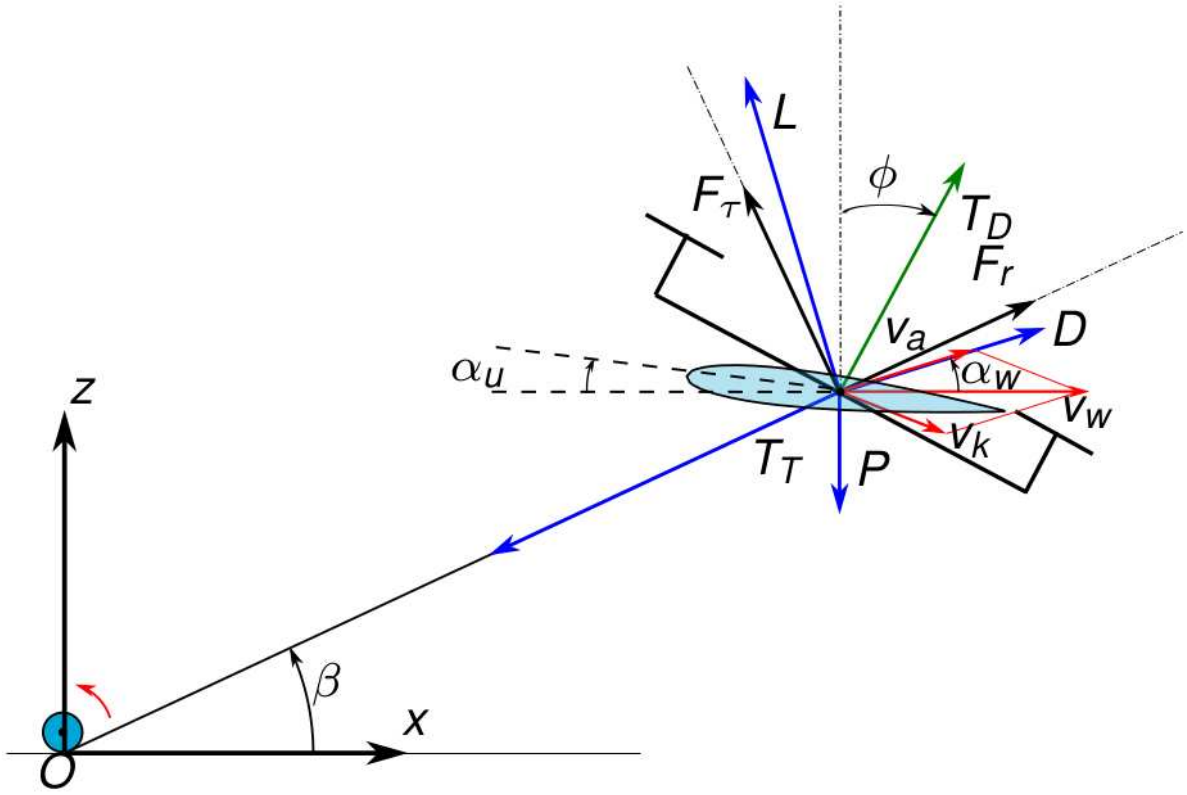

Figure 2.1 The airborne wind energy system with the drone connected to the on-ground station. All forces acting on the system are shown.

Figure 2.1 gives a general overview of the considered system where all forces acting on the system are represented as the aerodynamic forces, L and D, the weight P, the tether tension T_T and the thrust of the drone T_D.

We will consider all the aerodynamic forces generated by the wing in presence of wind. These forces depend on the aerodynamic properties of the wing and its profile. The lift and drag forces can be expressed by:

$$L = \frac{1}{2}\rho S v_a^2 C_L, \quad D = \frac{1}{2}\rho S v_a^2 C_D \tag{2.1}$$

where ρ is the air density, v_a is the apparent wind velocity, S is the considered wing surface, C_L and C_D are respectively aerodynamic lift and drag coefficients. For classical airfoils, in order to determine these coefficients, one can refer to the aerodynamic coefficient curves of Figure 2.2, generated from the mathematical model borrowed from [31].

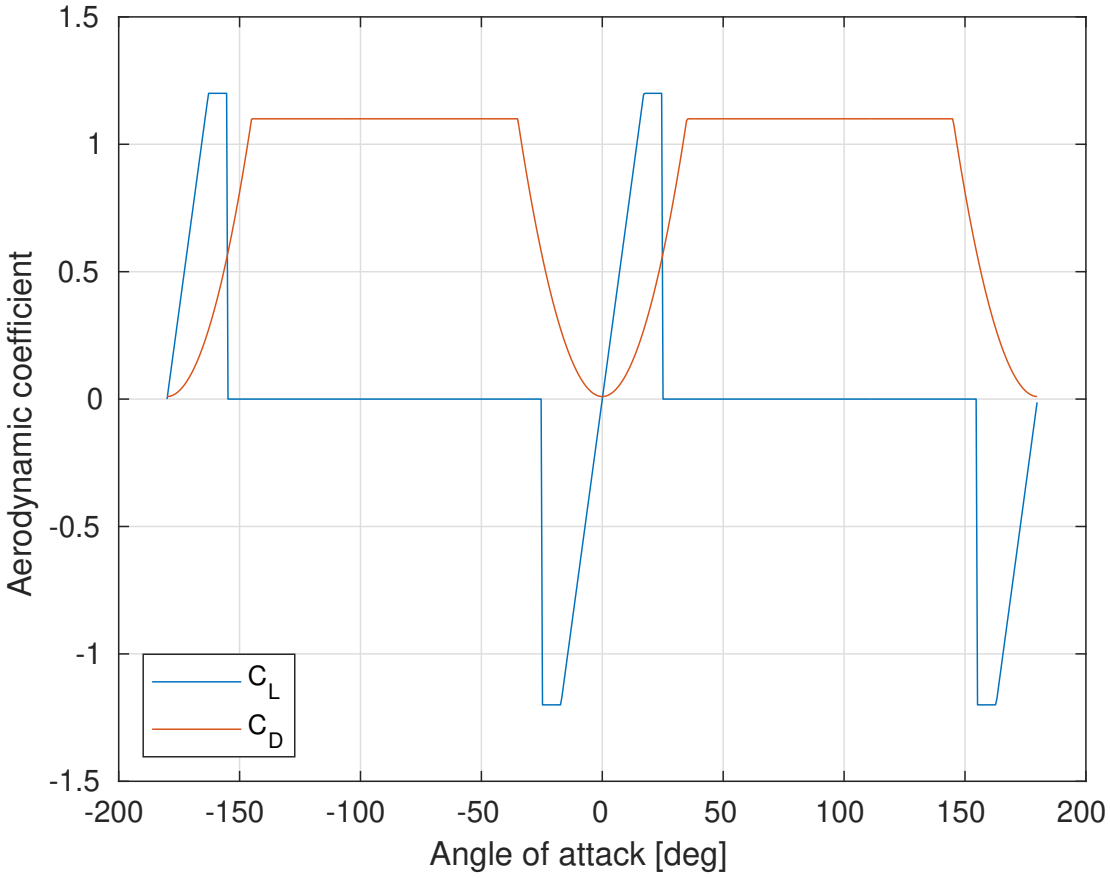

Figure 2.2 Model of aerodynamic coefficient C_L and C_D in function of the wing's angle of attack for a classical airfoil.

As it is shown in Figure 2.1, D is aligned in the direction of apparent wind v_a and L is orthogonal to it. The angle of attack α_a can be defined from the pitch angle α_u determined with respect to the horizon and the relative wind orientation α_w with the following equation:

$$\alpha_a = \alpha_w - \alpha_u \tag{2.2}$$

The apparent wind velocity $\vec{v}_a$ is defined by:

$$\vec{v}_a = \vec{v}_w - \vec{v}_k \tag{2.3}$$

where $\vec{v}_k$ is the translation velocity of the flying device and $\vec{v}_w$ is the wind speed. Several wing configurations can be studied. Notice that, the absence of an actuator that links the

drone to the wing leads to a fixed relative angle, and α_u expressed as:

$$\alpha_u = \phi + \alpha_D \tag{2.4}$$

where α_D is a fixed design value and ϕ the inclination angle of the drone. The configurations of the system for two different values of α_D are presented in Figure 2.3.

Figure 2.3 Examples of fixed configuration between the wing and the drone. Left figure corresponds to $\alpha_D = 0$, and right figure corresponds to another configuration where $\alpha_D = \pi/2$.

Another type of wing studied here is the Magnus wing (Fig.2.4) case that consists of a rotating cylinder instead of a classical airfoil. The advantage this type of wing is that the aerodynamic coefficients C_L and C_D only depend on the spin ratio X. A model of evolution of these coefficients with respect to X is presented in Equation 2.5 and detailed in [27].

$$\begin{aligned} C_L &= 0.0126X^4 - 0.2004X^3 + 0.7482X^2 + 1.3447X \\ C_D &= -0.0211X^3 + 0.1873X^2 + 0.1183X + 0.5 \\ X &= \frac{\omega_{cyl} r_{cyl}}{v_a} \end{aligned} \tag{2.5}$$

where r_{cyl} is the radius of the Magnus rotor and ω_{cyl} the Magnus rotor angular velocity.

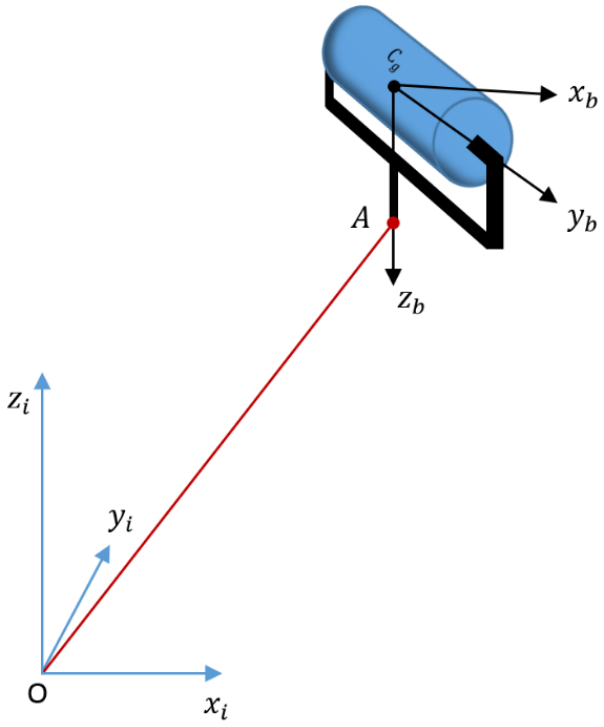

Figure 2.4 Model of the system with a Magnus wing. Source: [27]

For the drone attached to the rigid wing, the following equation is used to express its closed-loop dynamics model :

$$\dot{T}_D = \frac{1}{\tau_{T_D}}\Big(T_D^d - T_D\Big), \quad \dot{\phi} = \frac{1}{\tau_\phi}\Big(\phi^d - \phi\Big) \tag{2.6}$$

where T_D^d and ϕ^d are the desired thrust and inclination angle sent to the drone, and τ_{T_D} and τ_ϕ are the time constants of the first order systems in Equation 2.6. One can add a third equation, that is the dynamical equation of the on-ground generator traction force:

$$\dot{T} \;=\; \frac{1}{\tau_T}\Big(u_r^d - T\Big) \tag{2.7}$$

where u_r^d is the desired traction force, used to control tether length r, T is the effective torque of the drum divided by its radius R_d and τ_T is the time constant of the dynamic system considered as a first order system.

The tether tension T_T can be calculated using:

$$T_T = T + M_D\ddot{r} + \Gamma_S \tag{2.8}$$

where Γ_S represents the dry friction of the on-ground winch and $M_D = \frac{I}{R_d^2}$ is expressed in function of the inertia moment of the on-ground generator I and its radius R_d.

The fundamental principle of dynamics is applied to establish a dynamical model of the flying device illustrated in Figure 2.1. Considering the system's two degrees of freedom, r and β, translation velocity of the flying device $\vec{v}_k$ can be decomposed into a radial velocity component $v_{k,r} = \dot{r}$ and a tangential velocity component $v_{k,\tau} = r\dot{\beta}$. As done in [32], differentiation of $\vec{v}_k$ with respect to time yields a radial acceleration component and a tangential acceleration component:

$$\frac{dv_{k,r}}{dt} = \ddot{r} - r\dot{\beta}^2, \quad \frac{dv_{k,\tau}}{dt} = r\ddot{\beta} + 2\dot{r}\dot{\beta} \tag{2.9}$$

As illustrated on Figure 2.1, the resultant forces F_r and F_τ are respectively the radial and tangential force components according to the polar coordinate system (r,β).

$$F_r = -T + \Gamma_S + L\sin(\beta - \alpha_w) + D\cos(\beta - \alpha_w) - P\sin\beta - T_D\sin(\phi - \beta) \tag{2.10}$$

$$F_\tau = L\cos(\beta - \alpha_w) - D\sin(\beta - \alpha_w) - P\cos\beta + T_D\cos(\phi - \beta) \tag{2.11}$$

where α_w is the angle that the apparent wind velocity forms with the horizontal. It can be calculated with the formula of [31]:

$$\alpha_w = \arctan\frac{r\cos(\beta)\dot{\beta} + \dot{r}\sin(\beta)}{v_w + r\sin(\beta)\dot{\beta} - \dot{r}\cos(\beta)} \tag{2.12}$$

Thus, a dynamical model of this system can be derived in 2D polar coordinates:

$$\ddot{r} = \frac{1}{M_M + M_D}\Big[r\dot{\beta}^2 M_M + F_r\Big] \tag{2.13}$$

$$\ddot{\beta} = \frac{1}{r}\Big[-2\dot{\beta}\dot{r} + \frac{F_\tau}{M_M}\Big] \tag{2.14}$$

To summarize, the overall nonlinear model of the system can be written as:

$$
\begin{aligned}
\ddot{r} &= \frac{1}{M_M + M_D}\Big[r\dot{\beta}^2 M_M - T + \Gamma_S - P\sin(\beta) + u_{T_0} + L\sin(\beta - \alpha_w) \\
&\quad + D\cos(\beta - \alpha_w)\Big] \\
\ddot{\beta} &= \frac{1}{r}\Big[-2\dot{\beta}\dot{r} + \frac{1}{M_M}(-P\cos(\beta) + u_\beta + L\cos(\beta - \alpha_w) - D\sin(\beta - \alpha_w))\Big] \\
\dot{T} &= \frac{1}{\tau_T}\Big(u_r^d - T\Big) \\
u_{T_0} &= -T_D sin(\phi - \beta) \\
u_\beta &= T_D cos(\phi - \beta) \\
\dot{T}_D &= \frac{1}{\tau_{T_D}}\Big(T_D^d - T_D\Big) \\
\dot{\phi} &= \frac{1}{\tau_\phi}\Big(\phi^d - \phi\Big) \\
T_T &= T + M_D\ddot{r} + \Gamma_S
\end{aligned}
\tag{2.15}
$$

Drone inputs are computed from u_{T_0} and u_β that are used to control the elevation angle β and the tether tension T_T, respectively. Note that in Equation 2.15 there are two actuators, T and u_{T_0} in order to control two variables: r and T_T. The winch torque T, the faster and more precise actuator, is then used to control r, that is a more critical variable of the system than tether tension T_T, that has just to be maintained positive and thus it is controlled with the thrust generated by the drone. The open-loop system can be summarized with the block diagrams for both wing cases represented in Figure 2.5.

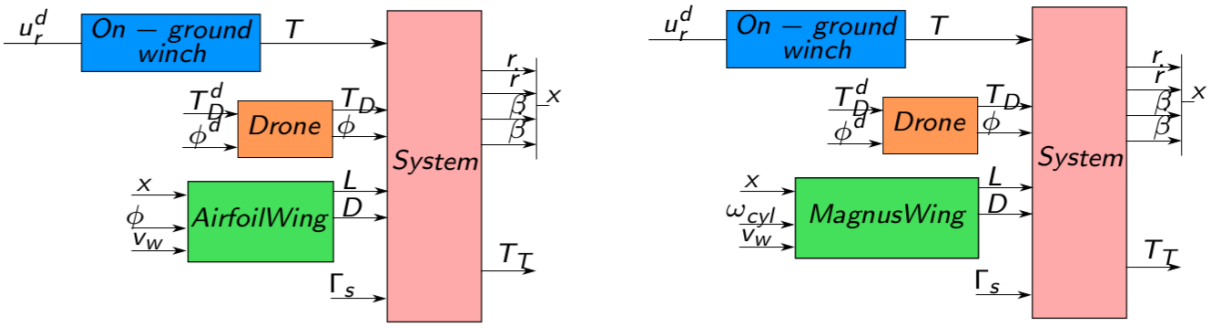

Figure 2.5 Block diagram of the open-loop system, on the left the airfoil case and on the right the Magnus wing case.

Chapter Three

Controller design

Once the system is modeled, a controller can be designed. In section 3.1, an overview of the proposed controller is presented with a block diagram. The theory of the chosen control method is explained in Section 3.2. It is then applied to the system in Section 3.3 and Section 3.4. The designed controller is then tested in simulation on different kind of system in Section 3.6. The obtained results are then improved by integrating the aerodynamic forces in Section 3.7.

3.1 Control scheme overview

The block diagram in Figure 3.1 shows the different stages to be carried out to perform the control action. The "Drone" block corresponds to the drone that has its own internal control loops and can be modelled by the simplified model of Equation 2.6. The "Wing" block corresponds to the whole flying part that can be modeled by Equations 2.13, 2.14, 2.1 and data from Figure 2.2. The block Feedback Linearization is detailed in section 3.2. In section 3.3, the design of the nonlinear controller with integral action is presented. The static equation used to compute u_{T0} can be found in section 3.4.

The block MIX allows to transform the inputs u_β and u_{T_0} in the desired setpoints of the drone, T_D^d and ϕ^d. This nonlinear static operator is implemented by the following simple

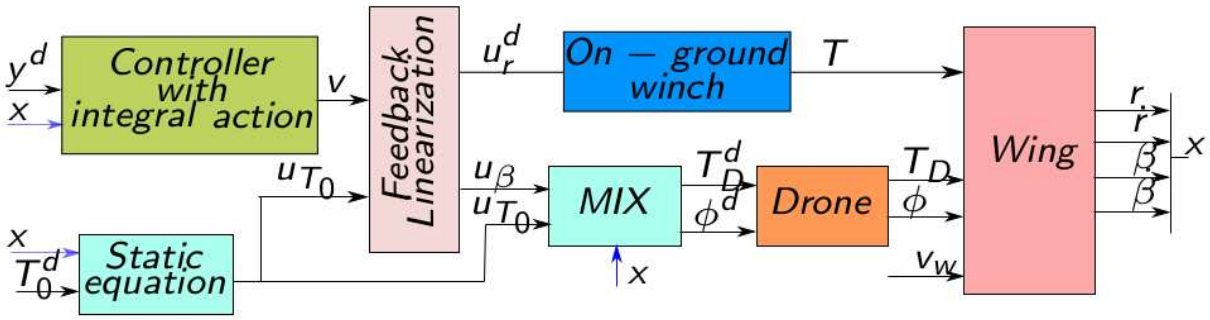

Figure 3.1 Block diagram of the control strategy.

expressions:

$$T_D^d = \sqrt{u_{T_0}^2 + u_\beta^2}$$
$$\phi^d = atan\left(-\frac{u_{T_0}}{u_\beta}\right) + \beta \tag{3.1}$$

However this transformation is improved in section 3.8 to deal with the influence of aerodynamics forces.

3.2 Feedback linearization

The output feedback linearization method [33] allows to control nonlinear systems. The method consists in transforming a nonlinear tracking problem to a simple stabilizing problem. The first step is to find the relative degree of the system, it corresponds to the number of times one needs to differentiate the output before the input appears explicitly. This method can be applied to a nonlinear system which is affine to the input as the following one:

$$\begin{aligned} \dot{x} &= f(x) + g(x)u \\ y &= h(x) \end{aligned} \tag{3.2}$$

with x the state vector , u the input vector and y the output vector.
However, every nonlinear system can be written in this form by adding an integrator before the system and extending the state.

By differentiating the output as many time as the relative degree k_m, the following equation is obtained :

$$\begin{pmatrix} y_1^{(k_1)} \\ ... \\ y_m^{(k_m)} \end{pmatrix} = A(x)u + b(x) \tag{3.3}$$

$\begin{pmatrix} y_1^{(k_1)} \\ ... \\ y_m^{(k_m)} \end{pmatrix}$ can be chosen equal to v which will be computed thanks to a linear intermediate control law. Under the hypothesis that the matrix $A(x)$ is invertible, the nonlinear control law is defined by:

$$u = A^{-1}(x)(v - b(x)) \tag{3.4}$$

This method is applied to the tethered drone system on a simplified model detailed hereafter:

$$\dot{x} = \begin{pmatrix} \dot{r} \\ \frac{1}{M_M+M_D}\Big[r\dot{\beta}^2 M_M + (-u_r^d - P\sin(\beta) + u_{T_0})\Big] \\ \dot{\beta} \\ \frac{1}{r}\Big[-2\dot{\beta}\dot{r} + \frac{1}{M_M}(-P\cos(\beta) + u_\beta)\Big] \end{pmatrix} \tag{3.5}$$

Note that friction and aerodynamic forces are neglected in this simplified model and thus considered as disturbances. The dynamics of the on-ground generator traction force is also neglected leading to the following equation: $T = u_r^d$.

The external and internal variables of this system are defined as follows:

Input vector

$$u = \begin{pmatrix} u_r^d & u_\beta \end{pmatrix}^T \tag{3.6}$$

Output vector

$$y = \begin{pmatrix} r & \beta \end{pmatrix}^T \tag{3.7}$$

State vector

$$x = \begin{pmatrix} r & \dot{r} & \beta & \dot{\beta} \end{pmatrix}^T \tag{3.8}$$

As it can be clearly shown, the relative degree of the system is 2.

$$y = \begin{pmatrix} 1 & 0 & 0 & 0 \\ 0 & 0 & 1 & 0 \end{pmatrix} x \tag{3.9}$$

$$\dot{y} = \begin{pmatrix} \dot{r} \\ \dot{\beta} \end{pmatrix} = \begin{pmatrix} 0 & 1 & 0 & 0 \\ 0 & 0 & 0 & 1 \end{pmatrix} x \tag{3.10}$$

$$\ddot{y} = \underbrace{\begin{pmatrix} \frac{1}{M_M+M_D}\left[r\dot{\beta}^2 M_M - P\sin(\beta) + u_{T_0}\right] \\ \frac{1}{r}\left[-2\dot{\beta}\dot{r} - \frac{P}{M_M}\cos(\beta)\right] \end{pmatrix}}_{b(x)} + \underbrace{\begin{pmatrix} -\frac{1}{M_M+M_D} & 0 \\ 0 & \frac{1}{M_M}\frac{1}{r} \end{pmatrix}}_{A(x)} \underbrace{\begin{pmatrix} u_r^d \\ u_\beta \end{pmatrix}}_{u} \tag{3.11}$$

From Equation 3.11, one gets that $\ddot{y}$ is affine with respect to the input u. Under the hypothesis that the matrix $A(x)$ is invertible, which is the case in our operating range, the nonlinear control law defined by:

$$u = A^{-1}(x)(v - b(x)) \tag{3.12}$$

reduces the nonlinear system's dynamics to the dynamics of a double integrator $\ddot{y} = v$ with v the linear intermediate control law.

3.3 Linear control law

Once the problem to solve is linear, a linear control law has to be designed. Different methods have been tested for the design of v: A linear quadratic regulator and a multi-variable proportional-integral-derivative controller.

3.3.1 Multi-variable proportional-integral-derivative controller

For the multi-variable proportional-integral-derivative controller, $v = \begin{pmatrix} v_r \\ v_\beta \end{pmatrix}$ with

$$v_r = \alpha_{r_{-1}} \int_0^t e_r(\tau)\,\mathrm{d}\tau + \alpha_{r0}\ e_r + \alpha_{r1}\ \dot{e_r} + \ddot{y}_r^d \tag{3.13}$$

$$v_\beta = \alpha_{\beta_{-1}} \int_0^t e_\beta(\tau)\,\mathrm{d}\tau + \alpha_{\beta 0}\ e_\beta + \alpha_{\beta 1}\ \dot{e_\beta} + \ddot{y}_\beta^d \tag{3.14}$$

where $y^d = [y_r^d\ y_\beta^d]^T$ is the vector of the desired setpoints, $e = (y^d - y)$ is the vector of tracking error. Note that the integral term is added in order to improve the robustness of the controller. In particular, to be able to reject disturbances and to compensate the modelling error, for instance the non considered lift and drag forces in Equation 3.5. The Integral of the Time weighted Absolute Error (ITAE) [34] [35] performance index is used in order to tune the controller parameters. It allows to specify the dynamic response with relatively small overshoot and relatively little oscillation. The used characteristic polynomial is

$$P(s) = s^3 + 1.783 w_n s^2 + 2.172 {w_n}^2 s + {w_n}^3 \tag{3.15}$$

with w_n the natural frequency of the closed-loop system. Note that, by this choice one can get a stable linear tracking error with a desired converging rate. To compensate oscillations of the reel-in and reel-out speeds $\dot{r}$ due to error on the simplified model, the derivative coefficient is increased by 20%, giving $\alpha_{r1} = 2.1396 w_n$. This value has been found experimentally based on several experiments made on the test-bench.

3.4 Static Equation

For the design of u_{T_0}, we have chosen to use an open loop control with a simple feedforward compensation of the weight:

$$u_{T_0} = T_0^d + P\sin(\beta) \tag{3.16}$$

At the equilibrium position, u_{T_0} has to compensate the weight and to ensure the desired tension in the tether. By decomposing the action of the drone into a radial component and tangential one, it is important to mention that the radial part u_{T_0} enters directly in concurrence with the winch's torque that controls r. This simple law allows to obtain a thrust force that will smoothly maintain the minimum desired tension in the tether without perturbing the control law on r, as long as the thrust is well calibrated. This calibration is detailed in Subsection 5.3.6. This choice has been done in order to study properly the control law on r, nevertheless, a more advanced control law can be designed for this part in order to track faster and more precisely the tether tension.

3.5 Integration of delay

To compensate the delay due to the response time of drone actuators, a transformation is also made in the MIX block:

$$T_{Dcompensated} = T_D^d + \tau_{T_D} \dot{T_D^d} \tag{3.17}$$

$$\phi_{compensated} = \phi^d + \tau_\phi \dot{\phi^d} \tag{3.18}$$

where τ_{T_D} and τ_ϕ are the identified time response of the drone actuators. A prediction using an Euler model is done. To obtain $\dot{T_D^d}$ and $\dot{\phi^d}$ a finite difference approximations method is used.

3.6 Simulation results

Simulations of the proposed control strategy are tested on a scenario including a take-off and a landing. During all the scenario the desired tension in the tether T_0^d is set to $1.5N$. The scenario is defined as follows:

- Initial position: The system starts from its initial position at $r_0 = 0.4m$, $\beta_0 = 20°$, $T_{D_0} = 0N$ and $\phi_0 = 0$.

- Take-off phase: At $t = 0$ s the reference signal r_d goes from r_0 to $r_f = 1.2m$ with a ramp rate of $0.08m/s$, and the desired elevation angle β_d goes from β_0 to $\beta_f = 45°$ with a ramp rate of $0.5\ °/s$.

- Landing phase: At $t = 25$ s the reference signal r_d goes from r_f to r_0 with a ramp rate of $0.08m/s$, and the desired elevation angle β_d goes from β_f to β_0 with a ramp rate of $0.5\ °/s$.

- End of the scenario : Once the system is landed, the drone is back to its initial position and ready to start a new cycle.

Table 3.1 Parameters of the controller

Symbol	Name	Value
ω_{nr}	Natural frequency for the r loop	5 rad/s
$\omega_{n\beta}$	Natural frequency for β loop	3 rad/s

The value of the parameters of the controller are given in Table 3.1. The value of w_{n_r} is higher than w_{n_β} since it is assume that the control loop in r is faster than that of β.

The parameter of the simulation are given in Table 3.2. Some of these parameters are identified from experimental results presented in Chapter 5. The parameters are chosen in order to have a simulation as close as possible to the experimentation. Parameters used in compensation equations are chosen slightly different from those used in the model in order to take into account the modeling error. Next subsections present simulation results for configurations shown in Figure 2.3, Magnus wing case and different wind conditions. Fisrt $\alpha_D = 0$ with no wind, then the same configuration with $v = 6m/s$. Next subsections presents the obtained results respectively for $\alpha_D = \frac{\pi}{2}$ and Magnus wing case, both with the same wind

Table 3.2 Physical Parameters

Symbol	Name	Value
M_M	Mass of airborne subsystem	0.774 kg
M_D	Ground station rotor mass	0.0481 kg
S	Wing area	0.09 m^2
α_D	Wing configuration angle	0 deg
ρ	Air density	1.225 kg/m^3
τ_T	Time constant of motor current loop	0.02 s
τ_{T_D}	Time constant of drone thrust loop	0.085 s
τ_ϕ	Time constant of drone inclination loop	0.194 s
u_{rmin}	Minimum tension in the winch	0 N
u_{rmax}	Maximum tension in the winch	8 N
T_{Dmin}	Minimum drone's thrust	0 N
T_{Dmax}	Maximum drone's thrust	17.7 N
ϕ_{min}	Minimum drone's inclination angle	-50 deg
ϕ_{max}	Maximum drone's inclination angle	50 deg

condition $v = 6m/s$. Subsection 3.6.5 will conclude on simulations results obtained with this control approach for these scenarios.

3.6.1 Case with $\alpha_D = 0°$ and $v = 0m/s$

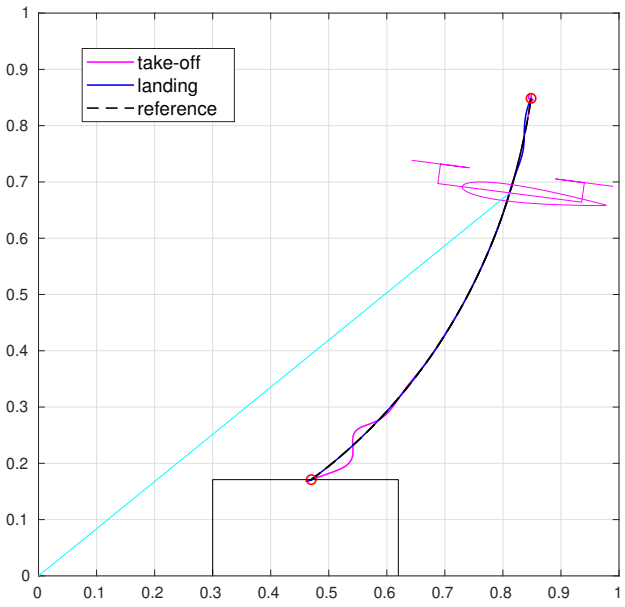

Figure 3.2 Trajectory of the system for $\alpha_D = 0°$ and $v = 0m/s$

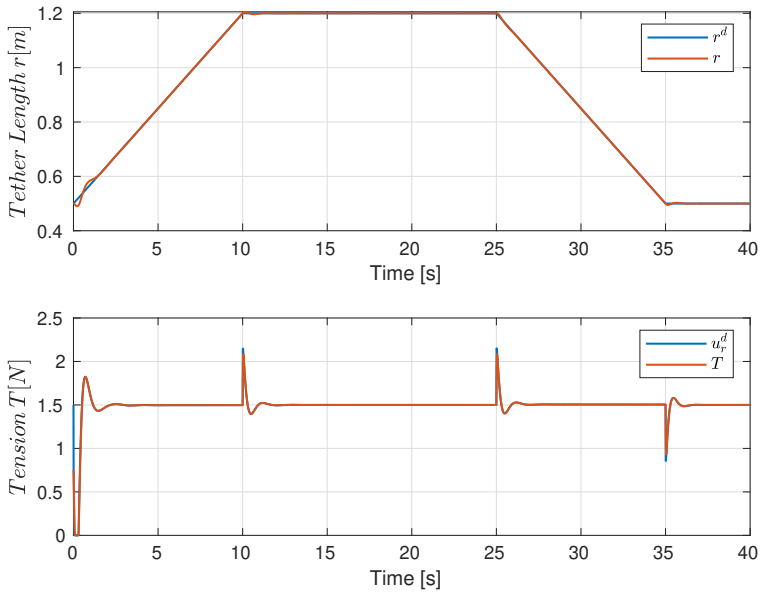

Figure 3.3 Evolution of the tether length r for $\alpha_D = 0°$ and $v = 0m/s$

Figures 3.3 and 3.4 show that the tether length r and the elevation angle β follow well their references. This is confirmed by the trajectory of the drone which is closed to the reference

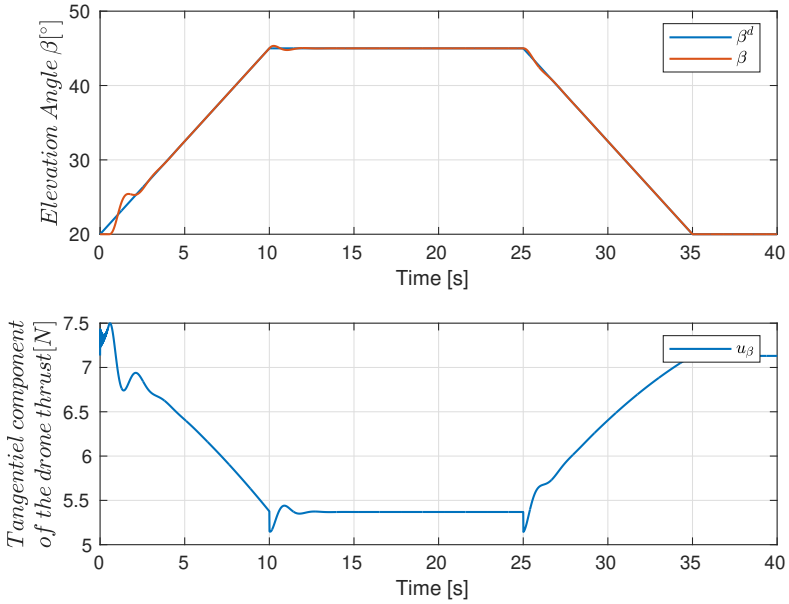

Figure 3.4 Evolution of the elevation angle β for $\alpha_D = 0°$ and $v = 0m/s$

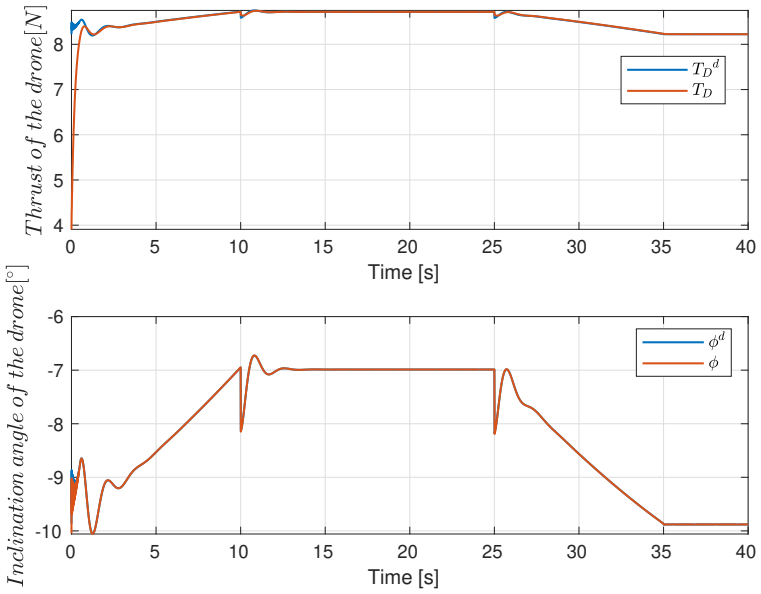

Figure 3.5 Evolution of drone inputs for $\alpha_D = 0°$ and $v = 0m/s$

as shown in Figure 3.2. The tether tension illustrated in Figure 3.6 is at its reference value except when the system starts a motion, for example at the beginning of the landing phase. But it goes back to this value in a short time and never goes close to $0N$ which will be

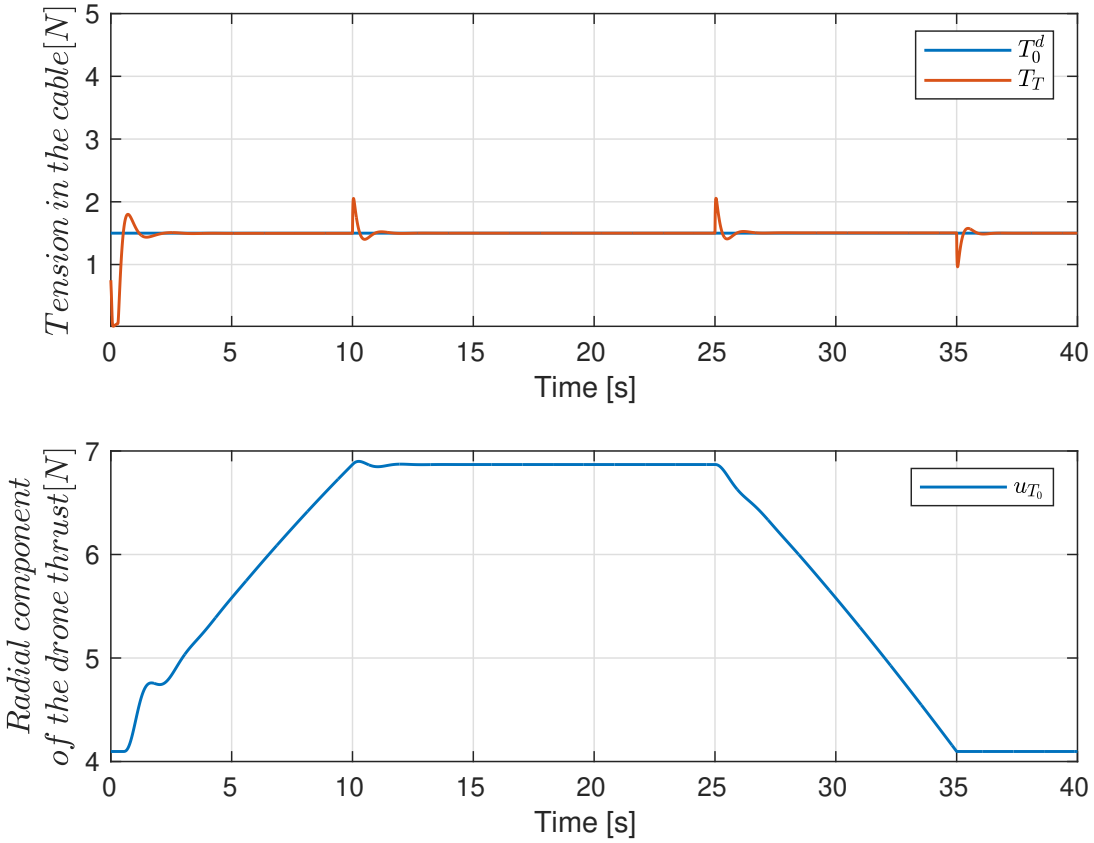

Figure 3.6 Evolution of tether tension T_T for $\alpha_D = 0°$ and $v = 0m/s$

synonym of a lost of tension in the tether. The inputs of the drone can be seen on Figure 3.5.

3.6.2 Case with $\alpha_D = 0°$ and $v = 6m/s$

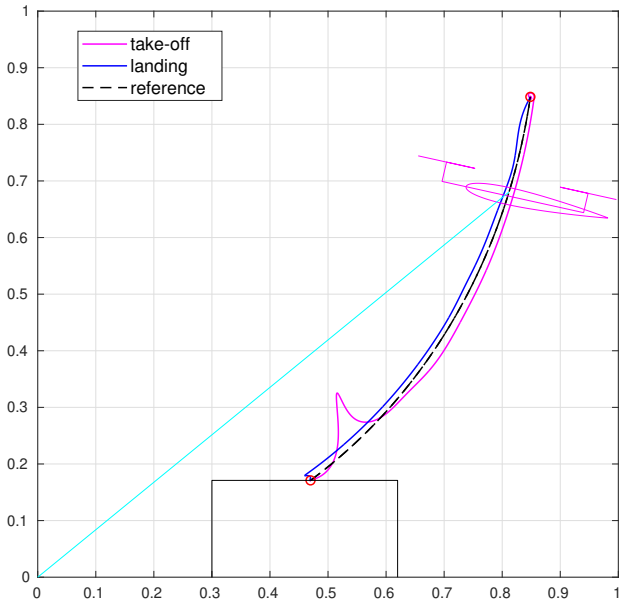

Figure 3.7 Trajectory of the system for $\alpha_D = 0°$ and $v = 6m/s$

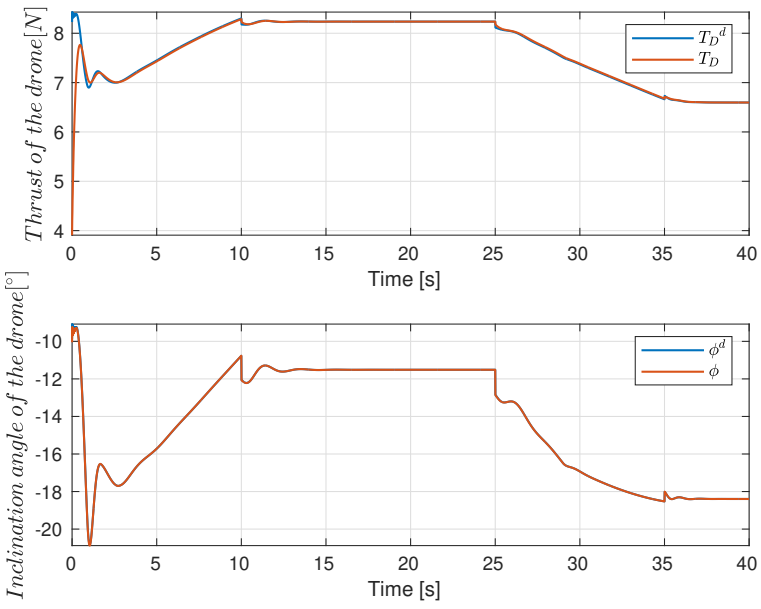

Figure 3.8 Evolution of drone inputs T_D and ϕ for $\alpha_D = 0°$ and $v = 6m/s$

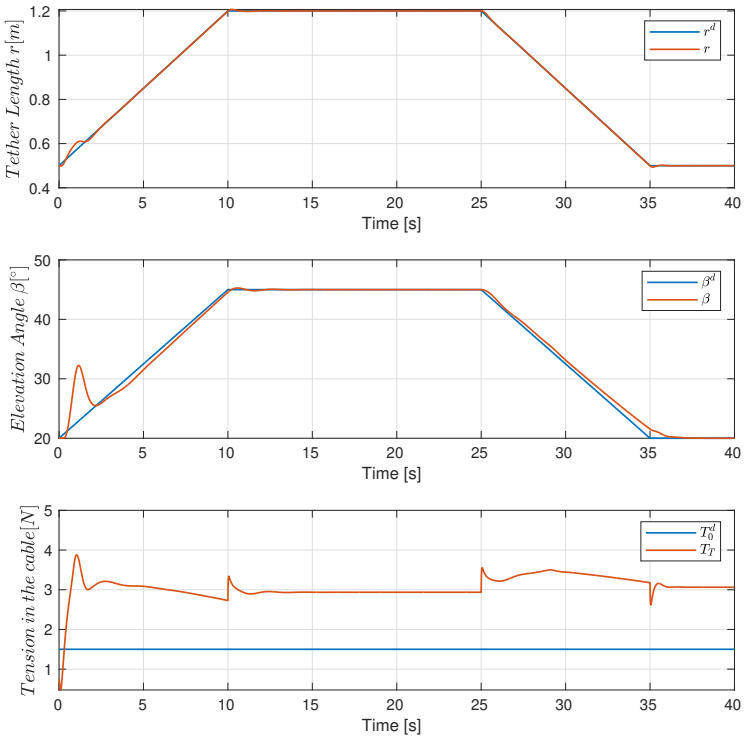

Figure 3.9 Evolution of the states r, β and T_T for $\alpha_D = 0°$ and $v = 6m/s$

For a wind of $6m/s$, the trajectory on Figure 3.7 shows an important overshoot at the beginning of the take-off and during all the trajectory a tracking error can be observed. The same observation can be made on the evolution of r and β on Figure 3.9. As the tether tension is controlled with an open-loop strategy, it is always above the desired value because of the extra tension due to the perturbing lift and drag forces. However, since the objective is to always have a taut tether, this is not a problem for the system to have a higher tether tension. The disadvantage of this higher tension will be a higher consumption by the on-ground winch and the drone. This can be solved by using a closed loop control on T_T. Figure 3.8 shows that the inclination angle ϕ is higher to compensate the wind and the drone thrust is slightly inferior to the case with no wind, this is a consequence of the presence of the lift force that helps the drone to support the overall weight.

3.6.3 Case with $\alpha_D = \frac{\pi}{2}$ and $v = 6m/s$

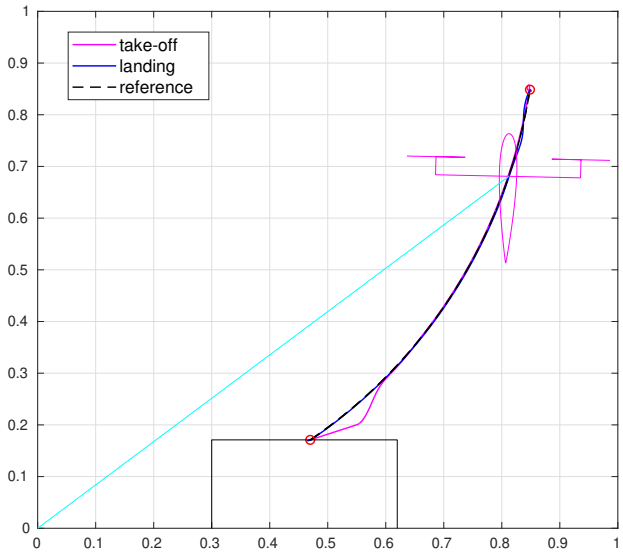

Figure 3.10 Trajectory of the system for $\alpha_D = \frac{\pi}{2}$ and $v = 6m/s$

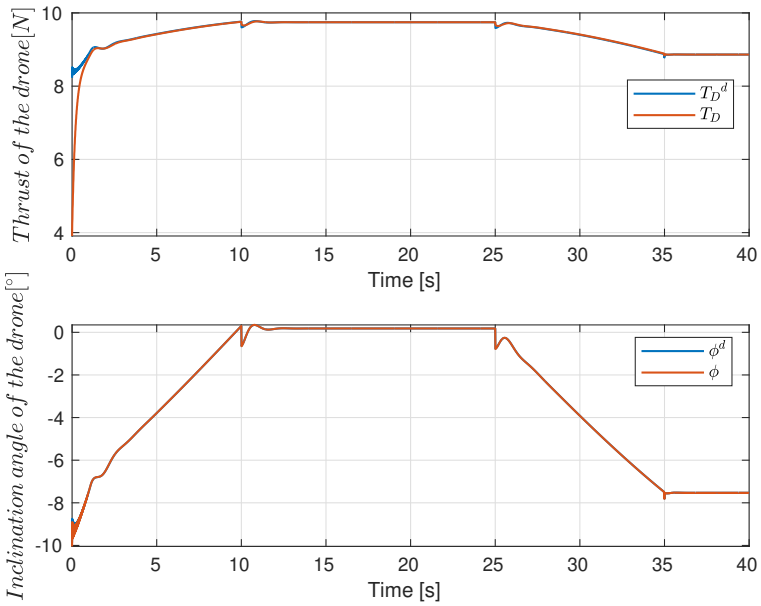

Figure 3.11 Evolution of drone inputs T_D and ϕ for $\alpha_D = \frac{\pi}{2}$ and $v = 6m/s$

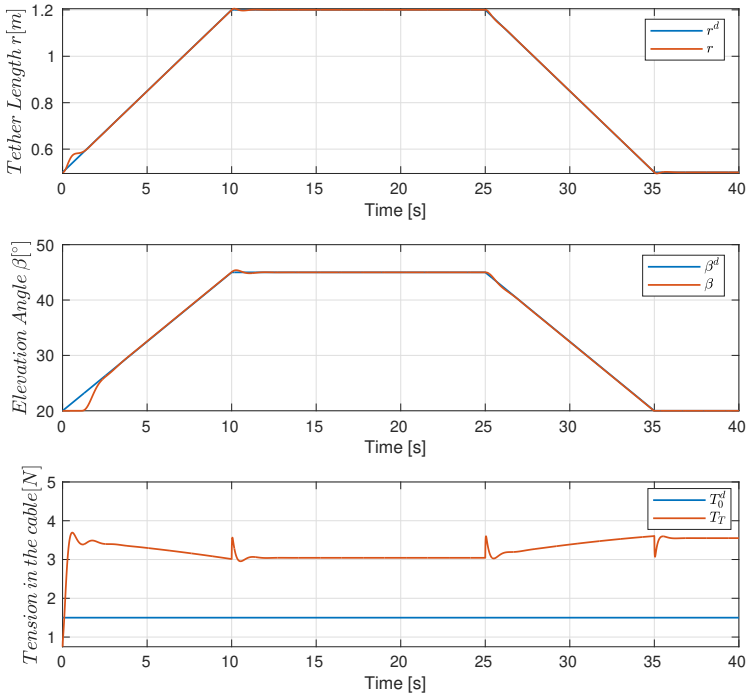

Figure 3.12 Evolution of the states r, β and T_T for $\alpha_D = \frac{\pi}{2}$ and $v = 6m/s$

In this configuration, the wing is orthogonal to the drone, it corresponds to $\alpha_D = \frac{\pi}{2}$. Figures 3.10, 3.12 and 3.11 show that the system is less impacted by the wind at the beginning of the take-off phase and during the trajectory there is no tracking error. On Figure 3.11, the inclination angle is around $0°$ against $-12°$ in the other configuration. The thrust is also higher in this case. This is due to the influence of the aerodynamic forces which in this configuration is mainly composed by the drag force that produces a downward additional force, and no lift force to compensate it.

Note that for $\alpha_D = \frac{\pi}{2}$ configuration, the absence of lift force in take-off and land phases leads to a drone thrust that has to increase with wind speed. This could lead to the saturation of the drone thrust for larger wind speed that will lead to the impossibility to stabilize the system at a given elevation angle.

3.6.4 Magnus wing for $v = 6m/s$

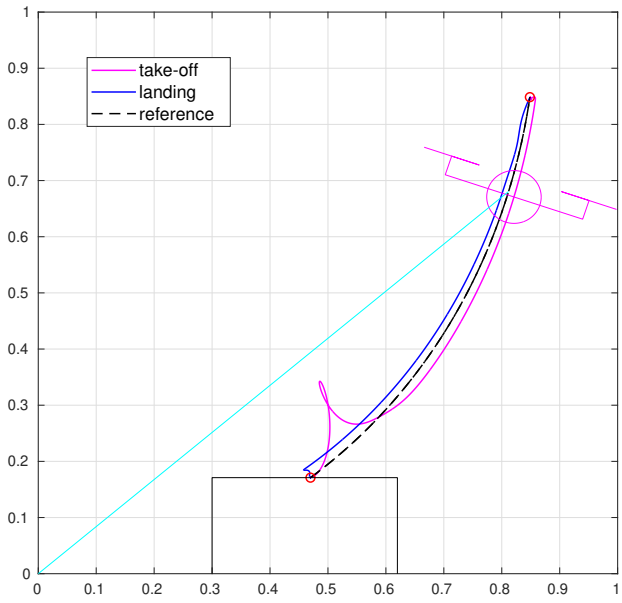

Figure 3.13 Trajectory of the system for a Magnus wing and $v = 6m/s$

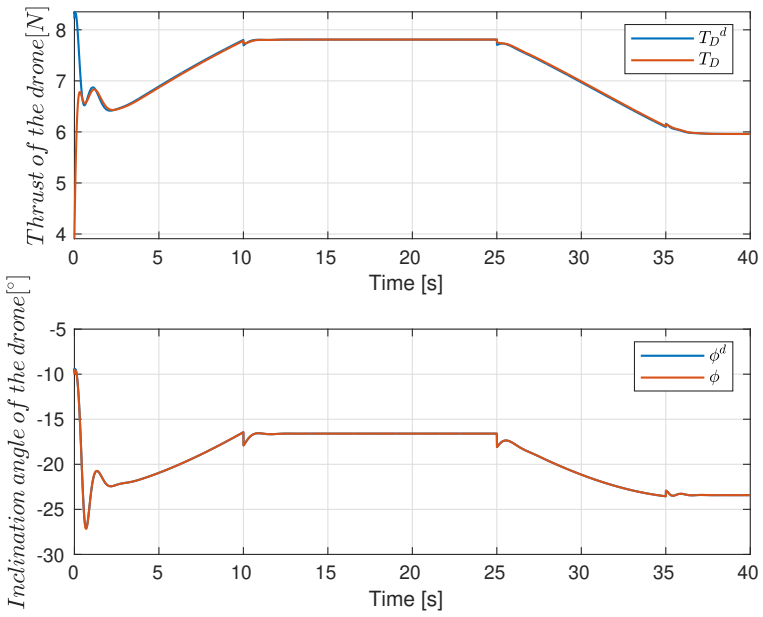

Figure 3.14 Evolution of drone inputs T_D and ϕ for a Magnus wing and $v = 6m/s$

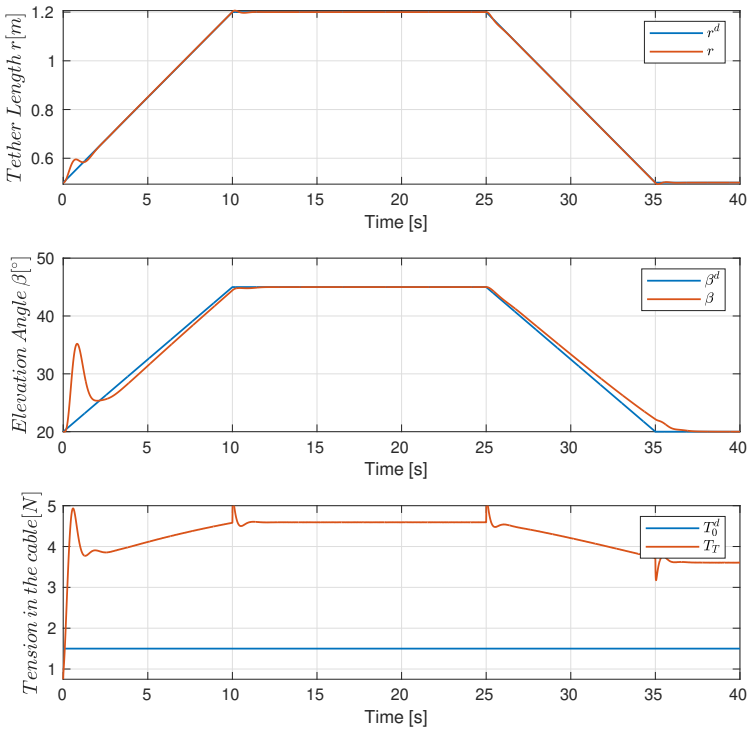

Figure 3.15 Evolution of the states r, β and T_T for a Magnus wing and $v = 6m/s$

For a Magnus wing, the spin ratio X is an additional control variable. For this simulation, the rotational speed of the cylinder was set to a fixed value $\omega_{cyl} = 319.15rad/s$. It corresponds to a spin ratio $X = 2.5$ that leads to good performances of the Magnus wing.

It appears that the system is impacted in the same way than in Subsection 3.6.2, the trajectory has a tracking error and the beginning of the take-off phase is perturbed as showed Figure 3.13 and Figure 3.15. The tether tension is also higher in this case, around $4.5N$ against $3N$ for a classical airfoil. The drone on Figure 3.14 is more inclined on this case, but the thrust is more reduced thanks to a larger lift force.

3.6.5 Conclusion on feedback linearization

The simulation results for different wing behavior and wind conditions show the performance of the proposed feedback linearization control approach on such a highly nonlinear and

uncertain system. In absence of wind, the control strategy leads to very good performances with $\alpha_D = 0$ configuration. $\alpha_D = \frac{\pi}{2}$ and Magnus wing configurations also lead to very good results in absence of wind but we choose not to show here to prevent a too dense manuscript. We observe that, as the wind speed increases, the system performance decrease, in terms of path following, and thus safety, but also in terms of energy efficiency. As lift and drag forces are considered as perturbation, and not included into the feedback linearization nor considered as additional potential actuator, the resulting force is poorly rejected by the control law.

As our goal is to design a system that is able to take-off and land safely for a wide range of wind condition, in the next section, aerodynamic forces will be included into the feedback linearization in order to preserve a linear behavior in presence of wind.

3.7 Integration of the aerodynamic forces in the control design

In order to have a more robust system against to wind disturbances, the aerodynamic forces have to be taken into account in the control design step. A first way is to include them in the output feedback linearization method. The design is same as in section 3.2. The equation 3.11 is updated and becomes

$$\ddot{y} = \underbrace{\begin{pmatrix} \frac{1}{M_M+M_D}\left[r\dot{\beta}^2 M_M - P\sin(\beta) + u_{T_0} + F_r^{aero}\right] \\ \frac{1}{r}\left[-2\dot{\beta}\dot{r} + \frac{1}{M_M}(-P\cos(\beta) + F_\tau^{aero})\right] \end{pmatrix}}_{b(x)} + \underbrace{\begin{pmatrix} -\frac{1}{M_M+M_D} & 0 \\ 0 & \frac{1}{M_M}\frac{1}{r} \end{pmatrix}}_{A(x)} \underbrace{\begin{pmatrix} u_r^d \\ u_\beta \end{pmatrix}}_{u} \quad (3.19)$$

with F_r^{aero} and F_τ^{aero} stand for the radial and tangential components of the aerodynamic forces.

3.7.1 Simulation Results

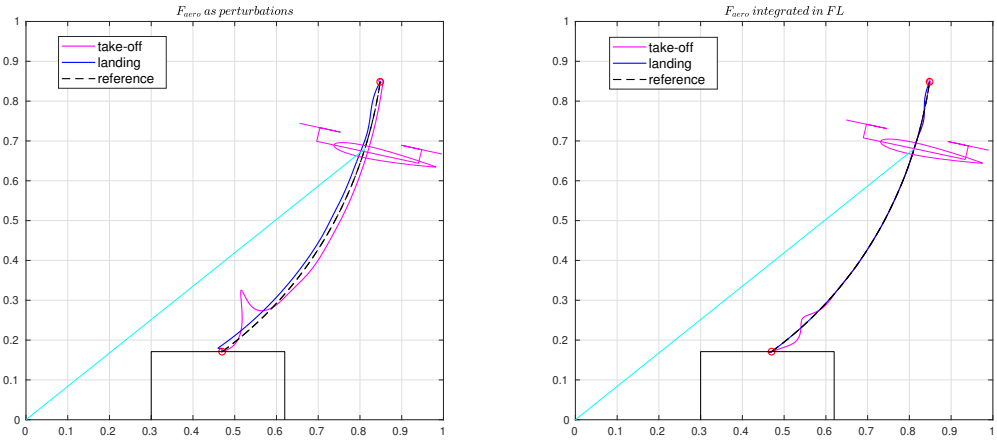

Figure 3.16 Trajectory of the system for aerodynamic forces considered as perturbation on the left and with the integration of aerodynamic forces on the right for $v = 6m/s$.

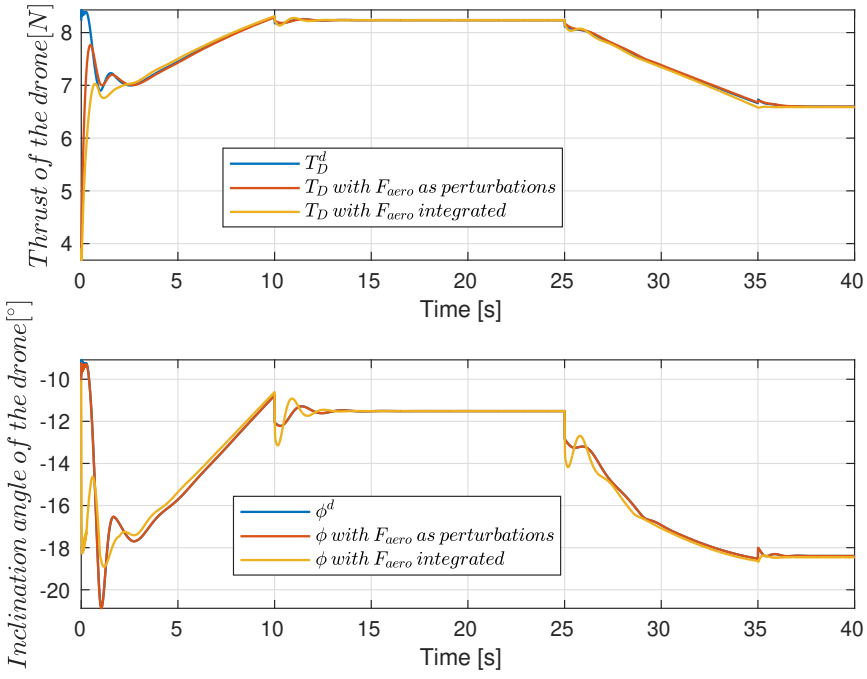

Figure 3.17 Evolution of drone inputs and comparison between aerodynamic forces considered as perturbation or integrated in the feedback linearization for $v = 6m/s$.

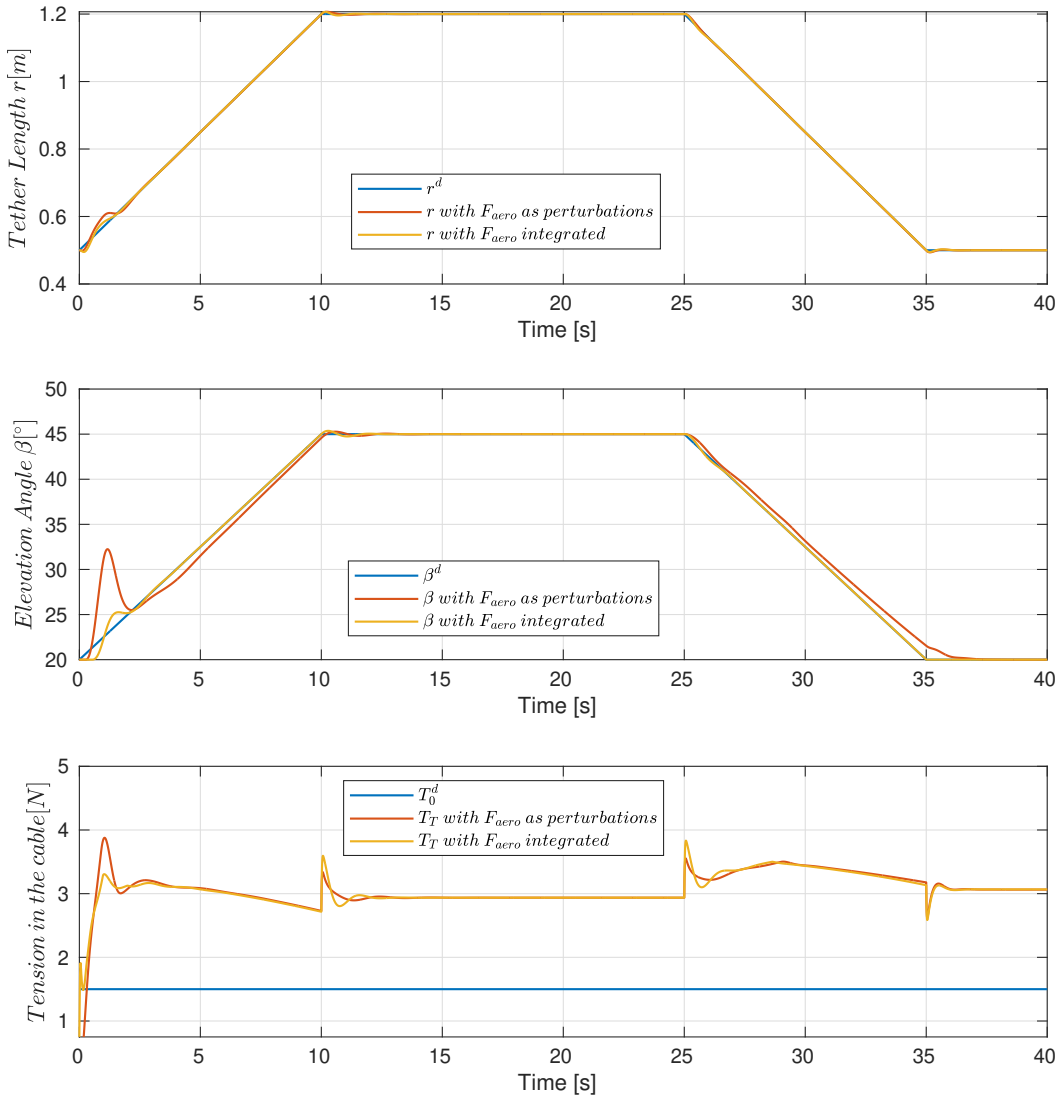

Figure 3.18 Evolution of the states r, β and T_T and comparison between aerodynamic forces considered as perturbation or integrated in the FL for $v = 6m/s$.

Thanks to the integration of aerodynamic forces in the output feedback linearization method, the take-off of the system is more robust to wind. Figures 3.16 and 3.18 show that the main improvement is at the beginning of the take-off. Figure 3.16 shows that the trajectory is closest to its reference and the tracking error has been deleted thanks to the

integration of the aerodynamic forces in the feedback linearization. This improvement can also be seen on the evolution of the state variables on Figure 3.18. The tension in the tether is above its desired value due to the open loop control on this state. Figure 3.17 shows that the drone inclination angle is less perturbed by the wind and the oscillations are lower. However it is important to notice that this integration is ideal in simulation since it assumes that the aerodynamics forces are perfectly known. In reality, those forces have to be estimated and it is hard to obtain a relevant estimation. This issue will be handled in Chapter 4. On the other hand, the additional aerodynamic force is transferred in the tether tension and lead to an additional energy consumption. Using aerodynamic forces as additional actuators are then considered in the next section in order to balance more efficiently drone thrust and aerodynamic forces.

3.8 Aerodynamic forces used as actuators

To have a more robust system against the wind disturbances, another method is to consider these forces in the control chain as additional actuators. For this, an optimization algorithm is developed in this block MIX. The idea is to take as inputs the desired radial and tangential forces coming from the controller: u_β and u_{T_0} and to distribute these forces on the aerodynamics forces and complete them if needed with the drone actuators.

$$u_{T0} = F_r^{aero} - T_D \sin(\phi - \beta) \tag{3.20}$$
$$u_\beta = F_\tau^{aero} + T_D \cos(\phi - \beta)$$

The radial and tangential components of the aerodynamic forces defined as fllows,

$$F_r^{aero} = L \sin(\beta - \alpha_w) + D \cos(\beta - \alpha_w) \tag{3.21}$$
$$F_\tau^{aero} = L \cos(\beta - \alpha_w) - D \sin(\beta - \alpha_w) \tag{3.22}$$

This algorithm allows to reduce the thrust and thus going from a lift coming from the drone to a lift due to the wing. In addition, actuators constraints has to be considered, such as maximum thrust of the drone T_{Dmax}, and its minimum and maximum angles of inclination $[\phi_{min}, \phi_{max}]$. To keep a good reactivity of drone thrust during all the take-off and landing phase, facing then potentially fast wind speed variations, one can also introduce a minimum drone thrust T_{Dmin} in the algorithm that will lead to an extra energy consumption for safety purpose.

3.8.1 Magnus wing case

As Magnus wing leads to an additional control variable through its spin ratio X that will modify aerodynamic forces L and D, the problem can be easily solved by a direct calculation. Thus, there are three control inputs for two outputs. An additional control objective has to be determined in this case. The objective is to maximize the aerodynamic forces and

complete with the drone. This will lead to the minimization of the drone thrust, and thus energy consumption of the system.

Using Equation 2.1 and Equation 2.5, find X that minimises expression $|F_\tau^{aero} - u_\beta|$, then calculate

$$\begin{aligned} T_D^d &= max(\sqrt{(u_{T_0} - F_r^{aero})^2 + (F_\tau^{aero} - u_\beta)^2}, T_{Dmin}) \\ \phi^d &= \beta - acos\left(-\frac{|F_\tau^{aero} - u_\beta|}{T_D^d}\right) \end{aligned} \tag{3.23}$$

Note that to do this, a good measurement or estimation of the apparent wind v_a is needed because the desired X is obtained with equation 2.5 through the control of rotation speed of the cylinder ω_{cyl}.

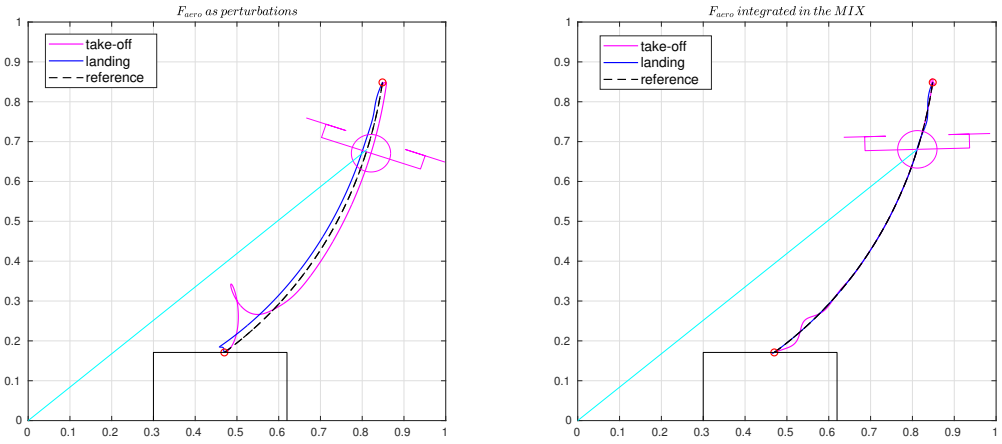

Figure 3.19 Comparison of the trajectory of the system for $v = 6m/s$ in the Magnus case

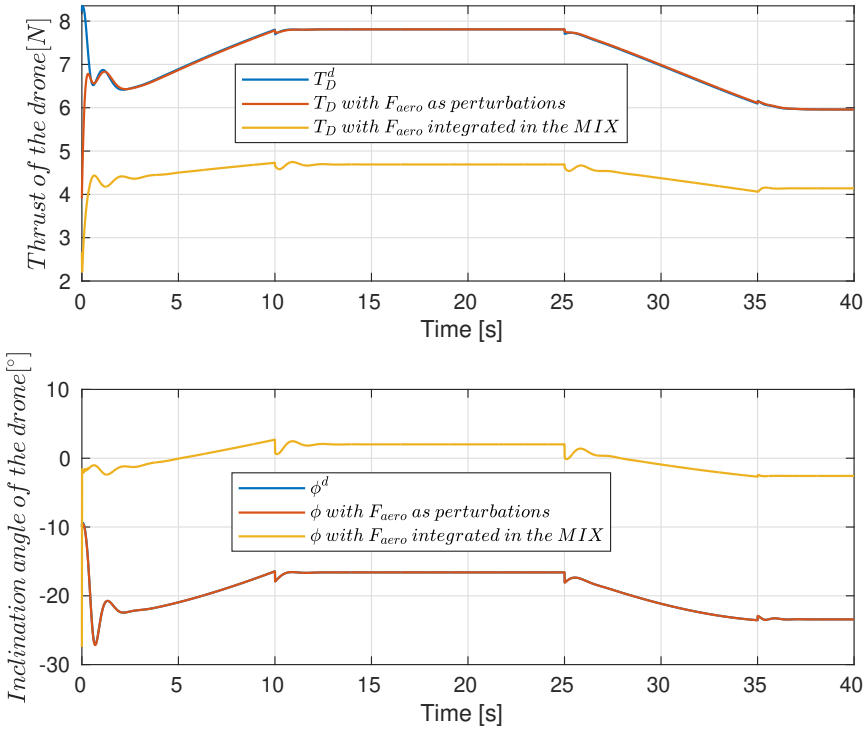

Figure 3.20 Comparison of drone inputs for $v = 6m/s$ in the Magnus case

Figures 3.19-3.21 clearly show that results are improved thanks to the MIX block which take into account the forces generated by the Magnus wing. The trajectory on Figure 3.19 is closer to the desired one and the output variables on Figure 3.21 follow better their references. The tension in the tether is much lower and equal to its reference. The influence of the MIX block can be clearly seen on the drone inputs in Figure 3.20. The thrust is lower because a part of the global forces is created by the wing. In the first case, the total radial force generated by the drone plus the aerodynamic forces is too high that is why the tether tension has to compensate with a higher tension. In the second case, the drone adapt its thrust to generate the right forces knowing the part applied by the aerodynamic forces and the tether tension stays at its desired value.

These results show that integrating the aerodynamics forces in the MIX block improves the robustness of the system against the wind and compensate well the errors on T_T due to

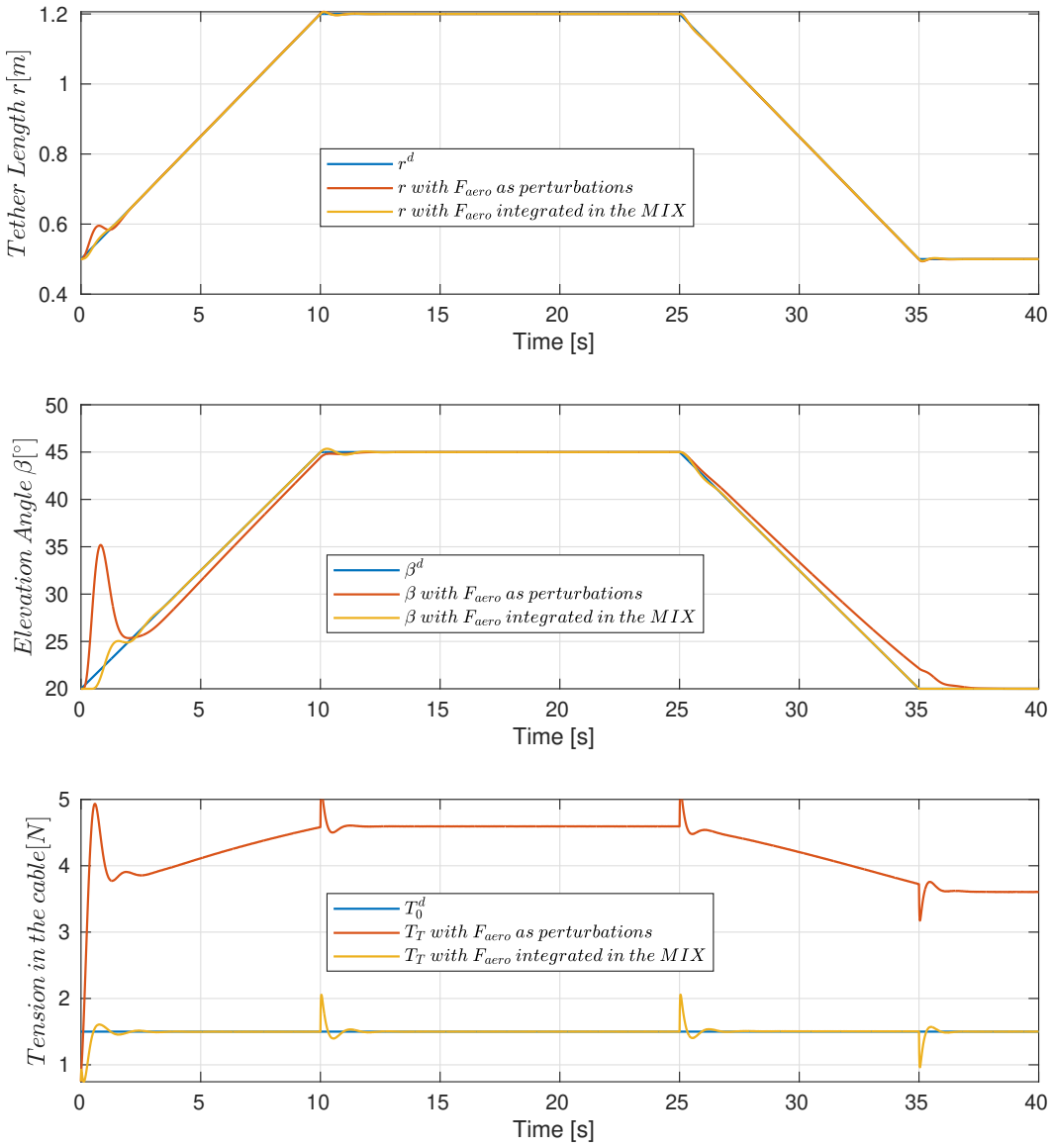

Figure 3.21 Comparison of the states r, β and T_T for $v = 6m/s$ in the Magnus case

the open-loop controller. It also reduces drone thrust and thus show the use of aerodynamic forces to reduce energy consumption during take-off and landing phases.

3.8.2 Airfoil wing case

In the case of airfoil wing, there is not an extra control variable as the wing is linked to the drone. In this case, C_L and C_D depends of the value of the inclination angle ϕ (Equation 2.4, Figure 2.2), that is why a research algorithm is used in order to find the best inputs T_D and ϕ that will produce the desired u_β and u_{T0} by the sum of T_D and the resulting aerodynamic forces. The objective is to maximise the use of the aerodynamics forces and minimize the use of the drone in order to reduce embedded energy consumption.

The optimization problem can be sum up by the following equations:

Find (T_D, ϕ) such that

$$\begin{aligned} F_\tau^{aero} + T_D \cos(\phi - \beta) &= u_\beta \\ F_r^{aero} - T_D \sin(\phi - \beta) &\geq u_{T_0} \\ T_{Dmin} \leq T_D &\leq T_{Dmax} \\ \phi_{min} \leq \phi &\leq \phi_{max} \end{aligned} \tag{3.24}$$

A comparison between a simple MIX block corresponding to Equation 3.1 and a MIX with the research algorithm is presented in the Figures 3.22 to 3.23 for a wind of $6m/s$.

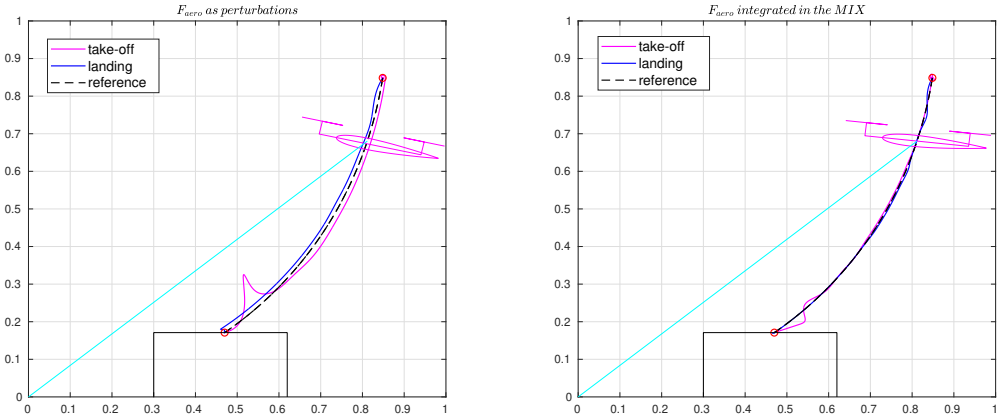

Figure 3.22 Comparison of the trajectory of the system with a MIX block for $v = 6m/s$

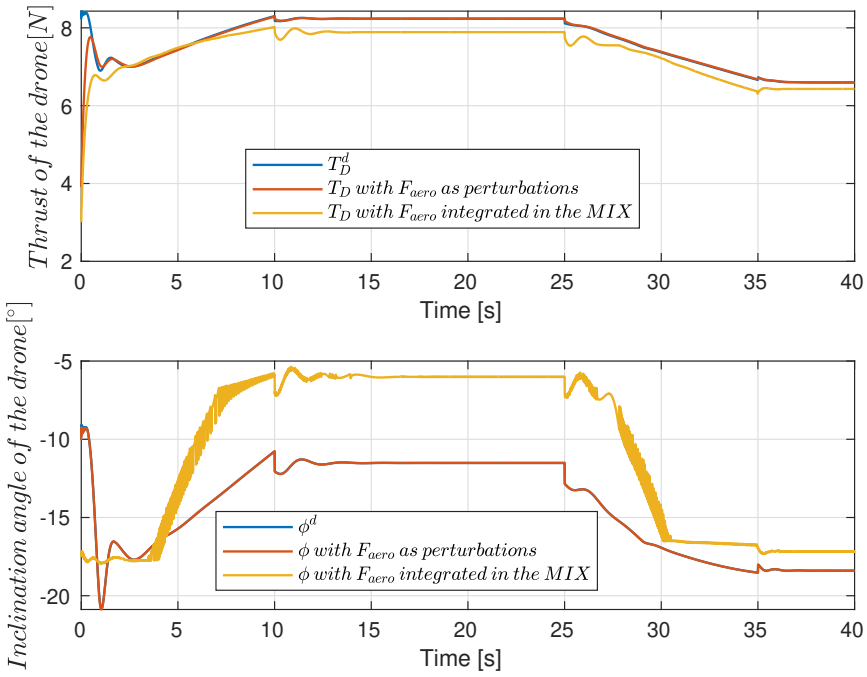

Figure 3.23 Comparison of drone inputs with a MIX block for $v = 6m/s$

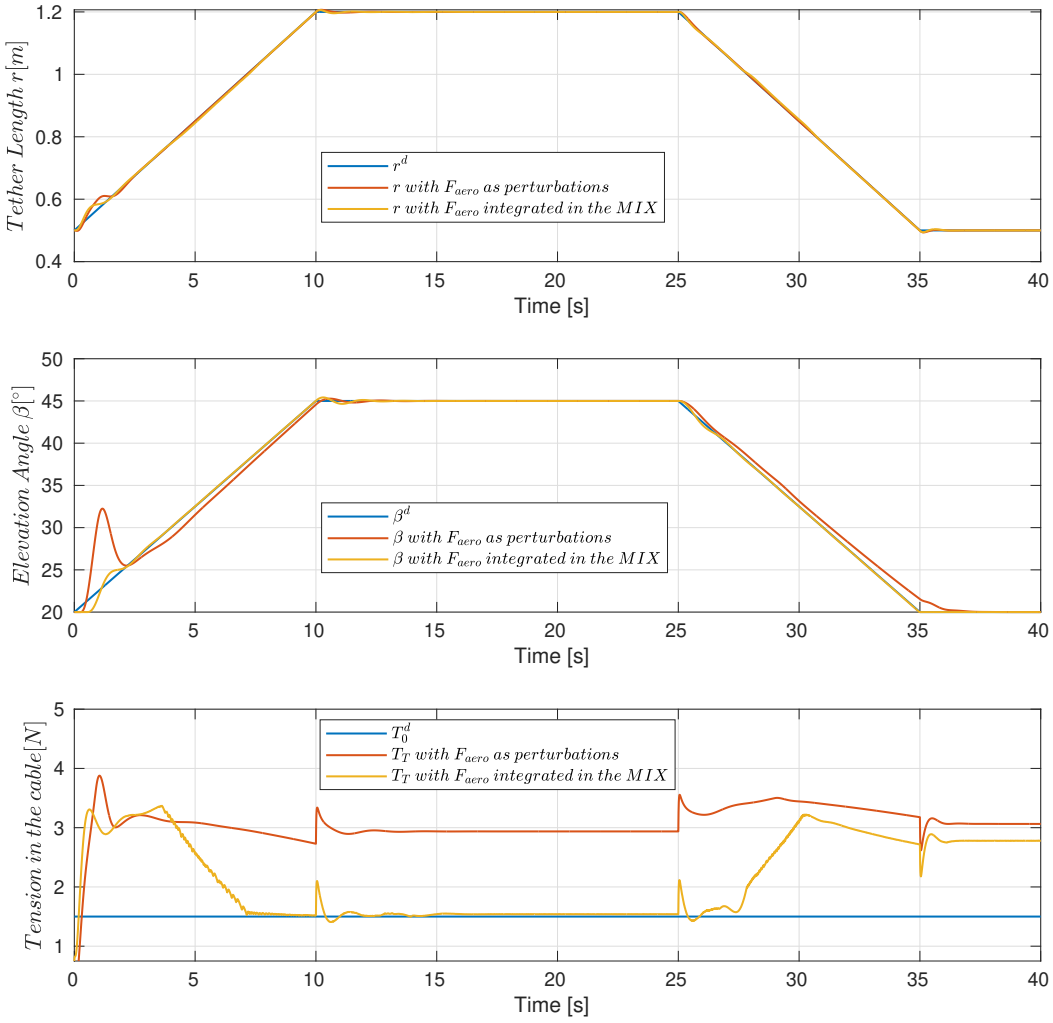

Figure 3.24 Comparison of the states r, β and T_T with a MIX block for $v = 6m/s$

The trajectory on Figure 3.22 is smoother thanks to the improved MIX block. In Figure 3.23, the thrust of the drone is lower, $7.9N$ against $8.2N$, and this induces a tether tension closest to its desired value, as shows Figure 3.24.

The MIX block with a research algorithm allows to have a more robust control scheme with respect to wind. We have observed that, with a simple MIX, for a wind higher than $3m/s$, the system performance decreases. However, using a MIX block with a research algorithm allows to fulfil the objective with a wind superior to $6m/s$.

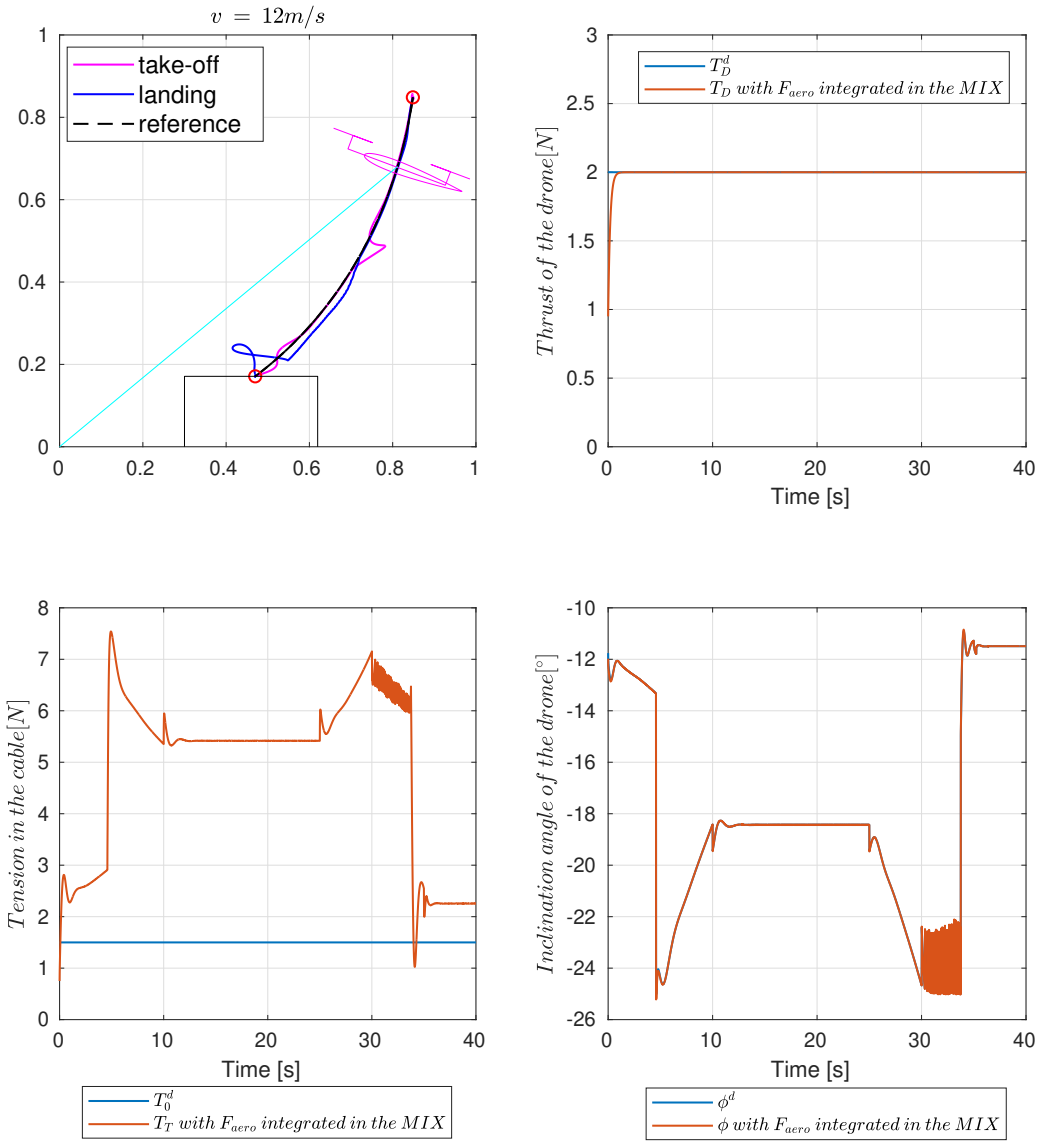

Figure 3.25 Influence of a MIX block for $v = 12m/s$

In Figure 3.25, the trajectory of the system, the tether tension and the drone inputs are presented for a wind of $12m/s$. At this wind speed, the lift is high enough to support the system, thus the drone thrust is at its minimum value $2N$. The winch actuator allows to maintain the system at its desired position. Note also that tether tension recover a bigger value than the desired one. As aerodynamic forces are function of the square of wind speed, it can become very big and in this situation, the tether is compensating the main part of

this force.

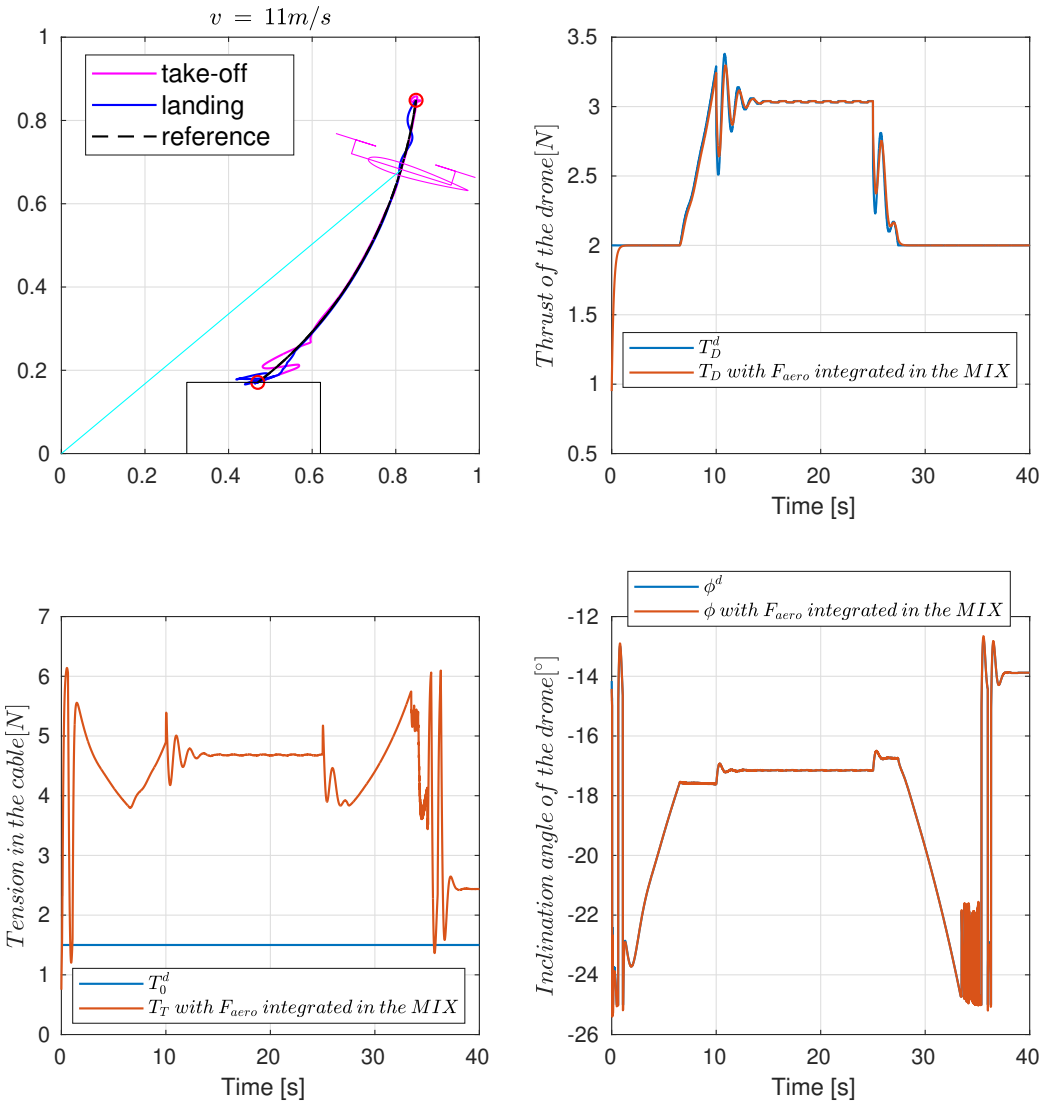

Figure 3.26 Influence of a MIX block for $v = 11m/s$

An intermediate situation is presented on Figure 3.26. At the beginning of the take-off and for the landing the thrust is at its minimum value $2N$ but for the phase where the system stays in the air, the drone is useful and has a thrust around $3N$. The algorithm is able to switch between using the wing or the drone, with a priority on the use of the wing.

It is worth pointing out that, for now, this solution is not implementable on the test

bench since the research algorithm demands an important computational time and thus an optimisation algorithm dedicated to real-time implementation has to be developed.

Note also that the model of the wing is supposed to be perfectly known. However this is not the case in real life. Thus the expected performances of the implementation of this algorithm would probably be beyond the simulation results, depending on the level of reliability of the wing model we have. In order to tackle this problem, an estimation of airfoil model parameters is presented in Chapter 4.

3.9 Conclusion

In this chapter, a control strategy for the considered AWE system has been detailed and illustrated with simulation results. Several cases have been presented. It appears that taking into account the aerodynamic forces is necessary to have a more robust system with respect to the wind. However, these aerodynamic forces are not always known and measurable. That is why an aerodynamic forces estimator has to be developed and will be presented in the next chapter. On the other hand, in order to perform a full operational scenario of an AWE system, aerodynamic forces has to be used as actuator. Indeed, control algorithm has to keep good performance and safety margin in every kind of situations:

- in the situation where there is no wind, meaning the drone is producing all the necessary lift force
- when there is a lot of wind the lift is produced only by the airfoil and all extra aerodynamic forces has to be compensated by the tether
- and all situations in between

This approach, exposed in section 3.8, shows good performance for a wide range of wind speed, but need a reliable model of the airfoil. Moreover, apart from the Magnus wing case presented in subsection 3.8.1 where there is a direct mean to control lift and drag forces

independently of the drone angle ϕ, a dedicated optimisation algorithm, that has to work in real-time, has to be designed for airfoil cases where its angle of attack is constrained by ϕ.

Finally, theses results confirms the relevance of using the on-ground winch to control the tether length where its tension is maintained by the radial force of the drone. Indeed, we can see in all considered wind conditions that tether length's regulation gives better performances than elevation angle's regulation.

Chapter Four

External forces estimation

4.1 Objective

As explained in the previous chapter, to improve the robustness of the controller, the aerodynamic forces have to be taken into account in the control design step. To have access to these aerodynamic forces, an extended Kalman filter (EKF) [36] [37] is used to estimate them.

In order to ensure the estimation of the aerodynamic forces, the state vector of the system is extended to six state variables, by adding the unknown parameters as new state variables with zero dynamics.

Notice that, in practice, the wind velocity is an unknown variable or imprecisely measured. Thus, the radial and tangential forces defined by the following equation are unknown or poorly known.

$$\begin{cases} F_{aero,r} = L\sin(\beta - \alpha_\omega) + D\cos(\beta - \alpha_\omega) \\ F_{aero,\tau} = L\cos(\beta - \alpha_\omega) - D\sin(\beta - \alpha_\omega) \end{cases} \tag{4.1}$$

This renders model (2.15) uncertain. Moreover, the AWE system is affected by others unknown forces that can be added to the tangential and radial aerodynamic forces. For instance, one can consider the dry friction and the forces due to propeller performance

variation. That is, the radial and tangential forces that acting on the system are defined as follows:

$$\begin{cases} F_{a,r} = F_{aero,r} + F_{fric,r} + F_{prop,r}, \\ \\ F_{a,\tau} = F_{aero,\tau} + F_{prop,\tau} \end{cases} \tag{4.2}$$

$F_{fric,r} = \Gamma_S$ represents the dry friction of the on-ground winch while F_{prop} stand for the forces due to embedded battery voltage variation as well as influence of airflow on propellers efficiency. This increases highly the uncertainty in model (2.15).

The dynamic model governing the evolution of this extended state is similar to the model described in (2.15) with a constant evolution for the forces $F_{a,r}$ and $F_{a,\tau}$.

Thus, to achieve the above mentioned objectives, based on the available output data (the length of the tether and the elevation angle), an extended Kalman filter will be designed to estimate the whole state vector (3.8) of the system and the additional unknown forces (4.2).

First, an augmented state vector is considered,

$$z = [z_1,\ z_2,\ z_3,\ z_4,\ z_5,\ z_6]^T = [r,\ \dot{r},\ \beta,\ \dot{\beta},\ F_{a,r},\ F_{a,\tau}]^T \tag{4.3}$$

and then, an augmented model that includes the dynamics of the unknown forces is introduced:

$$\dot{z} = \begin{pmatrix} z_2 \\ \frac{1}{M_M+M_D}[z_1 z_4^2 M_M - u_r - P\sin(z_3) - T_d sin(-z_3+\phi) + z_5] \\ z_4 \\ \frac{1}{z_1}[-2z_4 z_2 + \frac{1}{M_m}(-P\cos(z_3) + T_d cos(-z_3+\phi) + z_6] \\ 0 \\ 0 \end{pmatrix} \tag{4.4}$$

The entries of the observation vector are the length of the tether $r = z_1$ and the elevation angle $\beta = z_3$

$$y = \begin{pmatrix} z_1 \\ \\ z_3 \end{pmatrix} \tag{4.5}$$

To sum up the objective of the proposed extended Kalman filter is to estimate both state vector of (2.15) and unknown forces (4.2). Moreover, if a measurement or estimation of wind speed is available, this allows one to get also estimation of the aerodynamic coefficients C_L and C_D.

On the opposite, it is worth pointing out that, based on Equation (2.1) the knowledge of the aerodynamic forces (drag D and lift L) and a good estimation of aerodynamic coefficients (C_L and C_D), one can get an estimation of the apparent wind velocity v_a.

For the sake of simplicity, recall that the state space representation of the system has the following form:

$$\begin{cases} \dot{z} &= f(z,u) \\ y &= Hz \end{cases} \tag{4.6}$$

with

$$H = \begin{bmatrix} 1 & 0 & 0 & 0 & 0 & 0 \\ 0 & 0 & 1 & 0 & 0 & 0 \end{bmatrix} \tag{4.7}$$

Note that, f is a nonlinear function that represents the vector filed defined in Equation (4.4). Since this function is nonlinear, it is necessary to linearize it around the current state vector and discretize it before applying the extended Kalman filter.

4.2 Linearization

A real-time linear Taylor approximation of order 1 is used to linearize the nonlinear dynamics (4.6). That is, the linearization of (4.6) around its current state vector z_k leads to

$$\dot{z} = f(z_k, u_k) + A_k(z - z_k) + B_k(u - u_k) \tag{4.8}$$

where

$$A_k = \frac{\partial f(z,u)}{\partial z}\Big|_{(z_k,u_k)} \text{ and } B_k = \frac{\partial f(z,u)}{\partial u}\Big|_{(z_k,u_k)} \tag{4.9}$$

4.3 Discretization

To obtain the classical Kalman equations, we apply the Euler explicit discretization method to (4.8).

The Euler explicit method is applied:

$$\dot{z} = \frac{z_{k+1} - z_k}{h} \tag{4.10}$$

where h stands for the considered discretization step. Thus, the following LTV discrete-time system is obtained

$$\begin{aligned} z_{k+1} &= F_k z_k + s_k \\ y_k &= H z_k \end{aligned} \tag{4.11}$$

where $F_k = I_6 + hA_k$, $s_k = h\big(f(z_k, u_k) - A_k z_k\big)$ and I_6 is an identity matrix of dimension 6.

4.4 Extended Kalman filter

Note that, the prediction phase of the considered extended Kalman filter is based on a nonlinear function. The following algorithm lists the different steps carried out by of the proposed EKF.

- **Propagation stage**
  - Predicted state estimate:

$$\hat{z}_{k|k-1} = \hat{z}_{k-1|k-1} + hf(\hat{z}_{k-1|k-1}, u_{k-1})$$

  - Predicted error covariance:

$$P_{k|k-1} = F_k P_{k-1|k-1} F_k^T + Q$$

- **Correction stage**
  - Innovation:

$$\tilde{y}_k = y_k - H\hat{z}_{k|k-1}$$

  - Residual covariance:

$$S_k = H P_{k|k-1} H^T + R$$

  - Kalman gain:

$$K_k = P_{k|k-1} H^T S_k^{-1}$$

– Updated state estimate:

$$\hat{z}_{k|k} = \hat{z}_{k|k-1} + K_k \tilde{y}_k$$

– Updated error covariance:

$$P_{k|k} = (I_6 - K_k H) P_{k|k-1}$$

Although the covariance matrices Q and R are supposed to reflect the statistics of the measurement noises and state disturbances, in this work these matrices are used as tuning parameters that can be adjusted to get desired performance (precision and convergence rate).

4.5 Simulation results: Estimating both state vector and aerodynamic forces

The EKF is implemented on Matlab [38] to be used in the 2D simulation. The measure r and β are the inputs of the EKF. With the same take-off and landing scenario introduced in the previous chapter, the estimation is done in parallel of the simulation and the estimated states are not used in the control design. Notice that, in this simulation case study the dry friction and the force due to actuator modeling errors are considered only for small wind speed, where they are not negligible in front of aerodynamic forces. Moreover, in this simulation framework, the assumed unknown forces (lift and drag forces) are generated from the formulas (2.12),(2.1) and Figure 2.2.

4.5.1 Discussion on the tuning matrices

It is well known that the performance of an EKF depends mainly on the weighting matrices R and Q. In this study, the used sensors are accurate then the eigenvalues of R should be sufficiently lower than those of Q. On the other side, thanks to the measurements, the length of the tether r and the elevation angle β can be considered accurate in the augmented model

(4.4). Therefore, these state variables should be less weighted compared to the other state variables. Furthermore, since the dynamics of the additive forces are really unknown, the eigenvalues of the matrix Q that correspond to these state variables should be bigger than the others.

To illustrate the tuning method, let us consider two tuning examples. In the first one, all the state variables and measurements are identically weighted. That is, the weighting matrices are given by,

$$Q_1 = \begin{bmatrix} 1 & 0 & 0 & 0 & 0 & 0 \\ 0 & 1 & 0 & 0 & 0 & 0 \\ 0 & 0 & 1 & 0 & 0 & 0 \\ 0 & 0 & 0 & 1 & 0 & 0 \\ 0 & 0 & 0 & 0 & 1 & 0 \\ 0 & 0 & 0 & 0 & 0 & 1 \end{bmatrix}, \; R_1 = \begin{bmatrix} 1 & 0 \\ 0 & 1 \end{bmatrix} \tag{4.12}$$

For the second example, the choice of these matrices is based on the above introduced tuning method. That is,

$$Q_2 = \begin{bmatrix} 1^{-10} & 0 & 0 & 0 & 0 & 0 \\ 0 & 5 & 0 & 0 & 0 & 0 \\ 0 & 0 & 1^{-10} & 0 & 0 & 0 \\ 0 & 0 & 0 & 5 & 0 & 0 \\ 0 & 0 & 0 & 0 & 20 & 0 \\ 0 & 0 & 0 & 0 & 0 & 20 \end{bmatrix}, \; R_2 = \begin{bmatrix} 1^{-10} & 0 \\ 0 & 1^{-10} \end{bmatrix} \tag{4.13}$$

The simulation results with the first tuning case (Q_1 and R_1) are plotted in Figure 4.1. while those of the second tuning case (Q_2 and R_2) are illustrated in Figure 4.2.

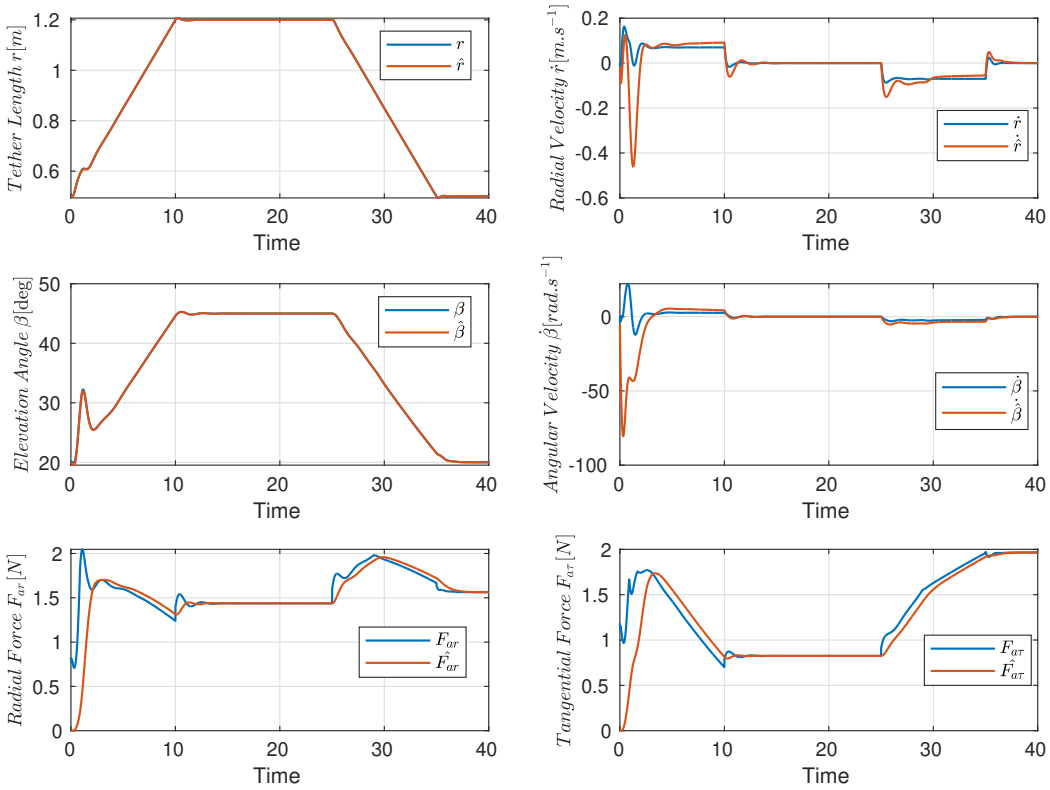

Figure 4.1 The estimated state variables with Q_1 and R_1 and wind velocity $v = 6m/s$. Blue lines show the actual state variable while the red lines correspond to the estimated ones.

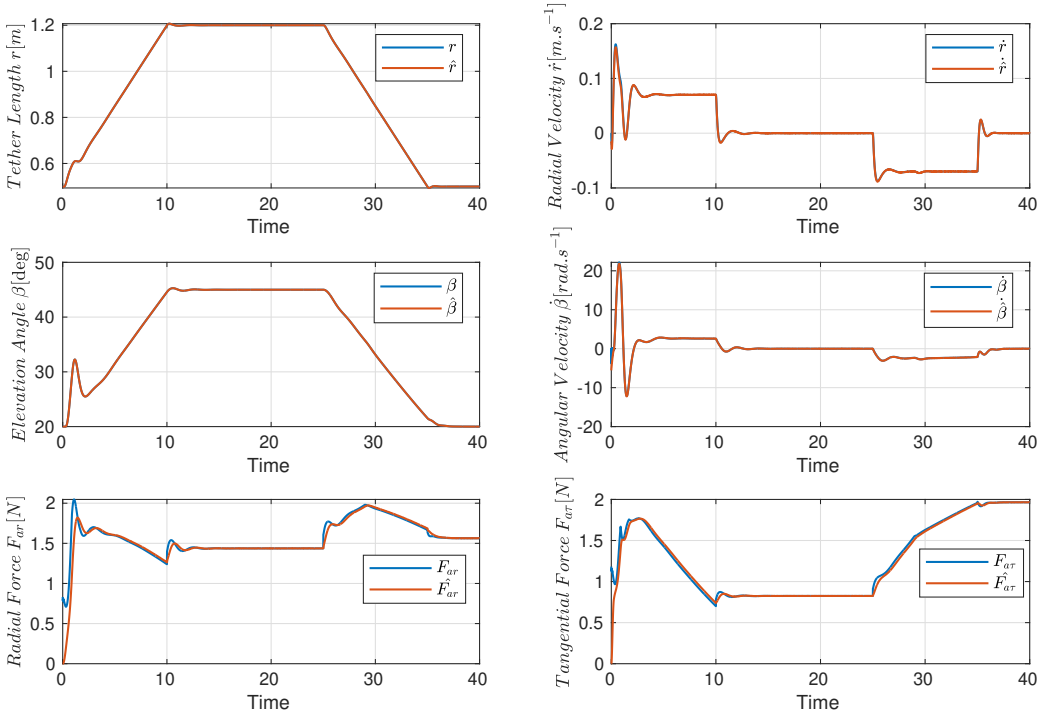

Figure 4.2 The estimated state variables with Q_2 and R_2 and wind velocity $v = 6m/s$. Blue lines show the actual state variable while the red lines correspond to the estimated ones.

The estimation errors for both tuning cases are presented in Figure 4.3.

As shown in Figures 4.1, 4.2 and 4.3, the weighting matrices Q_2 and R_2 provide better results in terms of convergence rate and precision than those generated by the weighting matrices Q_1 and R_1. The obtained simulation results permit to validate the proposed EKF and the employed tuning method for the weighting matrices.

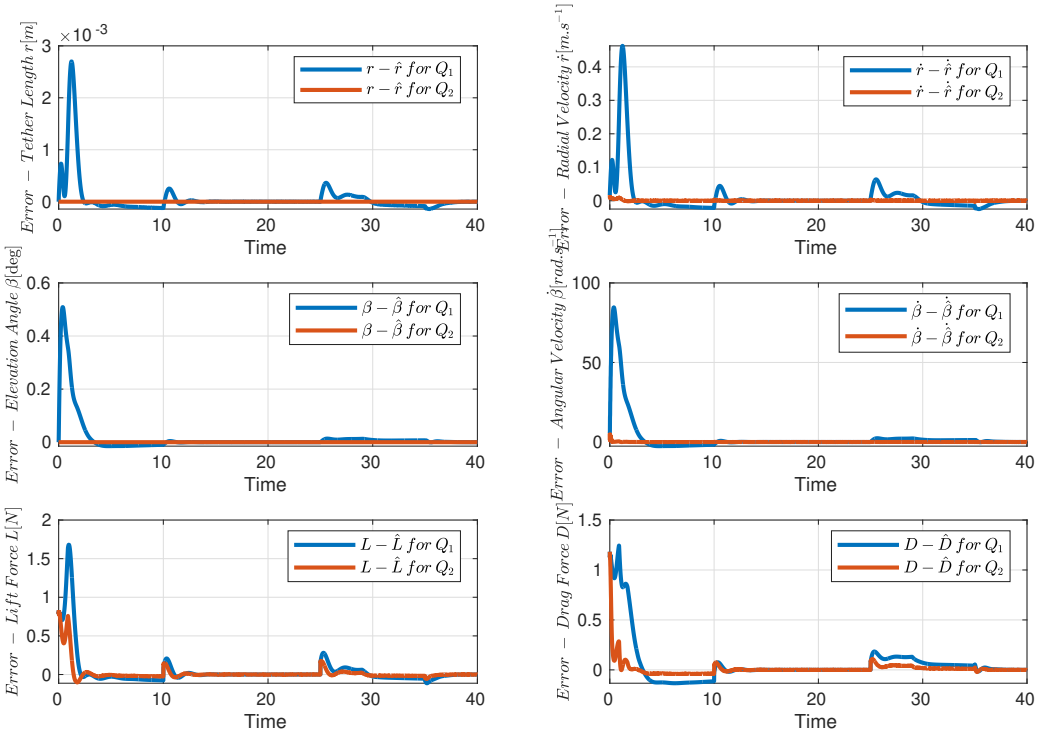

Figure 4.3 Comparison of the errors of estimation. Blue lines show the errors with Q_1 and R_1 while the red lines correspond to Q_2 and R_2.

4.5.2 Estimating F_{a_r} and F_{a_τ} for $v = 0m/s$

It is worth pointing out that in the case where there is no wind, $v = 0m/s$, the aerodynamic forces are close to $0N$ and the estimated radial and tangential forces correspond to the other forces which are not taken into account in the controller design stage: For instance the dry friction, the forces due to actuators modeling errors etc. Figure 4.4 shows the simulation results obtained in the case of no wind. Note that, the take-off and landing scenario is similar as above.

As illustrated in Figure 4.4, the estimated radial force $\hat{F}_{a_r}$ plotted in blue is composed by the dry friction displayed in red and an additive force due to actuator modeling errors represented in yellow. As observed, the dry friction is well related to the sign of the reel-in and reel-out speed $\dot{r}$. On the other hand, the estimated tangential force $\hat{F}_{a_\tau}$ depicted in blue

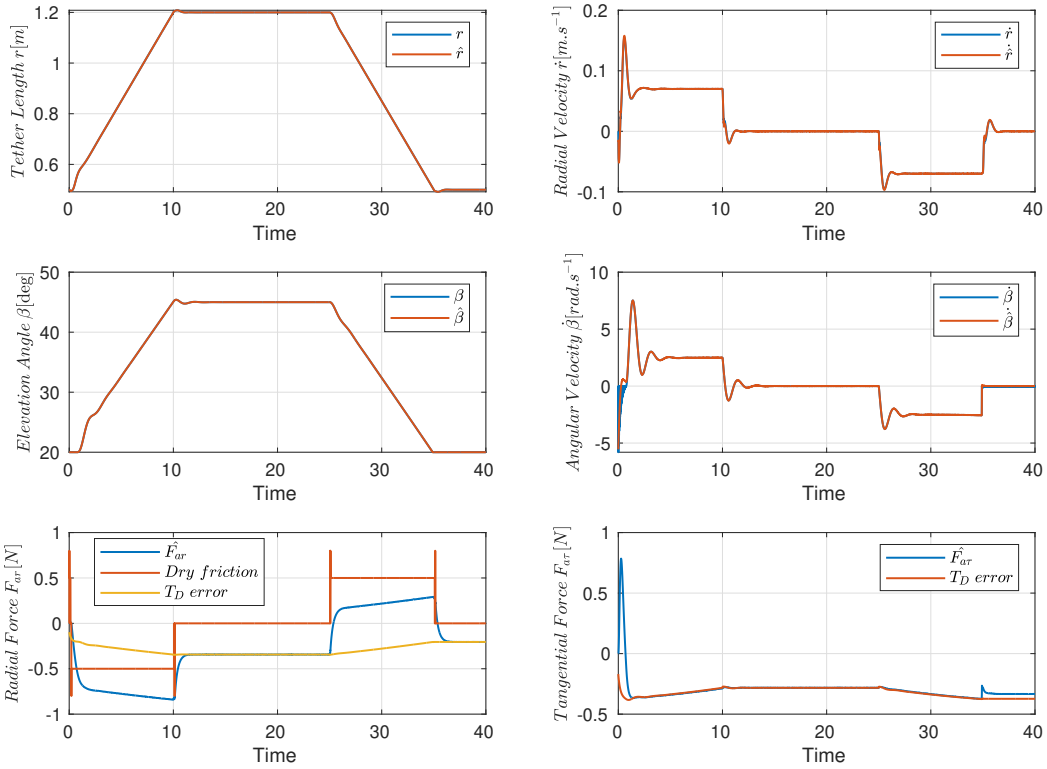

Figure 4.4 The estimated state variables compared to those generated by the model, with assumed wind velocity $v = 0m/s$.

is mainly formed by the force induced by the actuator modeling errors, illustrated in red.

4.5.3 Estimating F_{a_r} and F_{a_τ} for $v = 7m/s$

In this simulation test, to simplify the study, the dry friction and the force due to actuator modeling errors are not considered since they are negligible in front of the aerodynamic forces.

The estimated state variables are presented in Figure 4.5 together with the assumed actual variables generated by the considered model.

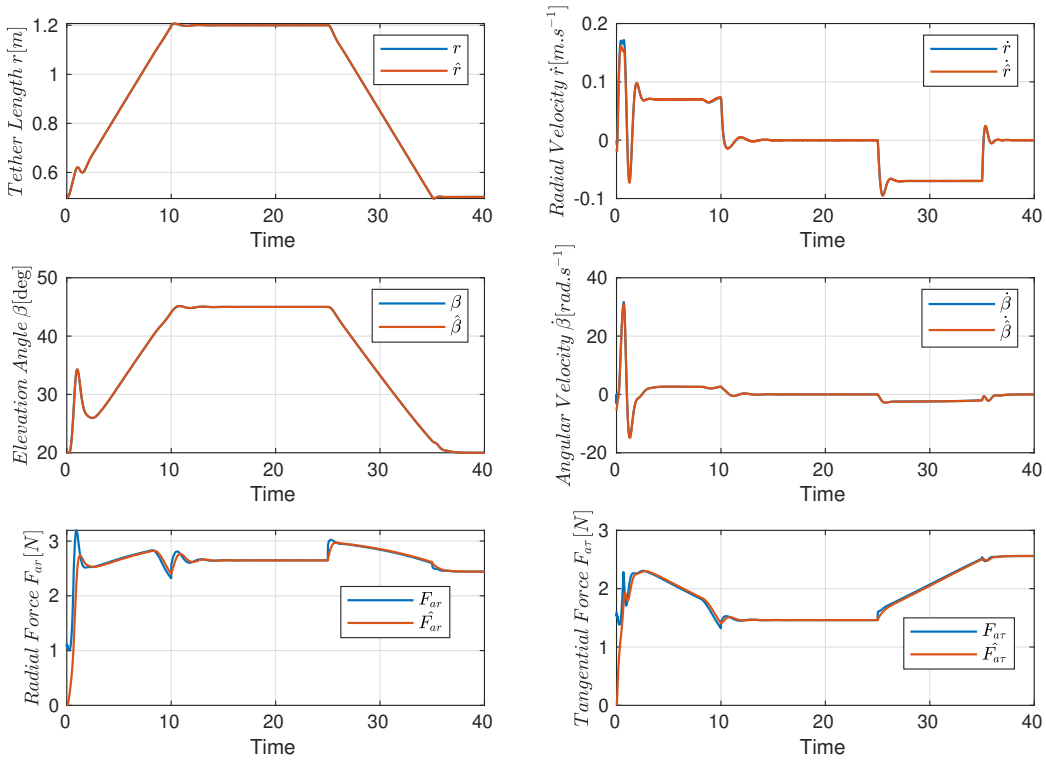

Figure 4.5 The estimated state variables compared to those generated by the model, with assumed wind velocity $v = 7m/s$.

Moreover, to show clearly the performance (convergence rate and accuracy) of the EKF the time evolution of the estimation errors are plotted in Figure 4.6.

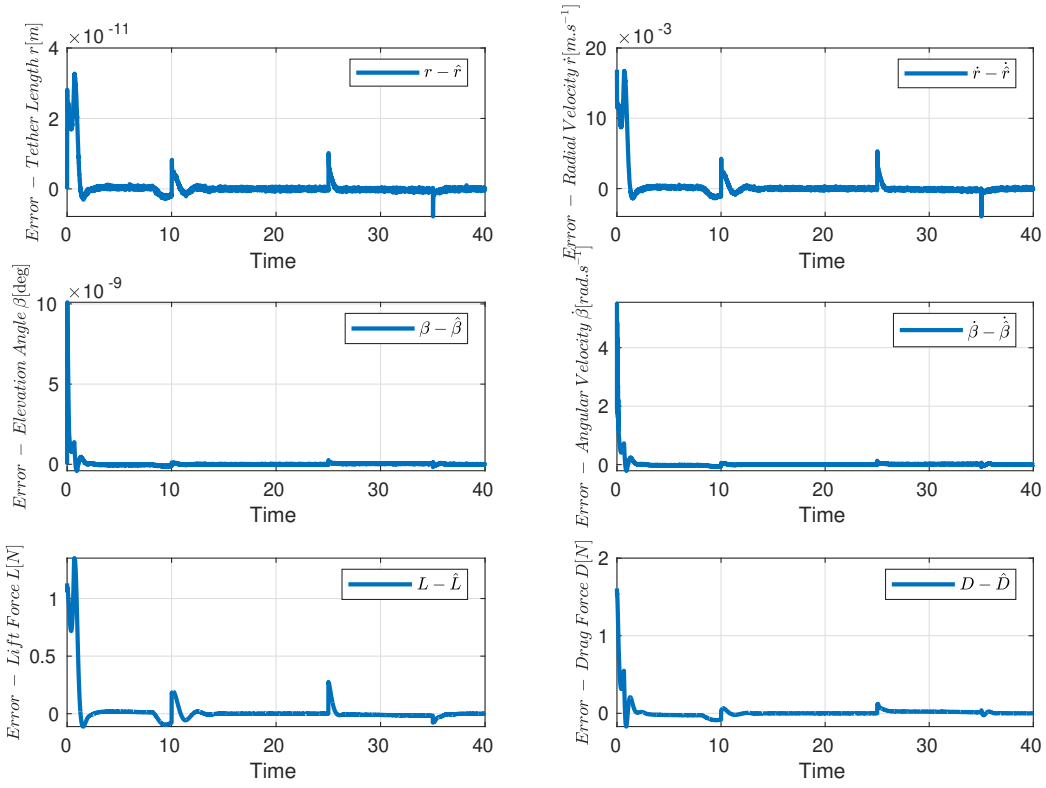

Figure 4.6 The error of estimation for the state variables, with assumed wind velocity $v = 7m/s$.

This figure shows that the initial estimation errors converge rapidly towards weak steady state values. Same remarks and conclusions can be done on the estimated aerodynamic forces plotted in Figure 4.7.

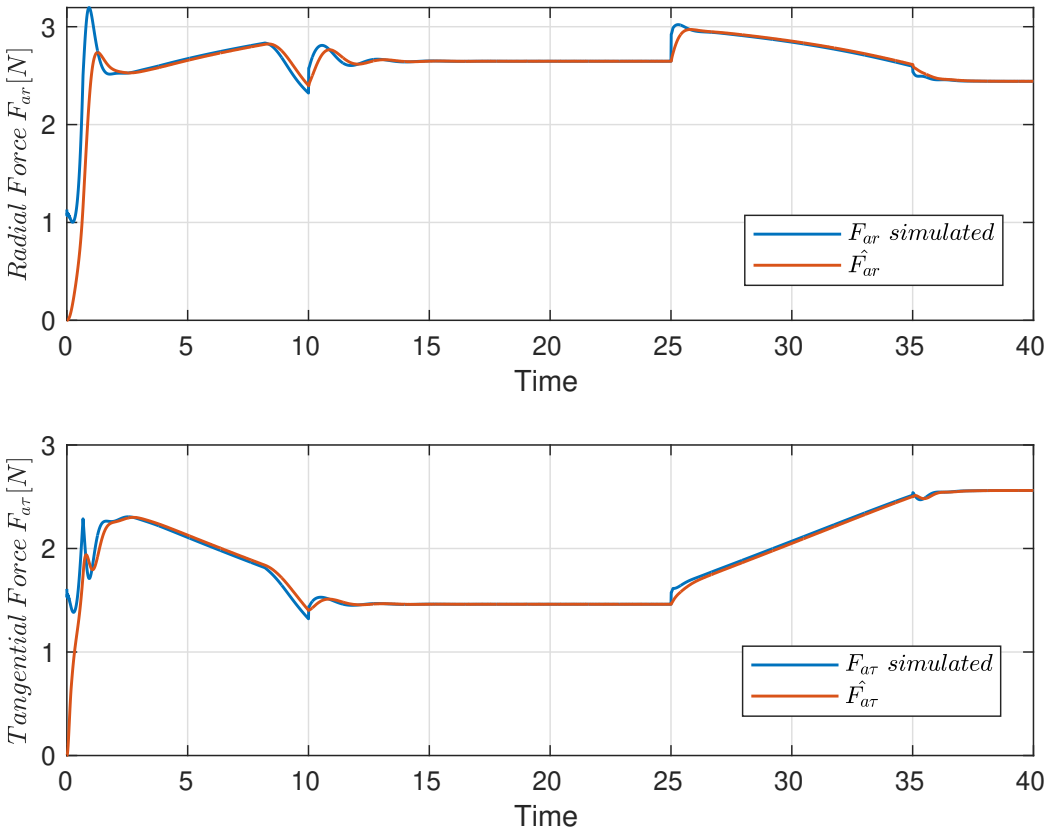

Figure 4.7 The estimated aerodynamic forces compared to the assumed actual ones, for $v = 7m/s$.

4.5.4 Estimating the aerodynamic coefficients C_L and C_D

The estimated aerodynamics forces allow one also to deduce a model for the aerodynamic coefficients C_L and C_D by applying relationships (2.1) and (4.1). Figure 4.8 presents the evolution of the estimated coefficients C_L and C_D provided from the data filter and those given by the model in Figure 2.2.

As shown in Figure 4.8, the estimated values of C_L and C_D converge rapidly towards that provided by the model. During the scenario, the angle of attack changes and allows us to estimate the model of C_L and C_D. By estimating these parameters for the whole range of possible angle of attack, a good aerodynamic model of the system can be identified and then used as actuator like presented in Section 3.8. However, to be able to do these estimations,

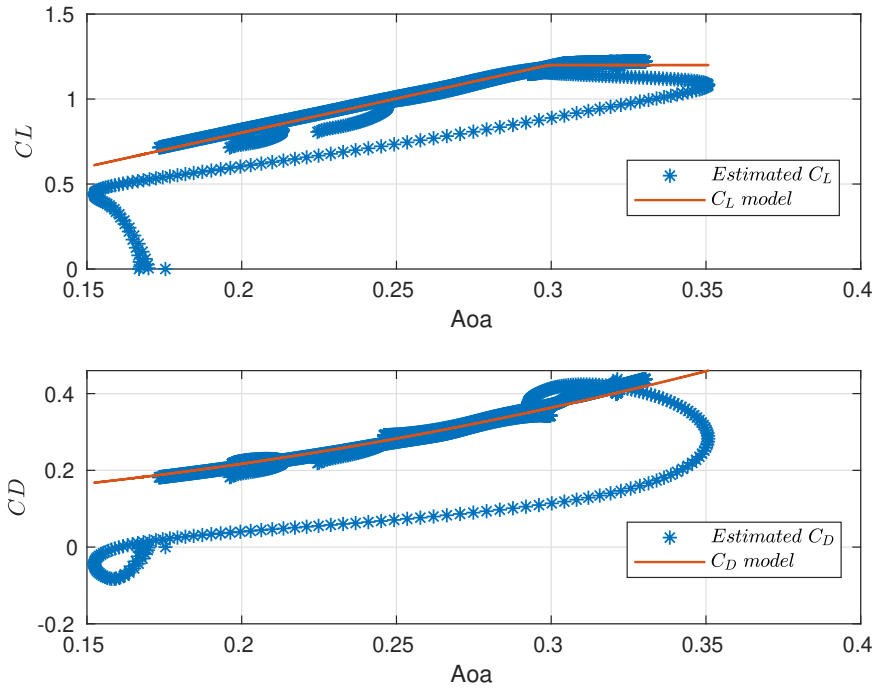

Figure 4.8 Estimated versus reference of the aerodynamic coefficients C_L and C_D for $v = 6m/s$.

a measure of the wind speed is required.

It is worth pointing out that, thanks to the proposed EKF, the wind velocity can be estimated if an accurate model of the aerodynamic coefficients is available.

4.5.5 Integrating the aerodynamic forces in the control law

In this subsection, we propose to integrate the estimated aerodynamic forces in the design of the output-feedback linearization control law presented in section 3.7. This allows one to better deal with the system uncertainties and so to enhance its robustness. The obtained simulation results for the controlled system are shown in Figures 4.9 and 4.10.

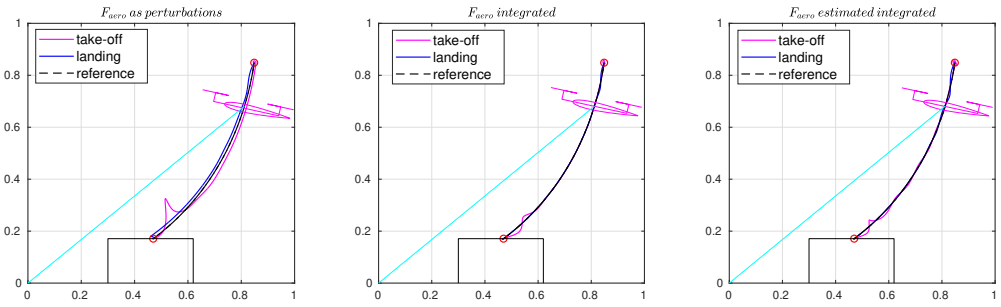

Figure 4.9 Flight trajectories of the AWE system driven by different control strategies for $v = 6m/s$

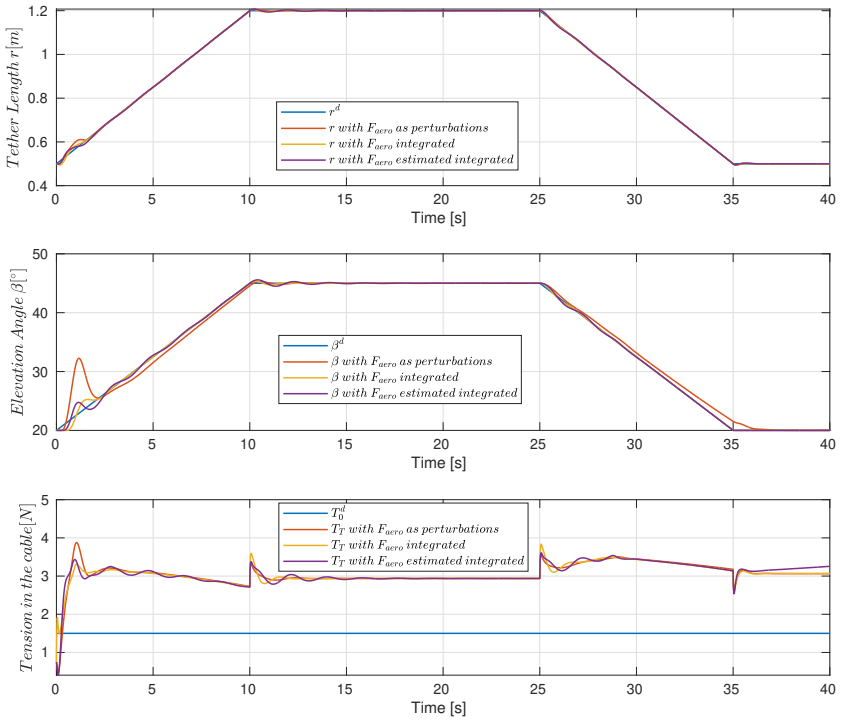

Figure 4.10 The time evolution of r, β and T_T for $v = 6m/s$

Three control configurations are considered in these figures. The red lines correspond to the control law presented in Subsection 3.6.2 where the aerodynamic forces are considered as disturbances. The yellow lines show the results of the ideal case presented in subsection 3.7 where the aerodynamic forces are assumed perfectly known and integrated directly in the control step. Finally, the purple lines corresponds to the case where the estimated aerodynamic forces are used in the design step of the controller. As expected, the knowledge of these forces allows one to obtain better results in terms of the tracking performance. As illustrated in Figure 4.9, thanks to the use of the EKF the static deviation of the AWE system from its set-point trajectory is reduced considerably. Figure 4.10 shows the time evolution of the three control input: two state variables (the tether length r and the elevation angle β) and the tension in the tether T_T for the three considered control configurations. It is clear that the main improvement is about the elevation angle, which has less steady-state error and a smaller overshoot at the beginning of the take-off phase.

4.6 Conclusion

To sum up, the different simulation results show that by considering the aerodynamic forces in the control design step, the performance of the closed loop system is improved. Moreover, the proposed EKF succeeds to provide accurate estimations of the state vector of the system and the unknown forces that act on it. Moreover, by using it in a wide range of known wind conditions, it can provide a valuable aerodynamic model of the system which is use-full to evaluate and optimize performances of such AWE system.

Chapter Five

Experimentation

This chapter deals with the experimental work of this thesis. A test bench was developed to validate experimentally the controller designed and the estimator. Section 5.1 details how the controller was extended to be implemented experimentally. In section 5.2 the scenario for the experimentation is presented. The test bench is detailed in section 5.3. The results of the experimentation are shown in section 5.4 for different experimental conditions.

5.1 Extension to 3D

As mentioned in the previous sections, the model and the designed control law are in the plane (2D) and only two inputs of the drone are considered: T_D and ϕ. However, in the space (3D), azimuth angle of the system η, as well as roll angle θ and yaw angle ψ of the drone has to be controlled (see Figure 5.1). An additional control law for η and ψ angles has been designed. In order to stay as much as possible equivalent to the 2D problem, the yaw is chosen such that the drone is always pointing to the ground station. Notice that, the drone has its internal control loop that regulates the yaw angle to its desired value $\psi_d = \pi + \eta$. To regulate azimuth angle η, the roll angle θ that is also locally controlled by the drone is used. This angle η is set in a way to have the system aligned with the wind, or in particular in our indoor situation aligned with x axis. The same approach employed for elevation angle

β control law detailed in section 3.2 is used:

$$\ddot{\eta} = \frac{1}{r}(-2\dot{\eta}\dot{r} + \frac{1}{M_M}u_\eta) \tag{5.1}$$

$$u_\eta = M_M r(v_\eta + \frac{2\dot{\eta}\dot{r}}{r}) \tag{5.2}$$

$$v_\eta = \alpha_{\eta_{-1}} \int_0^t e_\eta(\tau)\,\mathrm{d}\tau + \alpha_{\eta 0}\ e_\eta + \alpha_{\eta 1}\ \dot{e_\eta} + \ddot{\eta}_r^d \tag{5.3}$$

$$e_\eta = \eta_{ref} - \eta \tag{5.4}$$

In Equation 5.2 the input command u_η is obtain thanks to a feedback linearization method on the dynamical model of η given in Equation 5.1. Then a linear command v_η is design in the same way than v_β and the coefficient are chosen thanks to the ITAE criteria.

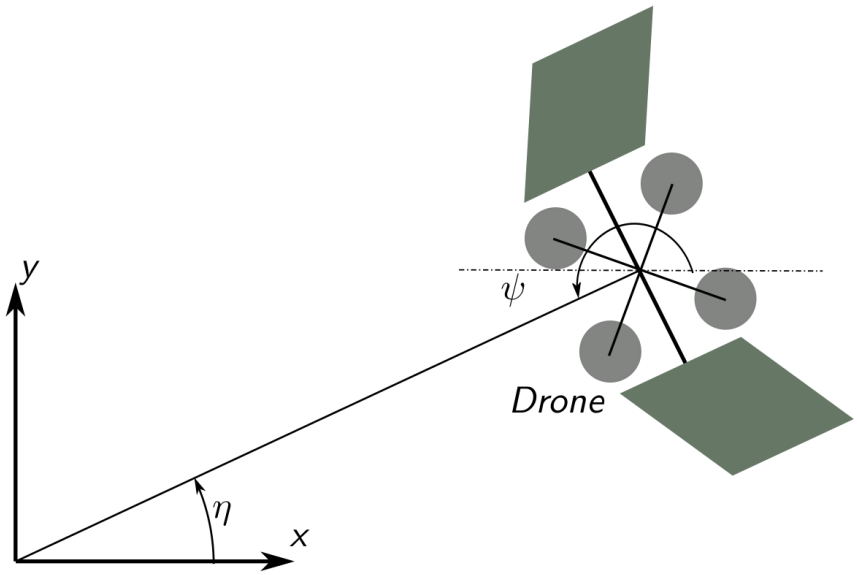

Figure 5.1 Top view of the system.

5.2 Scenario

To validate experimentally the performance of the proposed control strategy, it is tested on a scenario including a take-off and a landing. During all the scenario the desired tension in the tether T_0^d is set to $1.5N$ and the desired azimuth angle η_{ref} is equal to $0°$. The scenario is the following:

- Initial position: The system starts from its initial position at $r_0 = 0.4m$, $\beta_0 = 40°$, $T_{D_0} = 0N$ and $\phi_0 = 0$.
- Take-off phase: At $t = 0$ s the reference signal r_d goes from r_0 to $r_f = 1.2m$ with a ramp rate of $0.08m/s$, and the desired elevation angle β_d goes from β_0 to $\beta_f = 45°$ with a ramp rate of $0.5\ °/s$.
- Landing phase: At $t = 25$ s the reference signal r_d goes from r_f to r_0 with a ramp rate of $0.08m/s$, and the desired elevation angle β_d goes from β_f to β_0 with a ramp rate of $0.5\ °/s$.
- End of the scenario : Once the system is landed, the drone is back to its initial position and ready to start a new cycle.

Table 5.1 Parameters of the controller

Symbol	Name	Value
ω_{nr}	Natural frequency for the r loop	5 rad/s
$\omega_{n\beta}$	Natural frequency for β loop	3 rad/s
$\omega_{n\eta}$	Natural frequency for η loop	3 rad/s

The scenario is done firstly with no wind disturbance and a secondly with two different wind conditions. The value of the design parameters of the controller are given in Table 5.1, the value of w_{n_r} is higher than w_{n_β} and w_{n_η} since it is assumed that the control loop in r is faster than in β and η.

5.3 Experimental benchmark

The experimental benchmark is composed of wings attached to a drone and linked together to an on-ground winch with a tether. A motion capture system tracks the drone position and sends it to an on-ground computer that controls the winch and the drone. Figure 5.2 shows the global architecture of the system.

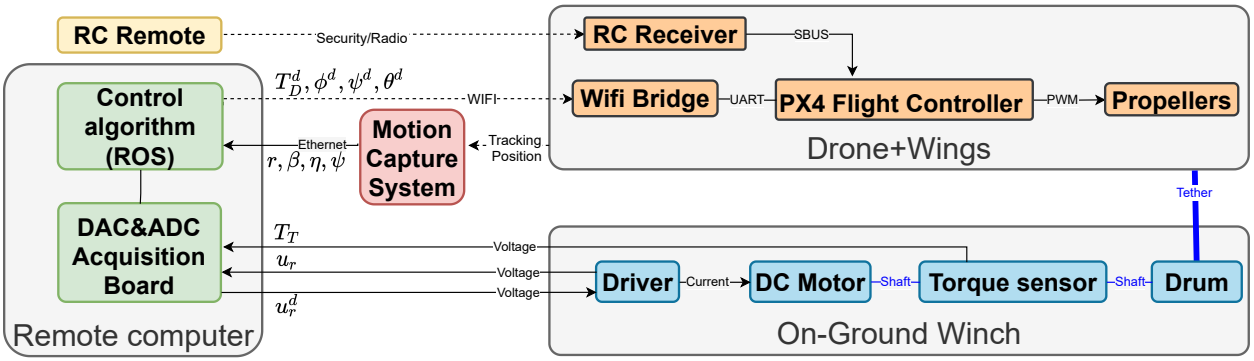

Figure 5.2 Global architecture of the benchmark.

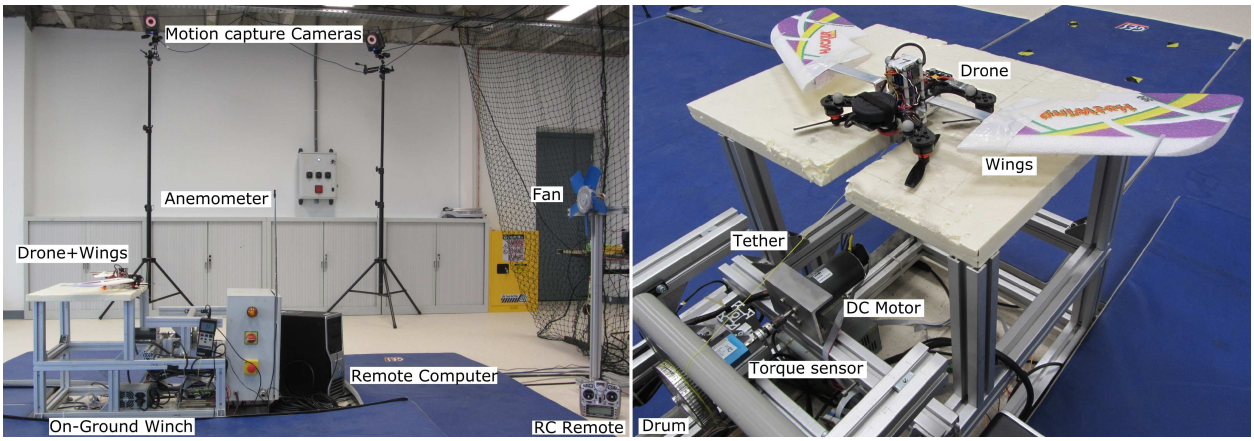

Figure 5.3 The different components of the benchmark.

5.3.1 Drone

The drone is composed of 4 NOVA RM2206-KV2300 motors with 5046BN propellers, driven by 30A Electronic Speed Controllers (ESC). A 3S 1300mAh LiPo battery ensure the power supply of the drone. The flight controller is a STM32 based KAKUTE F7 from Holybro,

running the PX4 autopilot. It communicates through a Wi-Fi/serial bridge made with an ESP32 micro-controller. PX4 Autopilot [39] [40] uses its embedded inner loop to control the attitude of the drone, based on an embedded estimator that uses IMU and a measurement of the position that comes from the motion capture system [41]. Setpoints sent to the drone through a mavlink protocol are the global thrust and Euler angles roll, pitch and yaws. Propellers are chosen to point downwards in order to have a center of mass as close as possible of the bridle point of the tether. This reduces the amplitude of the disturbance torques induced by the pulling force of the tether on the drone. Wings are Hotwing 500 model, made from polystyrene and fabricated by Hacker Model. Its area of $0.09m^2$ allows one to potentially generate a rated power around $300W$. A remote controller communicates directly with the flight controller through a FrSky radio protocol to ensure emergency stop functions.

5.3.2 On-ground Winch

On-ground winch is actuated with a 100W Maxon 2260L DC-Motor driven by a four-quadrants amplifier Maxon ADS 50/10 that controls its current. The drum of $5cm$ radius is linked to that motor through a Kistler 4502a rotating torque sensor that provides an accurate measure of the tether tension T_T. Current setpoint and current torque measurement are connected to the remote computer with a DAC PCI DAS1200 board from Measurement Computing.

5.3.3 Motion capture system

Motion capture system is a set of 9 Vicon T40s cameras that tracks a pattern of reflectors fixed to the drone and give its position and orientation. It is run on a dedicated computer that uses the Tracker Vicon software and is able to communicate with the remote computer through the VRPN protocol. From Cartesian position of the drone provided by the motion

capture system, the algorithm computes its spherical coordinates r, β and η (see Equation 5.5).

$$r = \sqrt{x^2 + y^2 + z^2}, \quad \dot{r} = \frac{\dot{x}x + \dot{y}y + \dot{z}z}{r}, \quad \beta = atan\left(\frac{z}{\sqrt{x^2 + y^2}}\right) \tag{5.5}$$
$$\eta = atan\left(\frac{y}{x}\right), \quad \dot{\eta} = \frac{\dot{y}x - y\dot{x}}{x^2 + y^2}, \quad \dot{\beta} = \frac{\dot{z}\sqrt{x^2 + y^2} - z\frac{(\dot{x}x + \dot{y}y)}{\sqrt{x^2 + y^2}}}{r^2}$$

Note that in an outdoor experimentation, where the use of a motion capture system is no longer possible, one has to use GPS position to provide the coordinates of the drone with a much lower accuracy and frequency. Consequently, in order to measure an accurate value of tether length r, the use of an incremental coder fixed on the DC motor of the winch would be a better strategy.

5.3.4 Remote computer

The on-ground remote computer is an Ubuntu desktop computer based on an Intel Xeon 2.53Ghz processor. The control algorithm is implemented within the ROS middleware and run at a frequency of 100Hz. The interface with the motion capture system use the *vrpn_client_ros* node [42] and the communication with the drone is performed through the *mavros* package [43].

5.3.5 Wind disturbance

In order to produce a wind disturbance on the system, we used a $38cm$ fan positioned at $-2.1m$ along x axis and $67.5cm$ along z axis. A hot wire anemometer provides a local mean measurement of the produced wind at the same altitude as the fan and $-0.38m$ along x axis.

Wind Tunnel

However, the wind produced by the fan has a highly perturbed airflow, including rotating movement induced by the rotation of the fan. To have a more homogeneous and clean wind, a wind tunnel (see Figure 5.4) can be used. As it is presented in [32], the wind tunnel is composed of a honeycomb and 9 brushless motors of $800W$ each distributed on a surface of $1.85m^2$. A hot wire anemometer is also used to have a local mean measurement of the produced wind.

Figure 5.4 The Gipsa-Lab's wind tunnel.

5.3.6 Parameter identification

All necessary identified physical parameters of the system are gathered into Table 5.2.

Table 5.2 Physical Parameters

Symbol	Name	Value
M_M	Mass of airborne subsystem	0.774 kg
M_D	Ground station rotor mass	0.0481 kg
S	Wing area	0.09 m^2
α_D	Wing configuration angle	0 deg
ρ	Air density	1.225 kg/m^3
τ_T	Time constant of motor current loop	0.02 s
τ_{T_D}	Time constant of drone thrust loop	0.085 s
τ_ϕ	Time constant of drone inclination loop	0.194 s
u_{rmin}	Minimum tension in the winch	0 N
u_{rmax}	Maximum tension in the winch	8 N
T_{Dmin}	Minimum drone's thrust	0 N
T_{Dmax}	Maximum drone's thrust	17.7 N
ϕ_{min}	Minimum drone's inclination angle	-50 deg
ϕ_{max}	Maximum drone's inclination angle	50 deg

To identify the time response τ_ϕ of the closed loop of the inclination angle ϕ, a first order model (in blue) is fitted on experimental data (in red) on Figure 5.5. A fit of 33.62% is obtained for a value of $\tau_\phi = 0.194s$. We also identified with the same method the time constant of a first order model for the current loop of the DC winch's motor. This loop is fast enough to be considered as instantaneous with regard to the whole system dynamics. As it is difficult to have an accurate measure of the thrust force of the drone, we estimated its first order model by seeking the time response of the position of the drone at the first take-off, which corresponds to a situation that is close to a step response. On the other hand, a hover is performed on the drone with no tether to calibrate the thrust that compensate the mass of the system. Note that parameters S, α_D, τ_T, ρ, as well as aerodynamic parameters of the

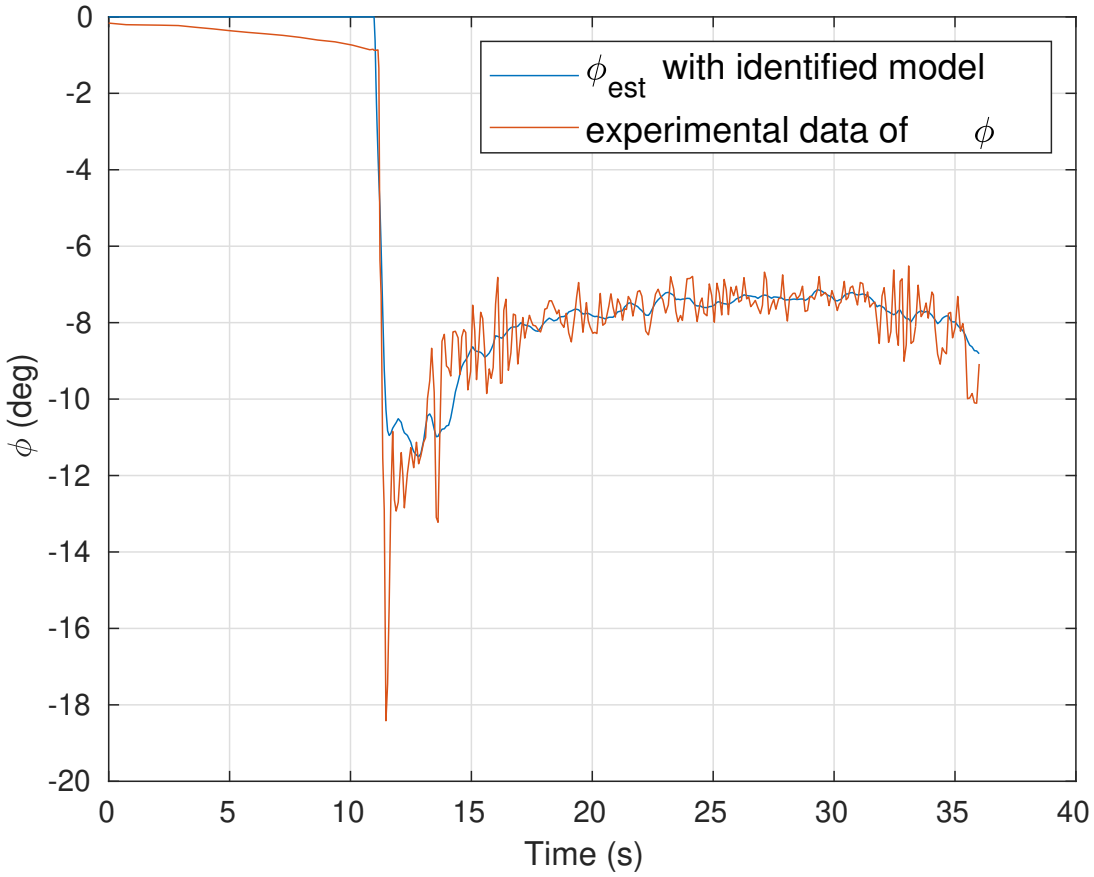

Figure 5.5 Identification of τ_ϕ

wing (Figure 2.2) are not used to the experimental implementation but only for simulation purpose.

5.4 Experimentation Results

Results presented in this section correspond to the proposed controller in Chapter 3 with no integration of the aerodynamic forces in the control design, and with the simple MIX block that corresponds to Equation 3.1. The EKF is also not implemented in real time however it is performed offline on the experimental data. The first experimentation is done with no wind, results are presented in Subsection 5.4.1. Then an experimentation with a wind around $2m/s$ generated by the fan is done and results are shown in Subsection 5.4.2. Finally, the last experimentation corresponds to a take-off with no wind and once the system is up, a wind of $0.6m/s$ is generated by the wind tunnel. Results of this experimentation are in Subsection 5.4.3.

5.4.1 No wind disturbance

Figures 5.6 to 5.11 shows the results of the experimentation with no wind disturbances.

On Figure 5.6 the trajectory of the system during the considered scenario is represented in 2D. In black, this is the desired trajectory, in red the one described by the system during the take-off and in blue during the landing. The black rectangle corresponds to the on-ground station and in light blue, the tether is represented. The system is represented in pink on this figure at one position of the overall trajectory. The trajectory is close to the desired one and the main difference is during the take-off.

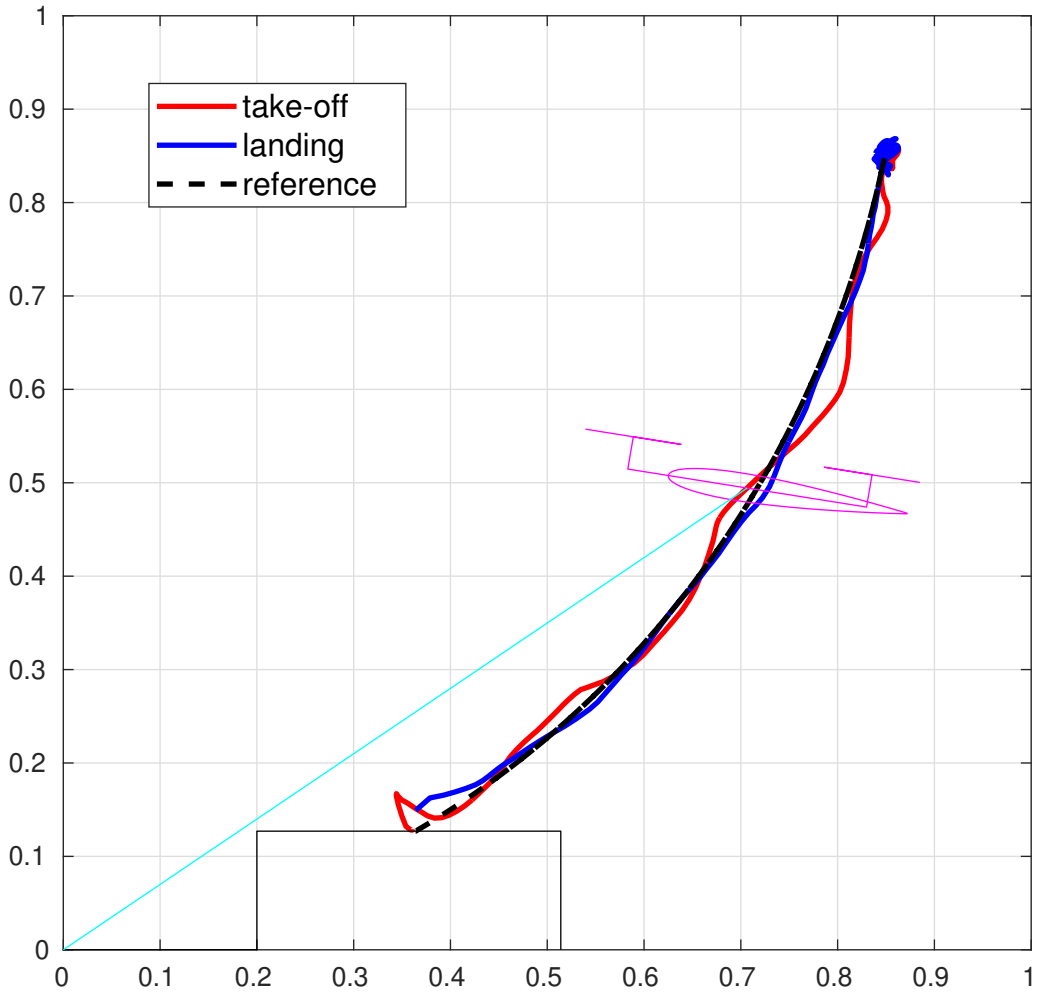

Figure 5.6 Trajectory of the system with no wind disturbance

The evolution of the tether length is presented on Figure 5.7, it is compared to the reference value and it also shows the control input u_r. This state follows well the reference thanks to the choice of the actuator: the winch command, the tether length and this actuator is very accurate, that allows an efficient control of the tether length, despite a significant friction force that has been estimated around $0.4N$. The control input u_r never goes to its $8N$ saturation and is far from it.

The evolution of the elevation angle β can be seen on Figure 5.8 as well as its control

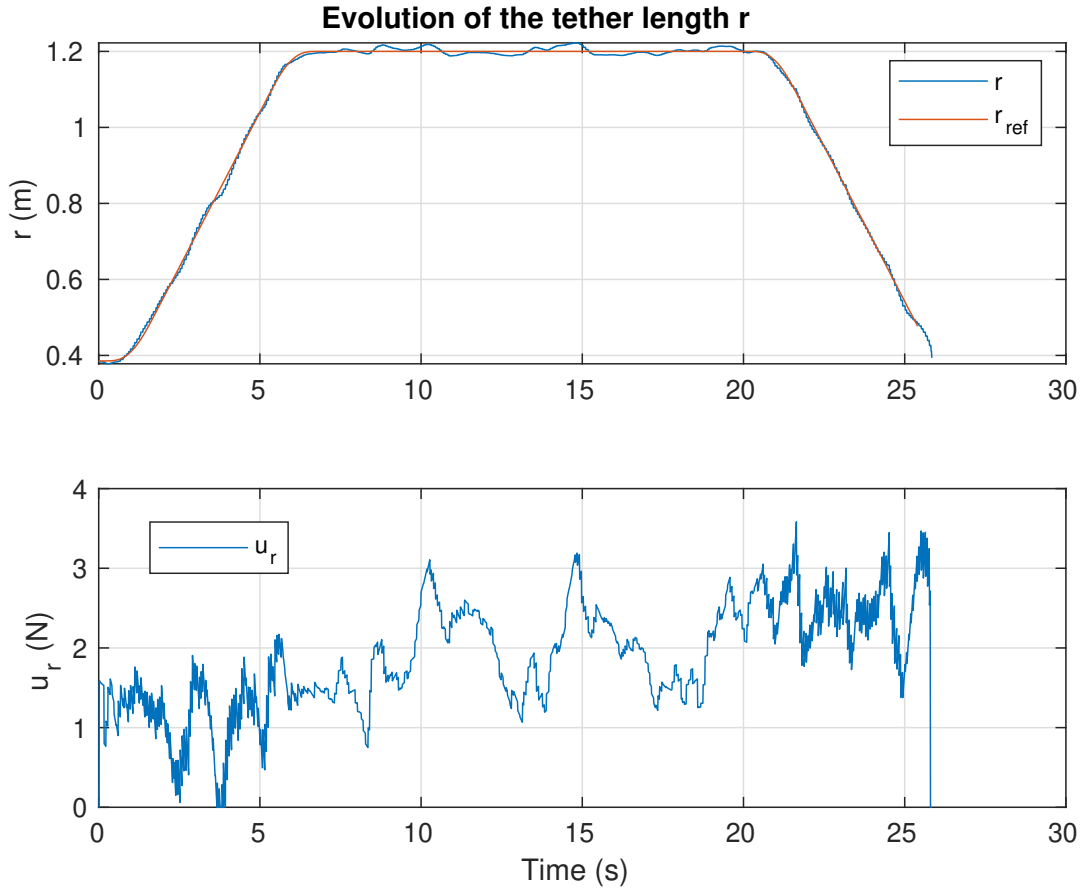

Figure 5.7 Evolution of the tether length r with no wind disturbance

input u_β. It follows well its reference value but with more tracking error since the drone is less accurate. An overshoot at the beginning of the take-off is observed. It is not due to ground-effect since this phenomena is also observed in simulation where the ground-effect is not considered.

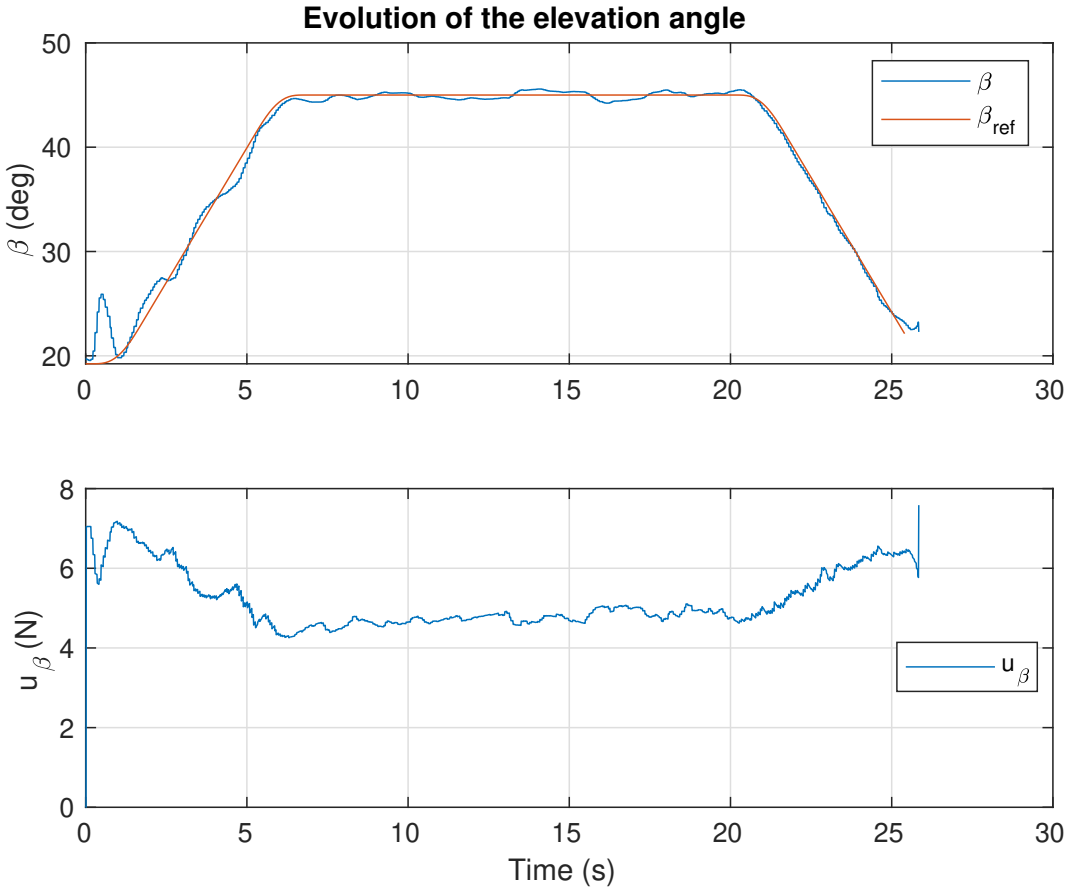

Figure 5.8 Evolution of the elevation angle β with no wind disturbance

The last state η is presented on Figure 5.9. It oscillates around its desired value 0° and tends to stabilize with an oscillation around 1°.

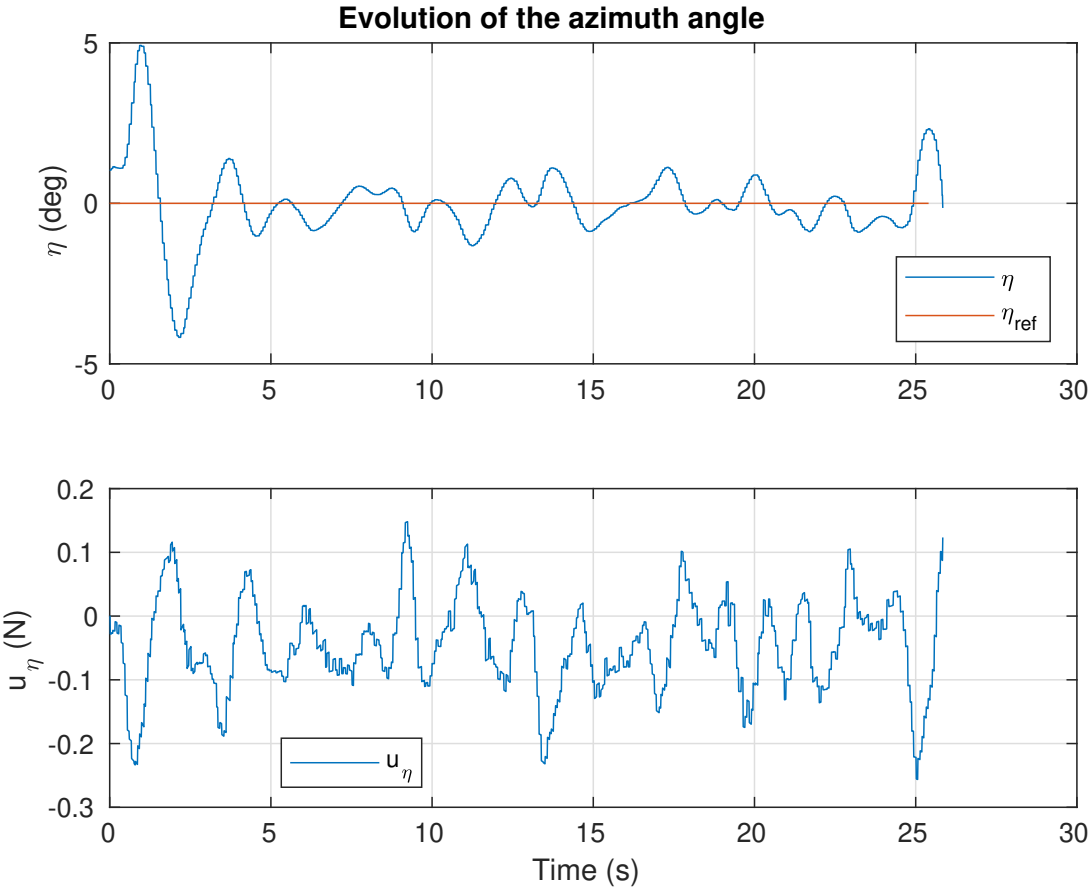

Figure 5.9 Evolution of the azimuth angle η with no wind disturbance

An important point is that the tether has to be always taut, meaning the tether tension T_T is above $0N$. This tension is shown in Figure 5.10. The tether tension never goes below $0.7N$ and is in average around the desired value $1.5N$. Its command u_{T_0} shows that even if the control law is in open loop, the command takes into account the influence of the weight and elevation angle β. However, the open loop doesn't allow to reject disturbances and modeling errors.

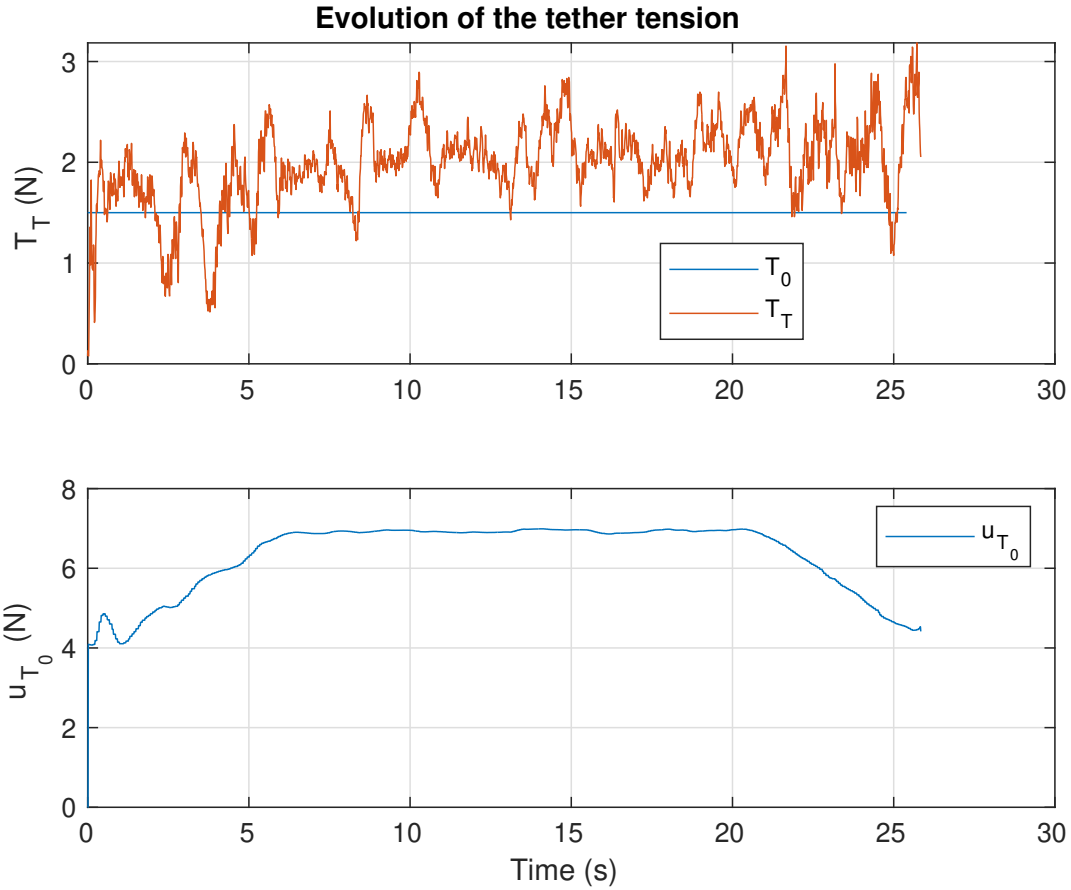

Figure 5.10 Evolution of tether tension T_T with no wind disturbance

The drone inputs ϕ_{ref}, the inclination angle measured by the motion capture ϕ, and the thrust T_D are shown on Figure 5.11. The inclination angle stabilize itself around $-7deg$ and the thrust is around $8N$. On the inclination angle, the influence of the delay compensation is efficient. The two signals ϕ_{ref} and ϕ are well synchronized.

Note that these results are quite close to the corresponding simulation ones presented in Section 3.6.1. In particular, the same kind of overshoot on elevation angle β is observed.

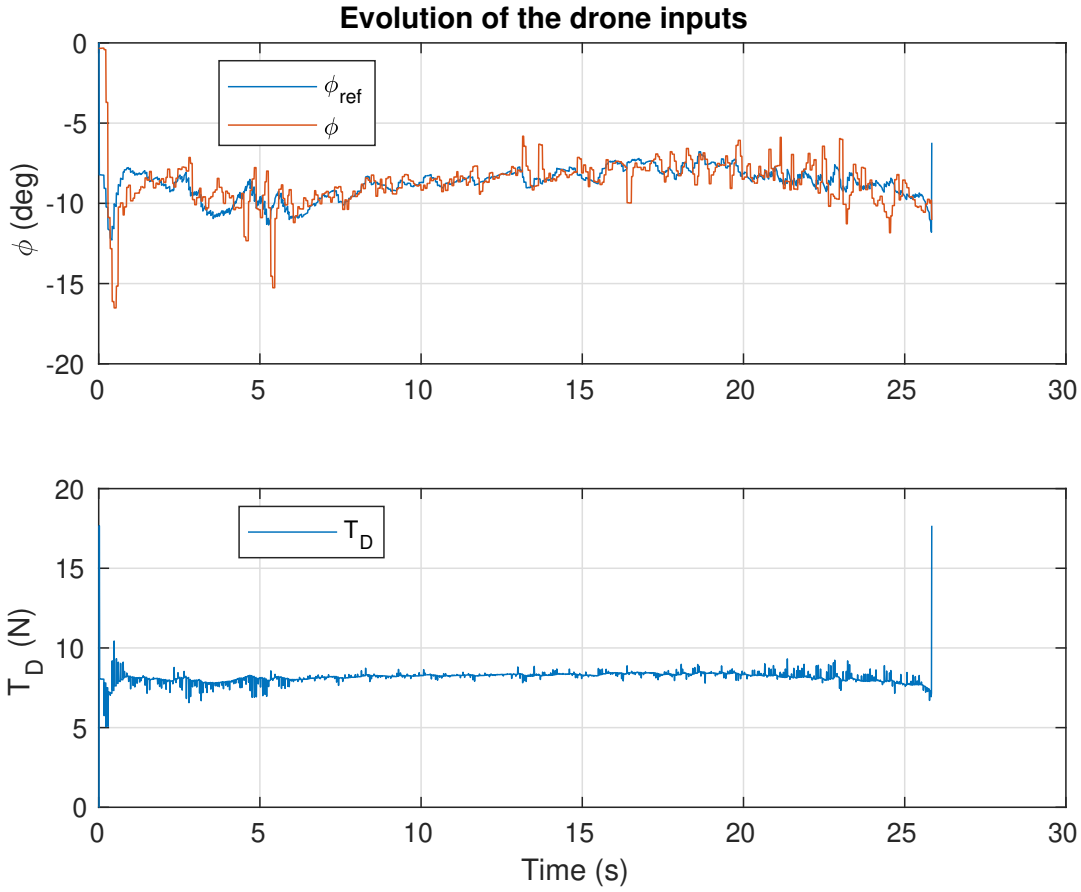

Figure 5.11 Evolution of drone inputs with no wind disturbance

5.4.2 Case with $2m/s$ wind disturbance produced by the fan

A wind disturbance around $2m/s$ produced by the fan is applied on the system. Figures 5.12 to 5.17 shows the results of this experimentation.

On Figure 5.12 the trajectory of the system is compared to its reference. With this wind condition, the trajectory is more disturbed but in its overall trajectory it follows up well the reference and it never gets in a critical zone where the system could crash.

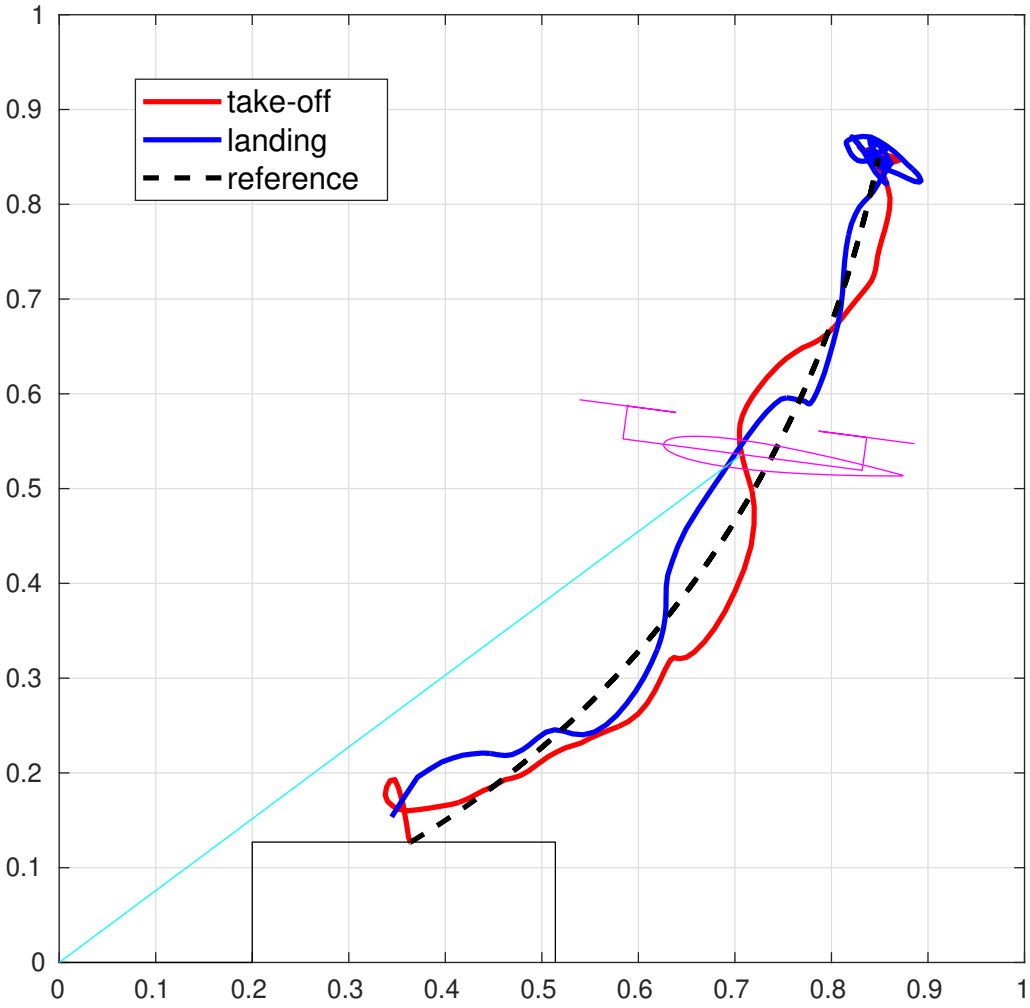

Figure 5.12 Trajectory of the system with a $2m/s$ wind disturbance

The tether length r follows well its reference as shows Figure 5.13. This result confirm the choice of the winch to actuate the tether length. The control input u_r still respect the saturation in this case.

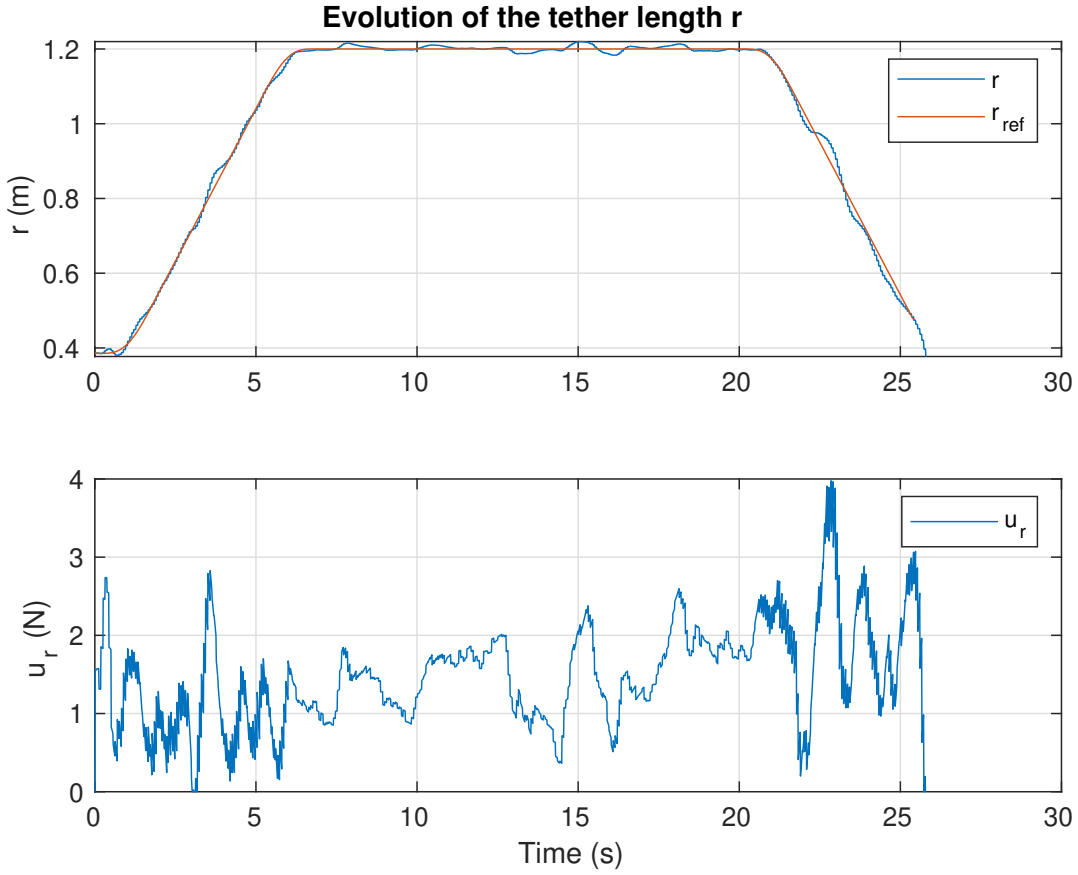

Figure 5.13 Evolution of the tether length r with a $2m/s$ wind disturbance

Figure 5.14 shows that due to the wind the elevation angle β is more perturbed and oscillations are more important but it is still close to the desired value. The overshoot at the beginning is still here and is more important, almost 10°.

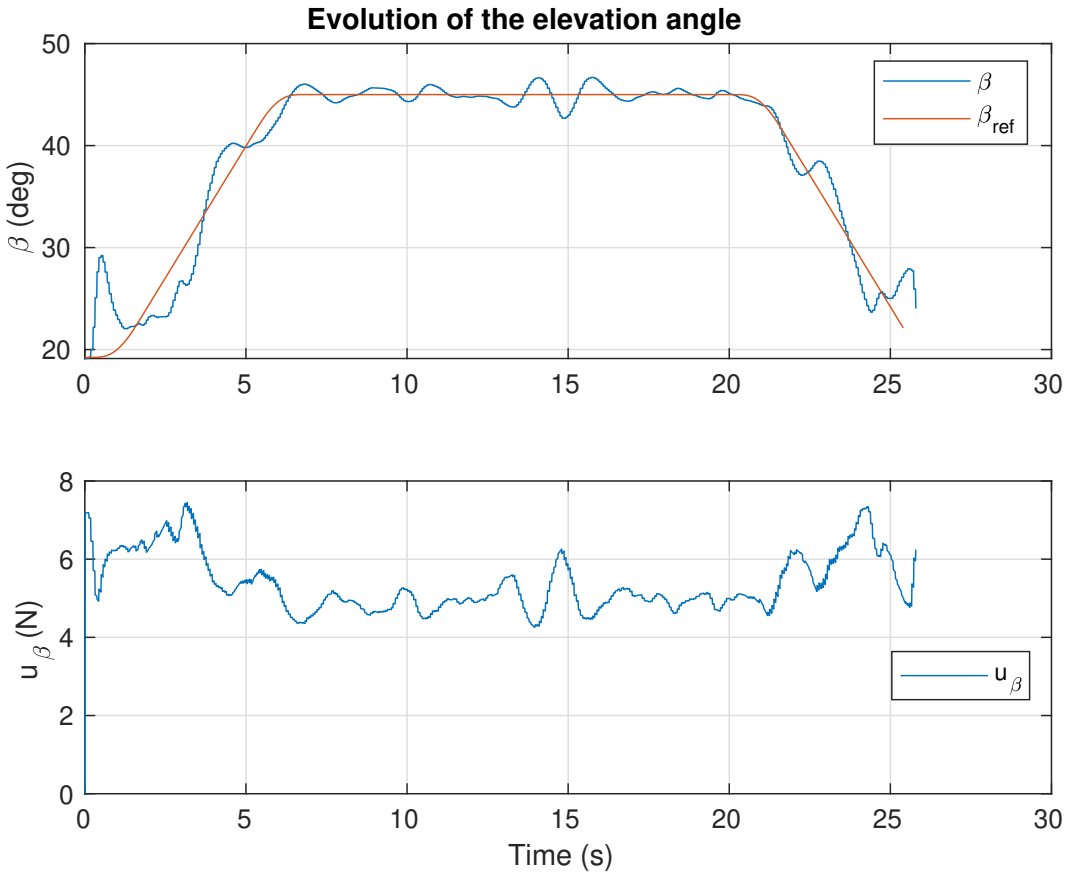

Figure 5.14 Evolution of the elevation angle β with a $2m/s$ wind disturbance

The azimuth angle η is also impacted by the wind, it oscillates around the desired value with an error around 5°.

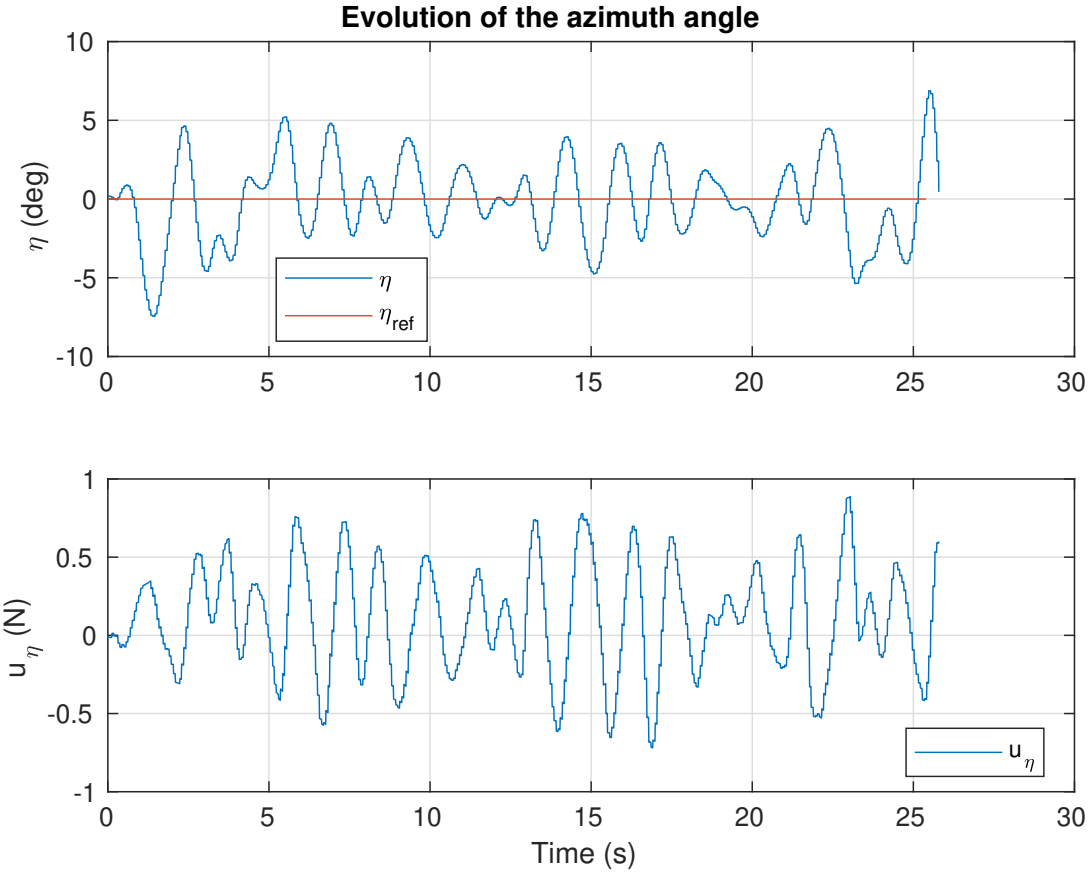

Figure 5.15 Evolution of the azimuth angle η with a $2m/s$ wind disturbance

On Figure 5.16, the tether tension is always above $0.2N$ and thus the tether is always taut during the experimentation. It oscillates around the desired value $1.5N$.

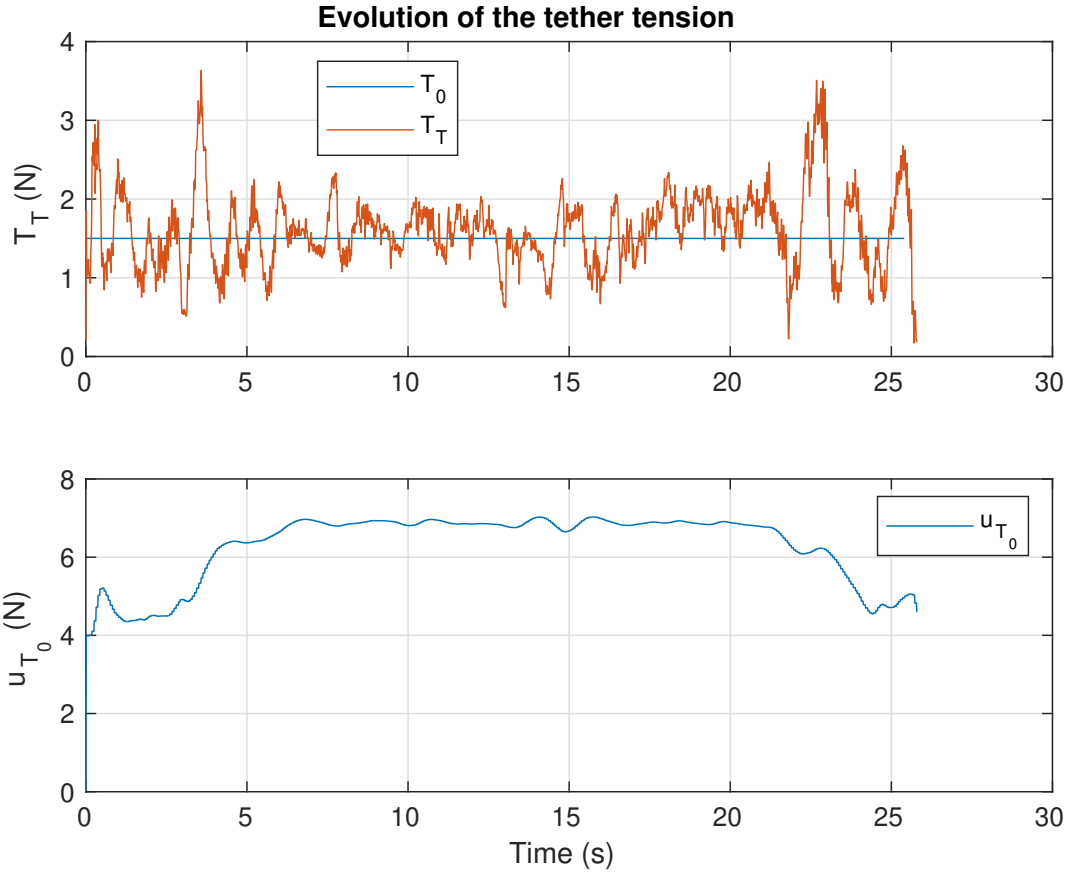

Figure 5.16 Evolution of tether tension T_T with a $2m/s$ wind disturbance

The drone inputs are presented on Figure 5.17, the inclination angle ϕ has to compensate the wind disturbances and is thus more oscillating. The thrust stabilize around the same value $8N$.

Due to the wind disturbance the system is more perturbed but it still succeed to follow the references and to keep the tether taut. For higher wind generated by the fan, the system crashes due to the turbulent nature of the wind. This is why more robust algorithm presented in Sections 3.7 and 3.8 has to be implemented in order to safely control the system under this kind of severe conditions.

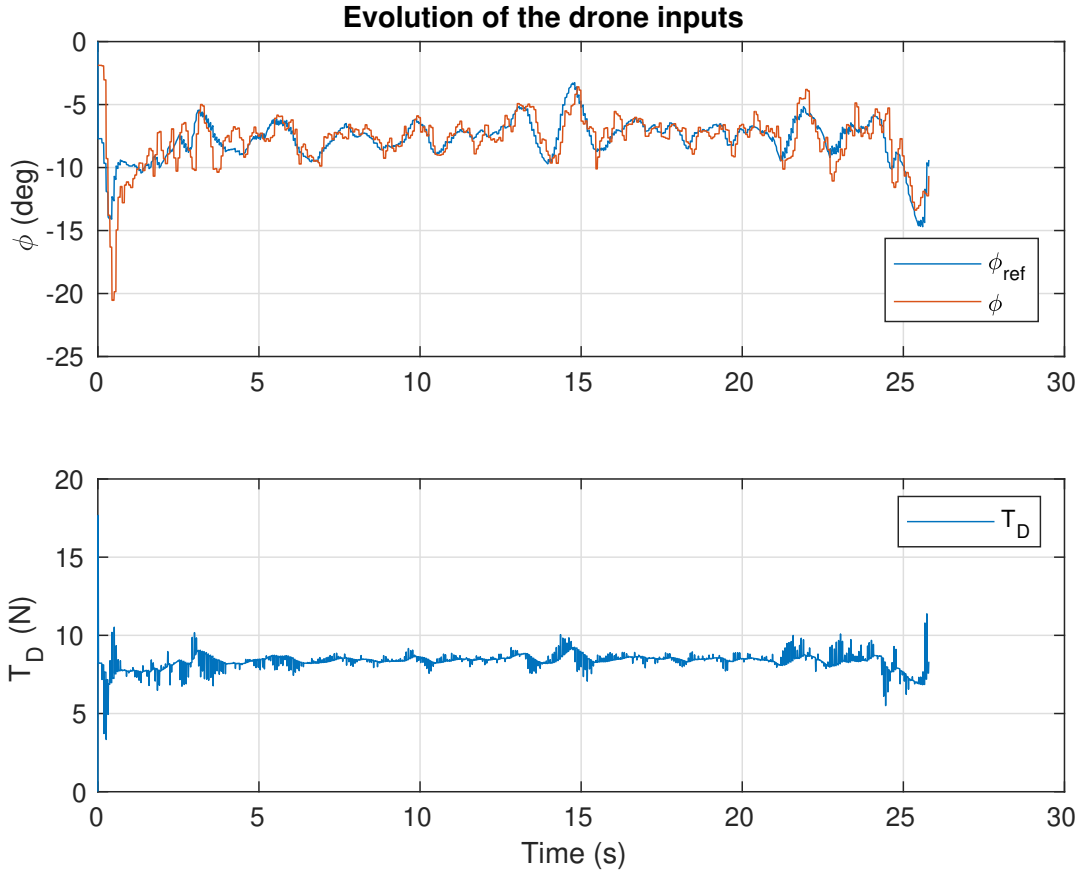

Figure 5.17 Evolution of drone inputs with a $2m/s$ disturbance

5.4.3 Case with $0.6m/s$ wind disturbance produced by the wind tunnel

The experimentation starts with a take-off with no wind disturbance and then a wind around $0.6m/s$ produced by the wind tunnel is applied for the rest of the scenario. Figures 5.18 to 5.23 presents the results for this experimentation.

The trajectory of the system is presented on Figure 5.18 and shows that the system follows well the desired trajectory.

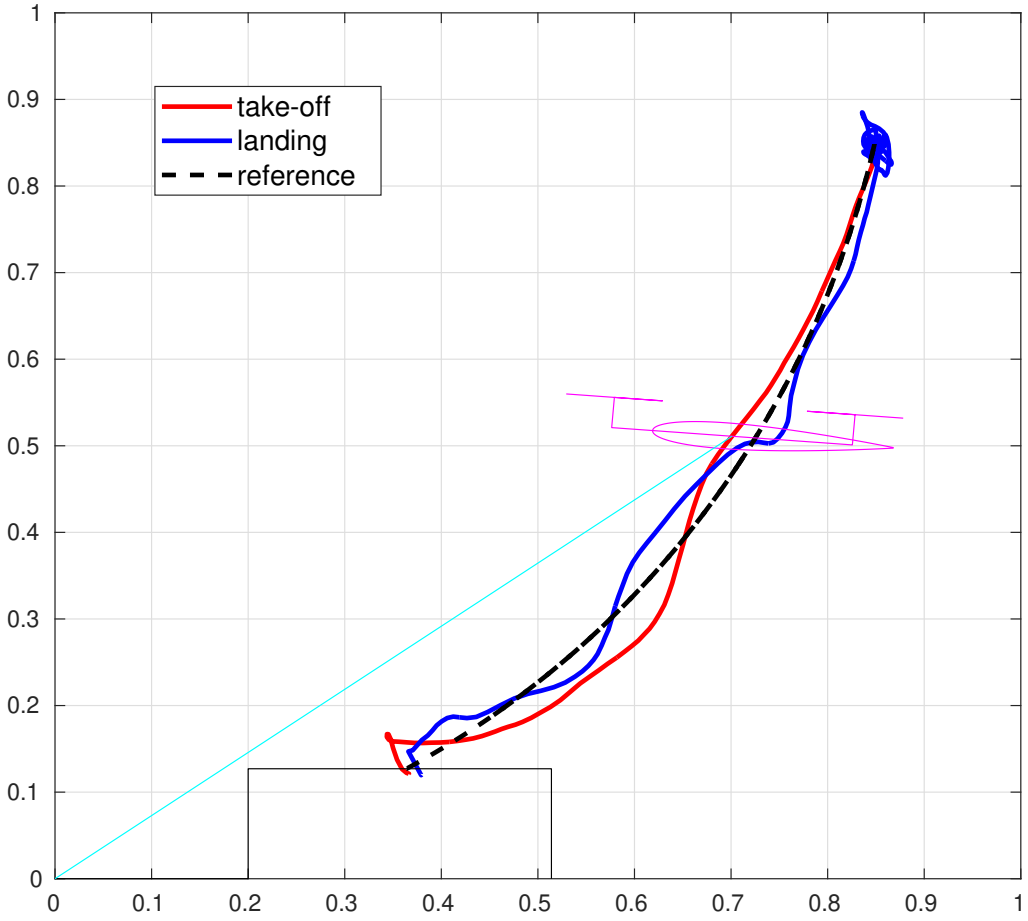

Figure 5.18 Trajectory of the system with a $0.6m/s$ wind disturbance

On Figure 5.19 the evolution of the tether length r is closed to the reference. It also shows the influence of the wind which appears after the take-off at $t = 22s$ and induces some small oscillations. The landing is performed under a wind of $0.6m/s$ and succeed.

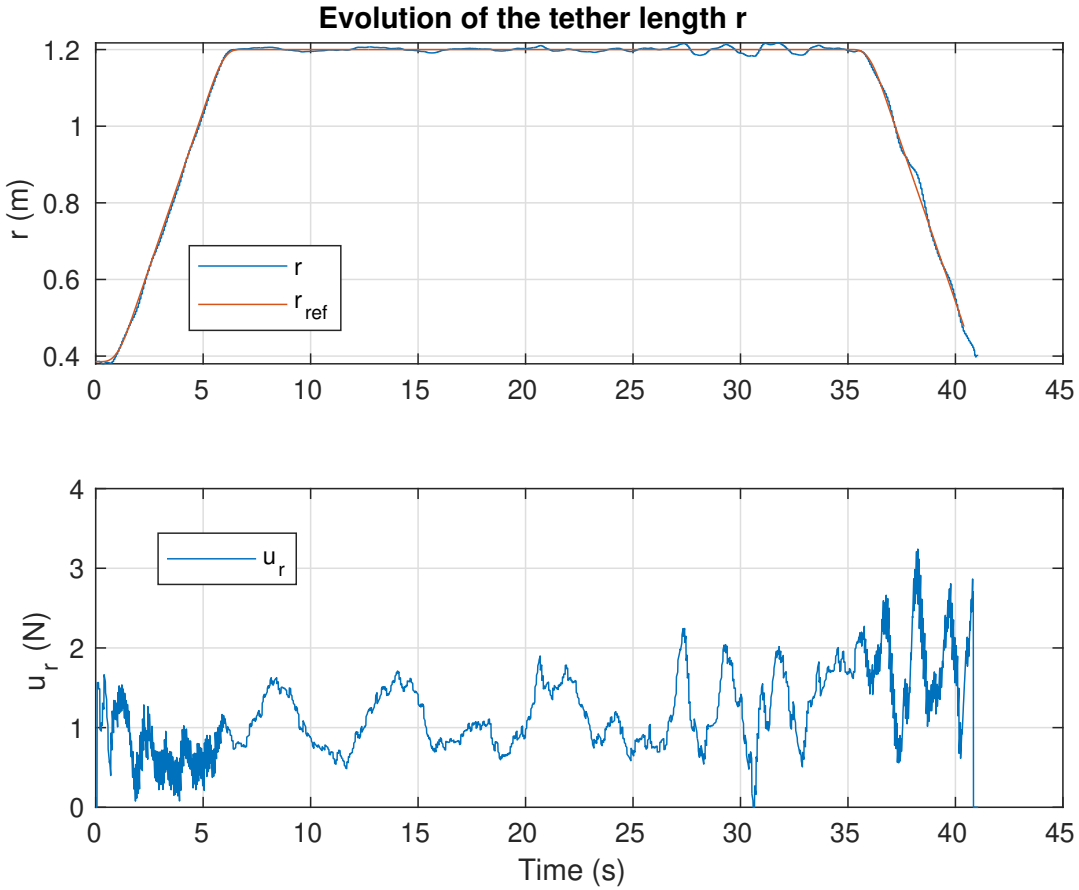

Figure 5.19 Evolution of the tether length r with a $0.6m/s$ wind disturbance

Same observations can be made for the elevation angle β on Figure 5.20.

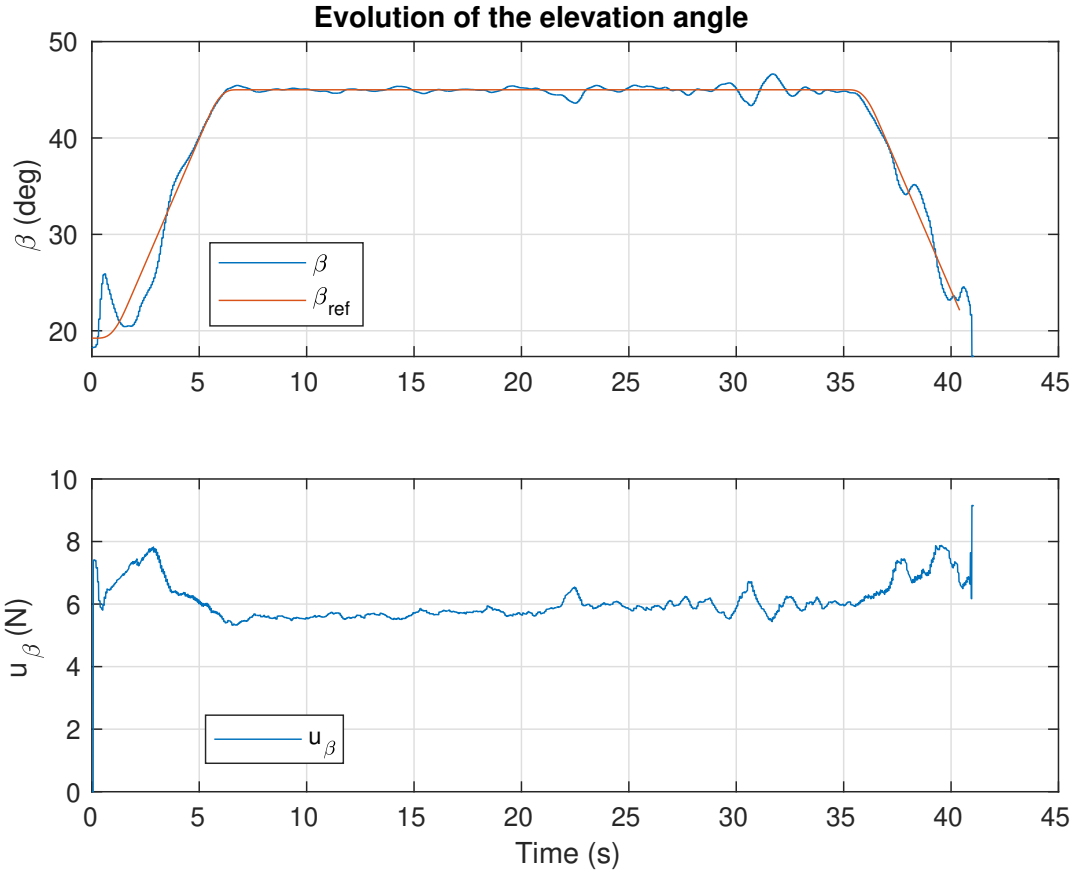

Figure 5.20 Evolution of the elevation angle β with a $0.6m/s$ wind disturbance

On Figure 5.21 the azimuth angle η oscillates at the beginning, due to the take-off phase and then stabilize around its desired value 0°. The oscillations are more important once the wind appears.

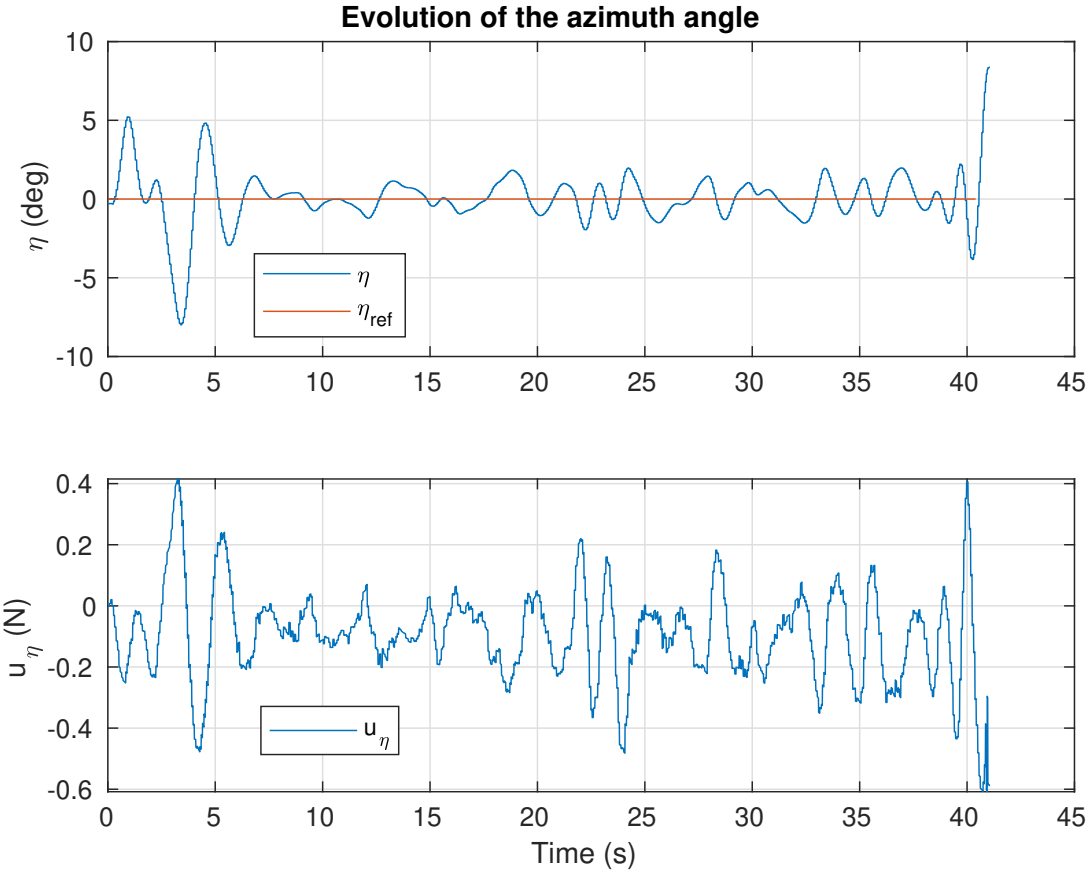

Figure 5.21 Evolution of the azimuth angle η with a $0.6m/s$ wind disturbance

The tether tension T_T on Figure 5.22 is always above $0.7N$, thus the tether is always taut. It also appears that the tension is more perturbed once the wind is on and during the landing. Oscillations have an higher magnitude. But in its overall behavior the open-loop still succeed to maintain the tether tension around its desired value $1.5N$.

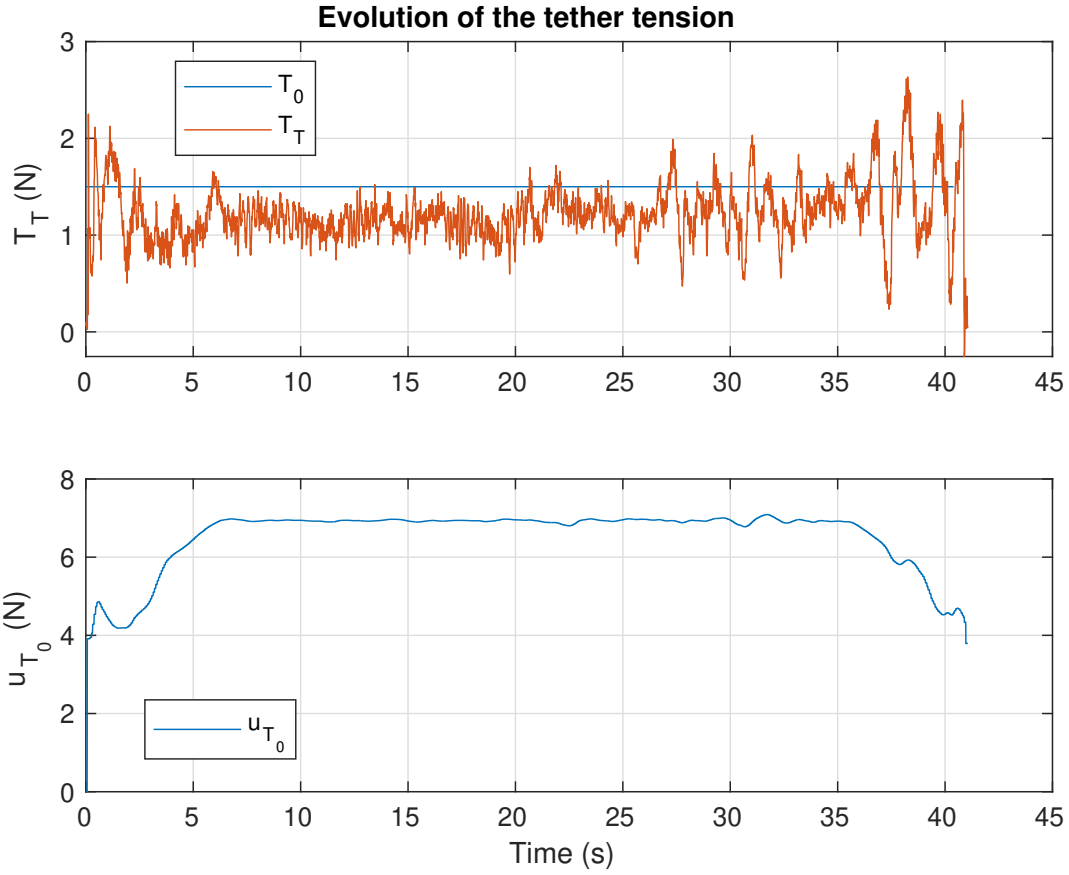

Figure 5.22 Evolution of tether tension T_T with a $0.6m/s$ wind disturbance

On Figure 5.23, the influence of the wind can also be seen on the inclination angle ϕ which is more disturbed once the wind is on.

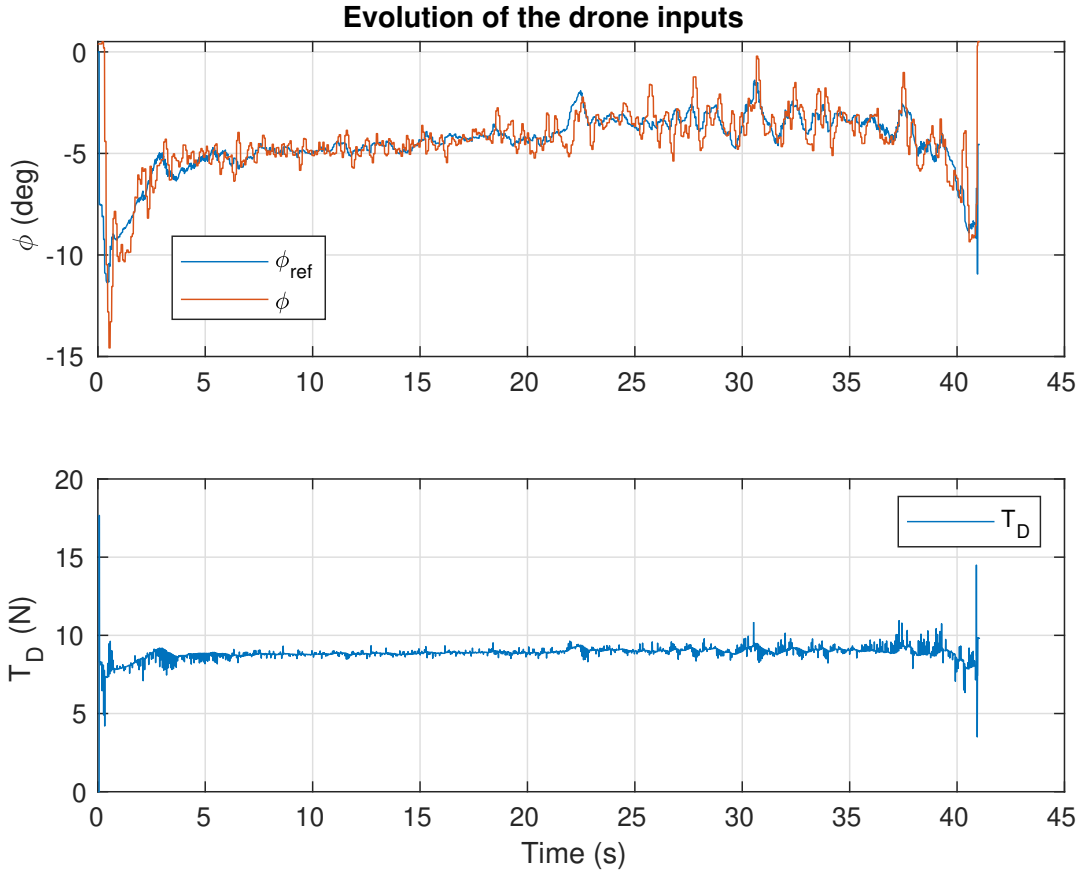

Figure 5.23 Evolution of drone inputs with a $0.6m/s$ wind disturbance

5.4.4 Offline Estimator

In this subsection, the algorithm of the proposed Extended Kalman filter presented in Chapter 4 is applied offline on the experimental data extracted from the experiments for no wind speed $v = 0m/s$ presented in Subsection 5.4.1. It is worth pointing out that our experimental facility does not include an adequate wind tunnel that could produce significant and relatively stable lift and drag force on the system.

In order to better adapt to the uncertainties of the experimental framework and to converge faster towards the actual values of the unknown forces, the weighting matrices of

EKF are adjusted as follows:

$$Q = \begin{bmatrix} 1^{-3} & 0 & 0 & 0 & 0 & 0 \\ 0 & 1 & 0 & 0 & 0 & 0 \\ 0 & 0 & 200 & 0 & 0 & 0 \\ 0 & 0 & 0 & 1^{-3} & 0 & 0 \\ 0 & 0 & 0 & 0 & 1 & 0 \\ 0 & 0 & 0 & 0 & 0 & 200 \end{bmatrix}, \; R = \begin{bmatrix} 1^{-10} & 0 \\ 0 & 1^{-10} \end{bmatrix} \tag{5.6}$$

Note that, this experiment is performed with the same scenario exhibit in Section 5.2. In Figure 5.24 the estimated variables provided by the EKF and the measured ones are compared in the case of $v = 0m/s$.

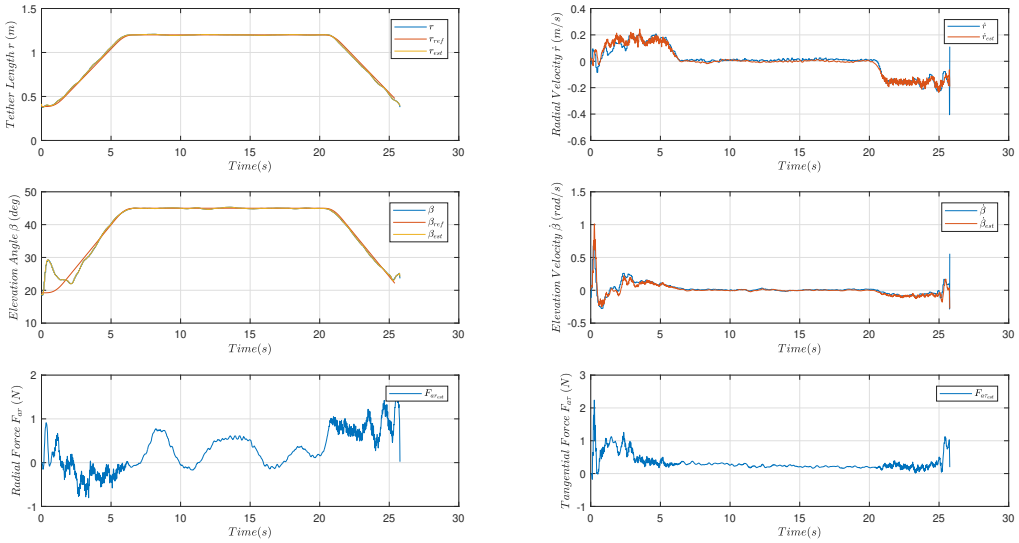

Figure 5.24 Estimation of the actual state variable for $v = 0m/s$.

As mentioned previously, since there is no wind, the estimated forces are not the aerodynamic ones, but reflect other forces that are not included in the prediction model used in the EKF algorithm. In particular, the estimated radial force is very close to the behavior of a dry friction as it can be seen in Figure 5.25. This figure also illustrates that the estimated variables $\hat{r}$, $\dot{\hat{r}}$, $\hat{\beta}$ and $\dot{\hat{\beta}}$ are very close to the measured ones, which confirm further the good

performance of the proposed EKF. On the other hand, the tangential part of estimated force

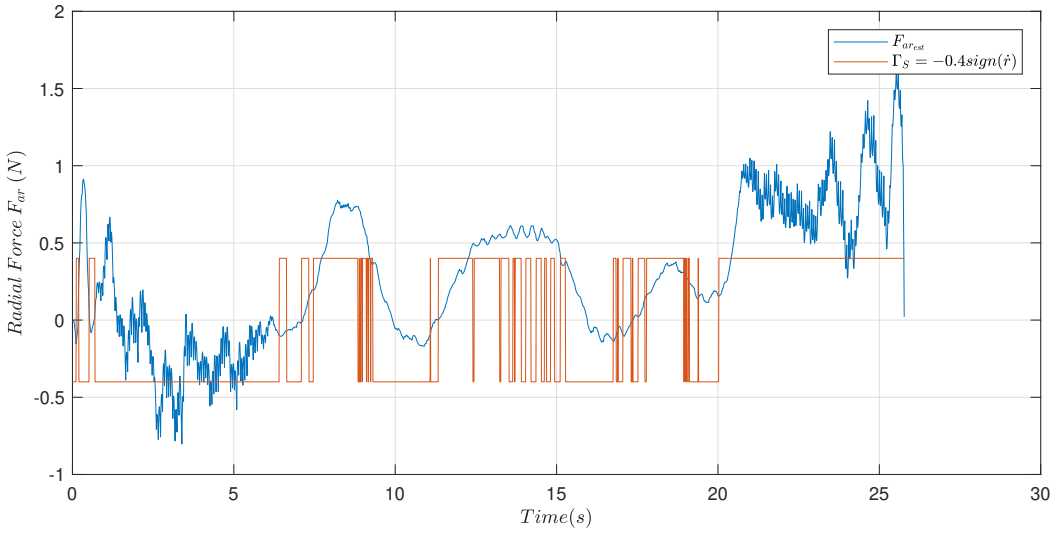

Figure 5.25 Estimated radial force compared with a model of static friction in the ground station.

is highly correlated (cross correlation = 0.833) to the tangential projection of the drone thrust T_D. We can conclude that the EKF gives an estimation of the difference between the desired drone thrust and the effective one.

5.5 Conclusion

These experimentations show that the take-off and landing without wind can be perform with very good performances thanks to the proposed feedback linearization technique. Wind disturbance produced by the fan and the wind tunnel are highly turbulent and thus the system managed to perform the scenario safely only until a mean wind of $2m/s$. In particular, the take-off is a very difficult part, since there is an overshoot on β, which is amplified by the wind. Results from simulation and experimentation are quite close so we can expect significant improvement in term of robustness toward wind condition by integrating the aerodynamic forces in the control design, and more likely by using aerodynamic forces as additional actuators. As expected from simulation results, experimental results confirms also

the relevance of using the on-ground winch to control the tether length where its tension is maintained by the radial force of the drone. Despite significant dry friction acting on the radial part of the system, the tether length's regulation has better results than elevation angle regulation, for no wind condition and more clearly in presence of wind perturbations. These scenarios also show that the winch can absorb aerodynamic forces perturbations with very little impact on tether length's regulation. Results also prove that the estimator is able to estimate forces that are not included in the model. Finally, in order to perform experimentation with higher wind speed, a wind tunnel creating a smoother wind has to be used.

Chapter Six

General conclusion

6.1 Conclusion

AWE systems are very complex to control, in particular during the take-off and landing phases. In this thesis work, this problem have been tackled.

The main contribution of this thesis are:

- **Using Output Feedback Linearization Method on an AWE system:** In chapter 3, the output feedback linearization method is applied to this AWE system. Simulations are performed using this controller on different configurations of the system and under different wind conditions. The influence of taking into account or not the aerodynamic forces in the controller design step is also discussed in this chapter. The Magnus wing case shows good performances thanks to a direct mean to control lift and drag forces independently of the drone angle. This chapter allows to validate the design of the controller and the relevance of using the on-ground winch to control the tether length. It also highlight the necessity of taking into account the aerodynamic forces, either by integrating them directly in the controller or using it as coupled actuator, having a dedicated optimisation algorithm that has to work in real-time to deal with them.

- **Estimation of external forces:** Chapter 4 presents an extended Kalman filter, developed to estimate the external forces of the system as the aerodynamic forces,

the dry friction and the forces due to propeller performance variation. This EKF is then tested in simulation and shows that it provides accurate estimations of the state vector of the system and the unknown forces that act on it. It also allows to obtain a valuable aerodynamic model of the system which is use-full to evaluate and optimize performances of such AWE system.

- **Experimental test:** The last contribution is presented in Chapter 5 and is about developing a prototype to experimentally validating precedent results. Results show that the take-off and landing without wind can be performed in very good way thanks to the proposed feedback linearization technique. However, for now, since the aerodynamic forces are not take into account in the implemented method on the test bench, the system is not able to take-off and land with a wind superior to $2m/s$. But, since results from simulation and experimentation are quite close, we can expect significant improvement in term of robustness toward wind condition by integrating the aerodynamic forces in the control design, and more likely by using aerodynamic forces as additional actuators.

This thesis work therefore brings a new contribution to the more general objective of being able to do a complete production cycle including a take-off, a production phase and a landing phase.

The experimental implementation also allows us to learn about the constraints on the system and we have been able to obtain a reliable model of the system, which gives close behavior in simulation and in experimentation. This will permit to gain time and avoid several crashes, see Figure 6.1.

Finally, the study of different configurations of the wings toward the drone were very interesting. With $\alpha_D = 0$, the system can switch between using the drone, the lift from wings, or both to support its weight. For Magnus wing, even if they have lower aerodynamic performances compared to classical airfoils, they allows to have a better path following

Figure 6.1 Crash of the drone during an experimentation.

under different wind conditions by controlling aerodynamic forces and drone orientation independently. It seems to be a safer alternative. For the last configuration, $\alpha_D = \frac{\pi}{2}$, we highlighted the disadvantages that no lift are generated during the take-off and landing phases which leads to a system more sensitive to wind gusts and dependent on the drone limits.

6.2 Perspectives

Other issues have to be tackled on this subject before obtaining a fully functional system. The experimentation has to be performed under a higher and smoother wind to experimentally validate the controller and the estimator. The experiments also have to be performed in outdoor conditions with a higher tether length and thus integrating a tether model with its associate drag. The developed work will allow to better understanding some remaining difficulties, like the overshoot at the beginning of the take-off phase. To perform a fully automated system, it has to execute a complete cycle with the management of the production thanks to a high level management algorithm like the one presented in [28], coupled with security parts that will have to take the decision of taking-off and landing depending on wind conditions and its forecasts.

The developed models and controllers can be used to do a systematic study according to performance or robustness toward meteorological conditions criteria for the different configurations of the system and in particular for α_D between 0 and $\frac{\pi}{2}$.

Bibliography

[1] IEA. *Shaping a secure and sustainable energy future for all.* URL: https://www.iea.org/ (visited on 10/04/2021).

[2] A Van Gries. "Improvements in or relating to Wind-driven Power Apparatus". In: *Application Number GB2081337A* 20 (1938).

[3] Miles L Loyd. "Crosswind kite power (for large-scale wind power production)". In: *Journal of energy* 4.3 (1980), pp. 106–111.

[4] Ampyx Power. *Airborne Wind Energy.* URL: https://www.ampyxpower.com/ (visited on 10/04/2021).

[5] Kitemill. *Airborne Wind Energy.* URL: https://www.kitemill.com/ (visited on 10/04/2021).

[6] Makani. *Harnessing wind energy with kites to create renewable electricity.* URL: http://www.makanipower.com/ (visited on 10/04/2021).

[7] Steve Mann, Isaac Harris, and Joshua Harris. "Renewable and sustainable energy reviews". In: (2004).

[8] KitePower. *Plug & Play, Mobile Wind Energy.* URL: http://www.kitepower.eu (visited on 10/04/2021).

[9] EnerKite. *Airborne Wind Energy.* URL: http://www.enerkite.de/en/products (visited on 10/04/2021).

[10] Lorenzo Fagiano and Stephan Schnez. "On the take-off of airborne wind energy systems based on rigid wings". In: *Renewable energy* 107 (2017), pp. 473–488. DOI: 10.1016/j.renene.2017.02.023.

[11] Sebastian Rapp and Roland Schmehl. "Vertical Takeoff and Landing of Flexible Wing Kite Power Systems". In: *Journal of Guidance, Control, and Dynamics* 41.11 (2018), pp. 2386–2400. DOI: 10.2514/1.G003535.

[12] Florian Bauer, Christoph M Hackl, Keyue Smedley, and Ralph M Kennel. "Multicopter-based launching and landing of lift power kites". In: *Airborne Wind Energy*. Springer, 2018, pp. 463–489. DOI: 10.1007/978-981-10-1947-0_19.

[13] Ahmad Kourani and Naseem Daher. "Marine locomotion: A tethered UAV-Buoy system with surge velocity control". In: *Robotics and Autonomous Systems* 145 (2021), p. 103858.

[14] Marco M Nicotra, Roberto Naldi, and Emanuele Garone. "Nonlinear control of a tethered UAV: The taut cable case". In: *Automatica* 78 (2017), pp. 174–184.

[15] S. Eeckhout, M. Nicotra, R. Naldi, and E. Garone. "Nonlinear control of an actuated tethered airfoil". In: *22nd Mediterranean Conference on Control and Automation*. 2014, pp. 1412–1417. DOI: 10.1109/MED.2014.6961574.

[16] Emilio Dicembrini, M Scanavino, F Dabbene, and G Guglieri. "Modelling and simulation of a tethered UAS". In: *2020 International Conference on Unmanned Aircraft Systems (ICUAS)*. IEEE. 2020, pp. 1801–1808.

[17] Enrica Rossi, Mattia Bruschetta, Ruggero Carli, Yutao Chen, and Marcello Farina. "Online nonlinear model predictive control for tethered uavs to perform a safe and constrained maneuver". In: *2019 18th European Control Conference (ECC)*. IEEE. 2019, pp. 3996–4001.

[18] Gipsa-lab. URL: http://www.gipsa-lab.fr/ (visited on 10/04/2021).

[19] A. Hably, R. Lozano, Alamir, and J. M. Dumon. "Observer-based control of a tethered wing wind power system : indoor real-time experiment". In: *The 2013 American Control Conference, (ACC2013)*. 2013.

[20] Rogelio Lozano Jr, Mazen Alamir, Jonathan Dumon, and Ahmad Hably. "Control of a wind power system based on a tethered wing". In: *IFAC Workshop on Embedded Guidance, Navigation and Control in Aerospace (EGNCA 2012)*. Bangalore, India, Feb. 2012. DOI: 10.3182/20120213-3-IN-4034.00027.

[21] Rogelio Lozano. *Unmanned aerial vehicles: Embedded control*. John Wiley & Sons, 2013.

[22] Rogelio Lozano. "Study of the flight dynamics of a kite". Theses. Université de Grenoble, Apr. 2014. URL: https://tel.archives-ouvertes.fr/tel-01424160.

[23] Mariam Samir Ahmed. "Relaxation-cycle power generation systems control optimization". PhD thesis. Université de Grenoble, 2014.

[24] Mariam Ahmed, Ahmad Hably, and Seddik Bacha. "Grid-connected kite generator system: Electrical variables control with MPPT". In: *IECON 2011-37th Annual Conference of the IEEE Industrial Electronics Society*. IEEE. 2011, pp. 3152–3157.

[25] Mariam Ahmed, Ahmad Hably, and Seddik Bacha. "Power maximization of a closed-orbit kite generator system". In: *2011 50th IEEE Conference on Decision and Control and European Control Conference*. IEEE. 2011, pp. 7717–7722.

[26] Mariam Ahmed, Ahmad Hably, and Seddik Bacha. "High altitude wind power systems: A survey on flexible power kites". In: *2012 XXth International Conference on Electrical Machines*. IEEE. 2012, pp. 2085–2091.

[27] Yashank Gupta, Jonathan Dumon, and Ahmad Hably. "Modeling and control of a Magnus effect-based airborne wind energy system in crosswind maneuvers". In: *IFAC*

WC 2017 - 20th IFAC World Congress. Toulouse, France, July 2017. URL: https://hal.archives-ouvertes.fr/hal-01514058.

[28] Yashank Gupta, Jonathan Dumon, and Ahmad Hably. "Power Curve Analysis Of On-ground Airborne Wind Energy Systems". In: *2019 IEEE International Conference on Industrial Technology (ICIT)*. IEEE. 2019, pp. 175–180.

[29] Yashank Gupta. "Magnus Based Airborne Wind Energy Systems". Theses. Université Grenoble Alpes, Nov. 2018. URL: https://tel.archives-ouvertes.fr/tel-02113723.

[30] Paul Williams. "Cable Modeling Approximations for Rapid Simulation". In: *Journal of Guidance Control Dynamics* 40.7 (July 2017), pp. 1779–1788. DOI: 10.2514/1.G002354.

[31] Rogelio Lozano, Jonathan Dumon, Ahmad Hably, and Mazen Alamir. "Energy production control of an experimental kite system in presence of wind gusts". In: *2013 IEEE/RSJ International Conference on Intelligent Robots and Systems*. IEEE. 2013, pp. 2452–2459. DOI: 10.1109/IROS.2013.6696701.

[32] Ahmad Hably, Jonathan Dumon, Garrett Smith, and Pascal Bellemain. "Control of a Magnus Effect-Based Airborne Wind Energy System". In: *Airborne Wind Energy. Advances in Technology Development and Research*. Ed. by Roland Schmehl. Green Energy and Technology. Springer, 2018, pp. 277–301. URL: https://hal.archives-ouvertes.fr/hal-01759173.

[33] RobMOOC. *Commande non-linéaire des robots*. URL: https://www.ensta-bretagne.fr/jaulin/robmooc.html (visited on 10/04/2021).

[34] Matlab. *The Optimal ITAE Transfer Functions for Step Input*. URL: https://www.mathworks.com/matlabcentral/mlc-downloads/downloads/submissions/18547/versions/1/previews/itae/html/itaeoptimtf.html (visited on 10/04/2021).

[35] Cao Yi. "Correcting the minimum ITAE standard forms of zero-displaceemnt-error systems". In: *Journal of Zhejiang University (Natural Science)* 23.4 (1989), pp. 550–559.

[36] Dan Simon. "Kalman filtering with state constraints: a survey of linear and nonlinear algorithms". In: *IET Control Theory & Applications* 4.8 (2010), pp. 1303–1318.

[37] Charles K Chui, Guanrong Chen, et al. *Kalman filtering*. Springer, 2017.

[38] Matlab. URL: https://fr.mathworks.com/products/matlab.html (visited on 10/04/2021).

[39] PX4. *Manual/Stabilized Mode (Multicopter)*. URL: https://docs.px4.io/master/en/flight_modes/manual_stabilized_mc.html (visited on 03/23/2021).

[40] PX4. *Using the ECL EKF*. URL: https://docs.px4.io/master/en/advanced_config/tuning_the_ecl_ekf.html (visited on 03/23/2021).

[41] PX4. URL: https://docs.px4.io/master (visited on 10/04/2021).

[42] ROS. *MAVROS*. URL: http://wiki.ros.org/mavros (visited on 03/23/2021).

[43] MAVROS. URL: http://wiki.ros.org/mavros (visited on 10/04/2021).